

Guest-induced phase transition leads to polarization enhancement in MHyPbCl₃

Pradhi Srivastava¹, Sayan Maity², Varadharajan Srinivasan²

¹Department of Physics, Indian Institute of Science Education and Research Bhopal, Bhopal 462 066, India and

²Department of Chemistry, Indian Institute of Science Education and Research Bhopal, Bhopal 462 066, India

(Dated: November 1, 2024)

We investigate the structural and electronic changes in a 3D hybrid perovskite, methylhydrazinium lead chloride (MHyPbCl₃) from a *host/guest* perspective as it transitions from a highly polar to less polar phase upon cooling, using first-principles calculations. The two phases vary structurally in the orientation of the *guest* (MHy) and the two differently distorted *host* (lead halide) layers. Our findings highlight the critical role of *guest* reorientation in reducing *host* distortion at high temperatures, making the former the primary order parameter for the transition, a notable contrast to the case of other hybrid perovskites. This is also confirmed by the dominating contribution of the *guest* reorientation along the transition pathway. Analysis using maximally localized Wannier functions reveals that polarization enhancement upon heating is primarily due to the *host* atoms, particularly of the more distorted octahedral layer. Despite its pivotal role in the transition, the contribution of *guest* to polarization is relatively weaker, in contrast to previous suggestions. Furthermore, a significant ($\sim 9\%$) feedback polarization induced on the *guest* by *host* distortion significantly alters the density of states occupied by *guest* closer to band-edges, suggesting a non-trivial contribution of *guest* in impacting the optoelectronic properties and exciton binding energies.

I. INTRODUCTION

Organic-inorganic halide perovskites (OIHPs) possess additional structural and chemical flexibility, compared to conventional metal halide perovskites [1–3]. Indicated by chemical formula ABX₃, these materials are similar to *guest-host* systems, where the rigid inorganic sub-lattice (B cation and X anion) *hosts* organic *guests* (A cation) having translational and orientational degrees of freedom. *Guest-host* systems are characterized by complexes involving two or more molecules or ions interacting with each other by forces other than covalent bonds, such as hydrogen bonds, van der Waals (vdW) interactions, or coordinate bonds [4, 5]. This intricate interplay of forces is exemplified in hybrid perovskites, where a negatively charged inorganic framework acts as the *host*, encapsulating positively charged organic molecules that act as the *guests*. The opposite polarities of *guest* and *host* ensure charge neutrality and overall stability of the crystal formed in a manner similar to that in their inorganic counterparts. However, in these hybrid structures, the stable orientations of the *guest* molecules are significantly influenced by hydrogen bonding interactions with the *host*. For instance, in the case of MA/FAPbX₃ [1–3], these hydrogen bonds guide the *guest* molecules into specific orientations within the *host* framework. Moreover, as suggested by previous reports, [6] these interactions can cooperate over large length scales, leading to spatially correlated *guest* orientations and *host* distortions. This cooperativity manifests globally as a structural phase of the system. Hence, hybrid perovskites could indeed be viewed from the point of view of *guest-host* systems. While this perspective might be unconventional, it aligns well with established notions of *guest-host* complexes. Furthermore, such a perspective also serves as a conceptual framework wherein the response of the crystal to external perturbations can be rationalized in

terms of the responses of the individual *host/guest* components. For instance, it is quite insightful to analyze the T-P phase diagram of a hybrid perovskite in terms of the expected phases of the individual sub-lattices. This would allow us to identify any emergent phenomena in the coupled system. Identification of key *host* or *guest* features influencing the stability of a phase has the practical advantage of offering strategies to design/tune *guests* and/or *hosts*, which can extend the stability of a phase or even suppress it completely. Experimentally, this would correspond to strategies such as doping, encoding organic *guests* with desired functionalities, applying strain, etc. This would, in turn, provide the flexibility to tune their electronic and optical properties according to different requirements.

Along with electrostatic interactions, hydrogen bonds (H-bonds) and co-ordinate bonds between *host* and *guest* mediate their coupling resulting in various phases with variations in temperature. Usually, stability of such phases capable of accommodating *host* distortion is predicted by relative sizes of *host/guest* ions indicated by Goldschmidt tolerance factor (τ) [7]. In such stable OIHPs ($0.8 \leq \tau \leq 1.0$), the primary order of phase transitions [8] is associated with *host* sub-lattice (octahedral tilt modes) [9–13]. The orientational freedom of *guest* plays a secondary role [8, 14] in the overall phase transition through an order-disorder mechanism [15]. *Guest*-reorientation rate controlled by the activation barrier between two stable hydrogen-bonded orientations of the *guest*, can be regulated by tuning the *host* or *vice-versa* [16, 17]. However, for a given *guest*, the trend may be different depending upon several parameters, such as hydrogen bond strength, electronegativity, and polarizability of the *host* [18, 19]. Alternatively, tuning the cation size, as shown mostly in mixed halide perovskites, can also modify the reorientation rate [20, 21]. Hence, tuning the *guest/host* chemistry can provide control over

the driving force of structural phase transitions in OIHPs.

To understand the effect of *guest* sizes, we classify OIHPs into normal-tolerant and over/super-tolerant perovskites, depending on whether τ remains within the conventional range or not. The phase transition temperature generally increases with the tolerance factor in a given series with varying *guests*, which is indicative of stronger interaction between the *guest* and the *host* for higher τ (Tables S1–S3). Usually, in normal-tolerant perovskites, significant *host* transition barrier (defined here as the difference in energies of phases with distorted and undistorted *host* lattice) implies their primary role in the phase transition mechanism. However, if the transition barrier of *guest* is more than the *host* barrier, *guest* orientation can decide *host* geometry, resulting in the reversal of the roles played by both sub-lattices. Strong coupling leads to locking of *guest* orientations, usually seen in OIHPs with relaxed τ and decreased dimensionality owing to the presence of large *guest* molecules [22]. This can also give rise to a polar/ferroelectric order, thereby facilitating electron-hole separation [23, 24]. Consequently, these materials are potential candidates for photovoltaics [25–29].

Such polar order in OIHPs is known to arise primarily due to the *guest* dipoles through both translational and rotational modes [30]. They also cause polar distortions in *host*-octahedra [31–33] as a “primary effect”, whose contribution to total polarization is usually small [34]. In the limit of strong *host/guest* coupling, a significant *host* distortion can further affect the *guest* polarization as a “secondary effect” which can be termed as “feedback polarization”, that has so far not been reported. Thus, segregating the contributions of all these components is essential in order to tune the polarization.

Recently, a new series of 3D-OIHP MHyPbX_3 ($\text{MHy}=\text{methylhydrazinium}$, $\text{X}=\text{Br/Cl}$) has been synthesized [35–39], despite leading to breakdown of conventional tolerance factor (τ) criteria due to the large ionic radius of the *guest*. MHyPbCl_3 undergoes an order-to-order transition from a low temperature (LT) less polar monoclinic ($P2_1$, Phase-II) to a high temperature (HT) more polar orthorhombic phase ($Pb2_1m$, Phase-I) at ~ 342 K, thus showing polarity at room-temperature. The absence of proper ferroelectric behavior was demonstrated through the fact that no switching of polarization was observed on switching of external electric field. The closed polarization-electric field (P-E) loop originates from the conductivity of the sample. X-ray diffraction data also consistent with this observation since it shows that the transition from $Pb2_1m$ to $P2_1m$ is a $mm2F2$ type transition, which is not a ferroelectric one. Therefore, the inability of reversible switching of MHy^+ cation upon application of an external field suggests that the MHy^+ hybrid systems may exhibit improper ferroelectric behavior. Interestingly, MHyPbCl_3 decomposes (~ 490 K) before a transition to a non-polar disordered state, unlike other conventional OIHPs or even MHyPbBr_3 [35, 36]. The individual roles of *host/guest*

and their coupling in stabilizing the polar phases are as yet unclear. Particularly, the presence of a large *guest* can have a significant role in the phase transition mechanism through modification of the rotational energy barrier.

Following these crucial observations from the experiments, we employ first-principles density functional theoretic (DFT) calculations on MHyPbCl_3 to understand the primary order parameter responsible for driving the structural phase transition. We find that, unlike prototypical analogs, a relatively high *guest*-reorientation barrier supports the primary role of the *guest* in driving the transition in this strongly coupled system. We confirm this result by quantifying the relative extents of *host* and *guest* participation along the minimum energy path connecting the two phases. Secondly, in contrast to the previous claims [36], we find that the *host* is primarily responsible for the polarization enhancement with temperature making the system an improper ferroelectric. [36] Using maximally localized Wannier functions (MLWFs) we not only unequivocally establish the dominant contribution of the *host* to the polarization enhancement but also show that the *host* distortion accompanying the transition induces a positive polarization feedback of $\sim 9\%$ on the *guest* ions. This feedback manifests itself through modulation of *guest* states at the band edges, which are usually dominated by the *host* contributions. Such a mechanism allows the direct influence of the organic *guest* in tuning the electronic and optical properties of over-tolerant OIHPs, making them appealing for optoelectronic applications.

II. RESULTS AND DISCUSSION

A. Structural optimization

The structures of both Phase-I and Phase-II of MHyPbCl_3 were fully relaxed at 0 K, starting from the respective experimental structures. The van der Waals correction is accounted for by including Grimmes D2 functional [40, 41]. The lattice parameters thus obtained match well with experimental values within accepted tolerance of $\pm 5\%$ [42, 43] irrespective of the choice of exchange-correlation (XC) functional (Table S4, also see Eq. S.2, Table S5 and Table S6). However, we chose to work with PBEsol [44] as it not only predicts the relative order of lattice constants ($a < b < c$ for Phase-II) accurately, but also has been preferred in other halide perovskites [45–48].

The optimized structures (Fig. 1) of the two phases differ in both the *guest* (MHy^+) orientation and the *host* (PbCl_6 octahedra) distortion, confirming orthorhombic structure ($Pb2_1m$) for Phase-I and monoclinic ($P2_1$) for Phase-II, similar to experiment [36]. Phase-II is the ground state at 0K, being lower in energy than Phase-I by ~ 45 meV/f.u.

We define a few parameters to distinguish the

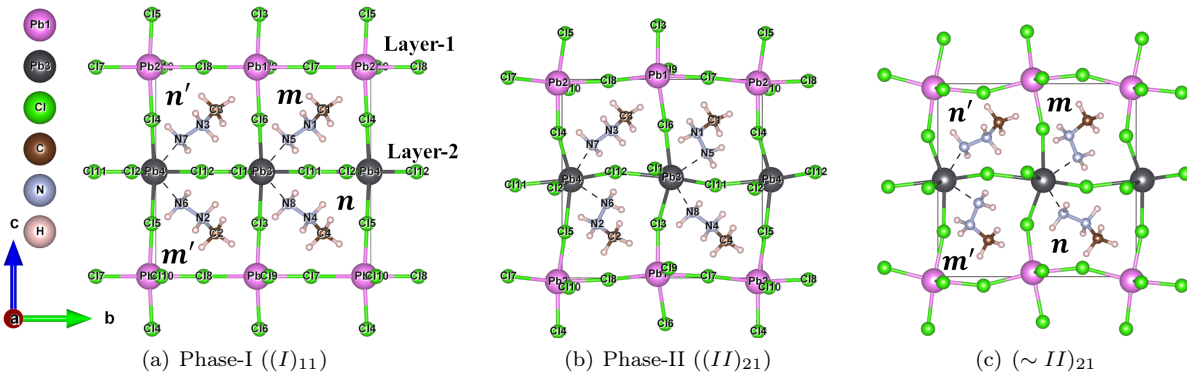


FIG. 1. Fully optimized structures of MHyPbCl₃ for both the experimental phases. Pink Pb atoms correspond to the less distorted octahedral layer (Layer-1) and grey Pb atoms to the more distorted octahedral layer (Layer-2). (c) Phase-II optimized under the constraints of Phase-I lattice parameters.

host/guest configurations between different phases, as shown schematically in Fig. 2. We assign Glazer notation of $a^0b^-c^-$ to Phase-I since the *host* tilting about a -axis is very small (nearly 0) compared to ideal perovskite (as shown in Fig. S2(c) and Fig.S2(d)). Similarly, Phase-II has a Glazer notation of $a^+b^-c^-$. Hence, the octahedral tilting transition $a^0b^-c^- \rightarrow a^+b^-c^-$ is seen from Phase-I to Phase-II. However, two alternate layers of octahedra are identified along crystal c -axis in both phases due to coordinate bonds between the *guest* and the *host*, layer-1 being less distorted (pink atoms in Fig. 1 and pink octahedra in Fig. S4) and layer-2 being more distorted (grey Pb atoms and grey octahedra) [36]. The difference in the two layers is shown by the variation in the bond lengths, $d_{\text{Pb-Cl}}$ and *host* tilting angles, $\delta\theta_{\text{tilt}}$ and $\delta\theta_{\text{gl}}$ (defined in Eqs. S.4–S.6 and shown in Fig. 2 and Fig. S2) for different structures under consideration. In Phase-II (Fig. 1(b)), half of the MHy sitting alternately along b and c axes (or at $m - m'$), gets significantly reoriented from Phase-I, whereas those at $n - n'$ are similar to Phase-I. The *host* and the *guest* configurations have been defined in Sec. S-II and have been tabulated for different structures (Table S10).

As any phase can differ by at least one of the *host/guest* sub-lattices, we employ the following nomenclature for identifying the structural differences in those components:

$$(Host)_{\text{Guest}(m-m'), \text{Guest}(n-n')}$$

Here, the first symbol (Roman numeral) denotes the *host* tilting ($\delta\theta_{\text{tilt}}$ close to either Phase-I or Phase-II), whereas the numbers in the subscript correspond to the *guest* orientation at $m - m'$ and $n - n'$ sites, respectively (Fig. 1(a)). Structures with *guest* orientation within 10° of either phase are classified as being in that phase. Thus, Phase-I and Phase-II are indicated by $(I)_{11}$ and $(II)_{21}$, respectively. Additionally, the ‘ \sim ’ symbol before the phase denotes a constraint on the *host* lattice parameters. For example, $(\sim II)_{21}$ corresponds to a structure

with Phase-I lattice parameters, but the *host* distortions and *guest* orientations are similar to Phase-II. Such an optimization was deemed necessary to compare the structural, electronic, and polar properties of the two phases at the same volume. The relevant parameters are defined in Fig. 2 and have been tabulated for different structures in Table S10.

B. Structural phase transition

1. Host/Guest coupling

Electronic properties, such as the band gaps, in OIHPs are governed significantly by the *host* atoms because of their high density of states near the band-edges [49]. The band gaps can, thus, be modulated by having a control over the *host* distortion which, in turn, is affected by the *guest/host* coupling. In other analogs, it has been found that the *guest* and *host* act cooperatively, [50] referred to as the ‘chicken (*guest*)-and-egg (*host*) paradox of the organic-inorganic interaction’. We expect that in MHyPbCl₃, being a super-tolerant stable perovskite, the HG coupling should be quite strong (which has been quantified in Sec. SIII A, and compared across different *guests* in Table S8). Hence, the impact of *guest* on the *host* should be more significant in comparison to other analogs. Therefore, understanding the phase transition mechanism in such a system would be quite interesting.

To this end, we performed a series of structural relaxations starting from different geometries and imposing constraints as required. As indicated above, full structural optimizations starting from experimental structures of HT and LT phases resulted in the $(I)_{11}$ and $(II)_{21}$ structures, respectively, which retained the corresponding experimental configurations of the *host* and *guest*. We note here that the optimized $(I)_{11}$ was nevertheless found to be dynamically unstable, a point we will explore in more detail later. Interestingly, when the *guest* configurations of the two phases were interchanged, the

modified HT structure ($(I)_{21}$) yielded the LT structure upon full optimization. In contrast, upon optimization, $(II)_{11}$ retained nearly the same *host* and *guest* configurations, without any significant *guest* reorientation irrespective of whether lattice parameters were allowed to relax (see Fig. S3 and Fig. S4, and Table S11). However, starting an optimization from $(I)_{21}$ at fixed lattice parameters yielded $(\sim II)_{21}$, a structure with Phase-II-like *host* distortions as well as *guest* orientations (shown in Fig. 1(c)). Together with the fact that optimization starting from $(I)_{11}$ yielded the Phase-I structure, this implies that *host* distortions are not energetically favoured without the *guest* reorienting to Phase-II configuration. Hence, the *guest* reorientation acts as a driving force for the structural transition, making it the primary order parameter. The interplay between *guest* and the *host* for this system is contrary to what has been reported for perovskites with smaller tolerance factors, ($A=MA^+$, FA^+ ; $B=Pb$, Sn , etc.) [15, 51] because of the inability of MHy^+ to rotate freely in the cubooctahedral void of the *host*. This has also been confirmed later in this work by the presence of relatively high rotational energy barriers for the switching between the two phases. A one-to-one correspondence between the *guest* orientation and the *host* distortion, as shown in Fig. S6 and Fig. S7 suggest the involvement of a complex order parameter, which could involve significant contributions from both the *guest* reorientation (predominantly) as well as the *host* distortion indicating a strong *guest/host* coupling.

A further confirmation regarding the primary role of the *guest* reorientations in driving the transition is obtained by quantifying the *guest* reorientational barrier encountered during transition and the relative contribution of the two sub-lattices along the minimum energy path (MEP) of transition. For this and other investigations described below, we compare $(I)_{11}$ and the constrained Phase-II, $(\sim II)_{21}$, obtained by the optimization of $(I)_{11}$ at fixed lattice parameters (Fig. 1(c)). This becomes specifically important for polarization calculations since the polarization quantum depends on the lattice parameters [52].

2. Guest-reorientational energy barrier and Transition Character

To estimate the rotational energy barrier of the *guest*, the *guest* is transformed between its orientations in the two phases using a combination of rotational and translational coordinates (R and T matrices). The details of the transformation are mentioned in Sec. S-IV A. This can be used to disentangle the *host* and *guest* sub-lattices, as was done to separate the contributions of MA^+ and inorganic BX_3 to polarization [53].

Fig. 3(a) estimates the rotational energy barrier due to the orientational pattern of the *guest* in $(I)_{11}$ and $(\sim II)_{21}$ which is around 0.3 eV/unit. This is obtained through Climbing Image-Nudged Elastic Band (CI-NEB)

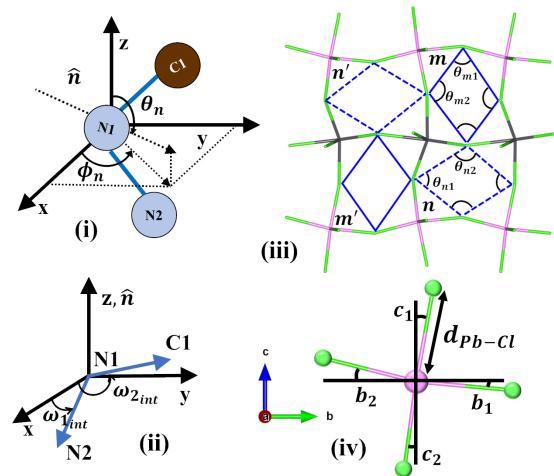


FIG. 2. (i)-(ii) Parameters to describe the *guest* orientation, (iii) *host*/octahedral tilting angle, $\delta\theta_{tilt}$, measured as the average deviation from 90 of the internal angles θ , and (iv) alternate measure for tilting angle in terms of Glazer angles given by $\delta\theta_{gl} = (|b_1| + |b_2| + |c_1| + |c_2|)/4$ and *host* distortion indicated by the rms deviation of bond lengths, δd_{Pb-cl} .

along the path determined by the rotation of the *guest* in fixed cell parameters of Phase-I. This path is referred to as fixed-cell NEB (fc-NEB). This high value of the barrier prevents the reorientation of *guest* at 0 K irrespective of the starting structure. This also explains why the high temperature phase, Phase-I, remains intact even after cell optimization. The variation in the *host* tilting pattern and the *guest* orientation has been tabulated in Table S9 for the path obtained by fc-NEB. The *host* variation (plotted in Fig. S11(b)) shows that the *host* stabilizes in its Phase-II-like octahedral pattern around the transition state (which is decided by the *guest* orientation), beyond which the optimization of any of the images would eventually lead to Phase-II. *Host* relaxation introduces a reduction in the rotational energy barrier, thereby facilitating its reorientation (Fig. S11(a)). To eliminate any effects due to the constraining of lattice parameters, the rotational energy barrier is also obtained by performing a variable-cell NEB from Phase-I to Phase-II (shown in Fig. S12). The energy barrier between the two orderings of the *guest* still is around 0.4 eV/unit which further confirms the inability of the molecule to reorient itself significantly irrespective of its starting configuration and the lattice parameters.

The driving force leading to structural phase transition can be quantified in terms of the relative contribution of the *guest* and *host* along MEP. For this, we define a parameter, Transition Character (TC), which is evaluated by the changes in the *guest* or *host* configuration as the transition progresses along the MEP. For the i^{th} image we define the *host* and *guest* parameters $\Delta\theta_{H,i}$ and $\Delta\theta_{G,i}$, respectively. Here, $\Delta\theta_{H,i}$ measures the differential change in $\delta\theta_{tilt}$ (see Fig. 2) normalized by total change

TABLE I. Relative energies of final structures obtained by optimization starting from different initial configurations to establish the primary role of *guest* in driving the structural phase transition. The optimization in the last row was performed, keeping the lattice parameters fixed at their values in Phase-I.

| Initial Configuration | Final Configuration | $\Delta E = E - E_{(II)_{21}}$ (meV/unit) |
|-----------------------|---------------------|--|
| $(I)_{21}/(II)_{21}$ | $(II)_{21}$ | 0.0 |
| $(I)_{11}$ | $(I)_{11}$ | 176.0 |
| $(II)_{11}$ | $(II)_{11}$ | 117.0 |
| $(I)_{21}$ | $(\sim II)_{21}$ | 143.0 |

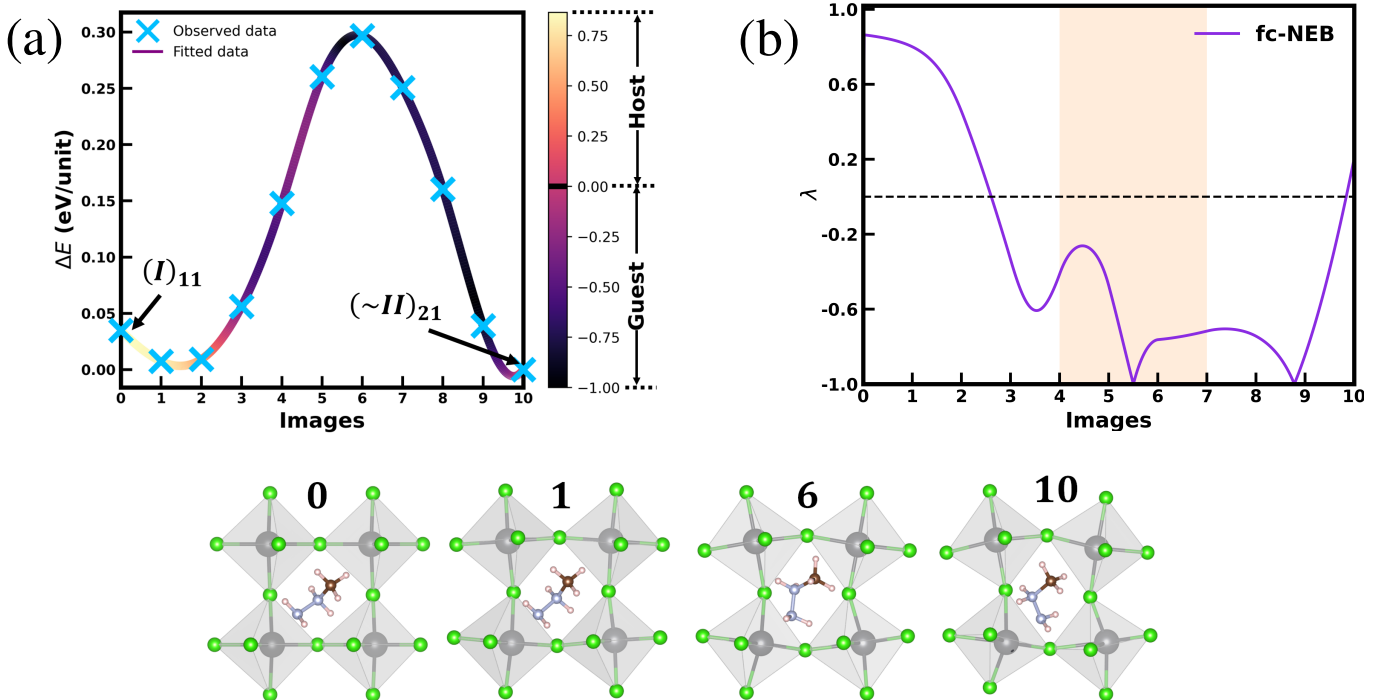


FIG. 3. (a) Energy barrier (fitted by spline interpolation) along minimum energy path (MEP) obtained from fc-NEB (fixed cell NEB) path in Phase-I lattice parameters), the color code indicates the primary involvement of either *guest* or *host* in different regions of the curve. The structures shown below are the initial (Phase-I), 1st (where *host* distortion is prominent), 6th (the transition point, *guest* reorientation is dominant) and the final images ($\sim II$)₂₁. They indicate some of the crucial points during the transition. (b) Transition character (TC), denoted by λ , as a function of the reaction coordinates along fc-NEB path. The values are derived from the interpolated data on θ_G and θ_H . The shaded region marks the region around the transition point which is *guest* dominated. The black dotted line (at $\lambda = 0$) demarcates the *host* and *guest* dominated regions.

in it across the transition. $\Delta\theta_{G,i}$ is calculated as

$$\Delta\theta_{G,i} = \sqrt{(\Delta\omega_{norm,i}^2 + \Delta\omega_{int,i}^2)} \quad (1a)$$

where $\Delta\omega_{norm,i}$ and $\Delta\omega_{int,i}$ are the differential changes in the molecular plane-normal and the internal angles of the *guest*, respectively, normalized by their overall change across the transition (see Sec. SIV B for details).

We now define a quantity called the transition character (TC), denoted by λ , as the difference between the rates of configurational changes of *host* and *guest* to the sum of their absolute values, as given by Eq. 2.

$$\lambda_i = \frac{(|\Delta\theta_{H,i}| - |\Delta\theta_{G,i}|)}{(|\Delta\theta_{H,i}| + |\Delta\theta_{G,i}|)}, \quad -1 \leq \lambda_i \leq 1 \quad (2)$$

Guest orientation predominates over *host* tilting for the regions where $-1 < \lambda < 0$, and *host* distortion is dominant for $\lambda > 0$, with both contributing equally at $\lambda = 0$.

Fig. 3(a) shows the energy barrier from Phase-I to ($\sim II$)₂₁ color-coded according to TC (the variation in TC is shown in Fig. 3(b) and Fig. S13(c)). The huge barrier seen is clearly associated with the *guest* rotational energy cost. Hence the transition is mostly governed by *guest*, thereby making it the primary order parameter of structural phase transition. The majority of the *host* transition occurs near the first image, involving a soft mode arising from the instability in $(I)_{11}$ earlier and as discussed below. vc-NEB from Phase-I to Phase-II structure also confirms the primary involvement of *guest*

around the transition point (Fig. S12, Fig. S13(b) and Fig. S13(c)). Additionally, in vc-NEB, the *host* involvement also becomes prominent along the transition path in comparison to fc-NEB. However, in either of the cases, transition is not achievable until the molecule rotates by a critical angle, i. e., *host* distortion alone cannot drive this phase transition.

3. Host-distortion

To analyze the interplay between *guest* and *host*, we need to understand the involvement of *host* as well. Therefore, we investigate the phonon dispersions of different structures of MHyPbCl₃ considered here. We find that all structures are dynamically stable within typical numerical accuracy (~ 0.3 THz) [54, 55] except for $(I)_{11}$ (Fig. S14 and Fig. S15). The latter displays an imaginary optical mode at Γ (Fig. S15(b)) originating on the *host* as is expected by a similar origin of low-frequency modes in other halide perovskites [35, 37, 55, 56]. Starting from this unstable Phase-I structure, each ion i is displaced by $\mathbf{u}_i(\eta)$ along the unstable optical mode, as is given by Eq. 3. Here x is the soft or the unstable mode eigenvector at Γ and η is the unitless displacement parameter [57].

$$\mathbf{u}_i(\eta) = \eta \cdot \mathbf{x}_{i\nu\Gamma}(\mathbf{q}_\Gamma) \quad (3)$$

The PES calculated along the soft/unstable eigenmode (Fig. 4) shows a local maximum at Phase-I with minima at $\eta = \pm 0.7\text{\AA}$, corresponding to a maximum atomic displacement of around 0.1\AA . A very small energy barrier of ≈ 1.4 meV/f.u. (which reduces to ≈ 0.36 meV/f.u. with hybrid-functionals (Fig. S15(b))) suggests that Phase-I results from dynamic disordering of the *host* over the two off-centred minima.

The structures of the two new energy equivalent minima are related by b -glide and are dynamically stable (Fig. S15(c)). They have similar distortion pattern as Phase-II (Fig. S16 and Fig. S17) without significant re-orientation of the *guest*, hence are labeled as $(\sim II)_{11}$. In either structure, the *host* picks up the tilting pattern of Phase-II, indicating that Phase-I should be characterized by permanent *host* distortions. However, the re-orientation of *guest* remains hindered because of the huge rotational energy barrier as is discussed earlier. This further is an evidence of the dominant role of the *guest* in driving the phase transition and confirmed by TC values along the transition path. The dynamical stability of the $(II)_{11}$ structure further confirms that the preferred state of the *host* is the ordered state, irrespective of the lattice parameters (Fig. S15(d)). Therefore, the experimental *host* must be dynamically disordered over the two stable *host*-distorted states, appearing as the experimental Phase-I structure on average.

The independent analysis of *guest* orientation as well as *host* distortion provides us an insight into the significant roles of each of them in phase transition. Fig. S18 summarizes the energy scales of all the structures that

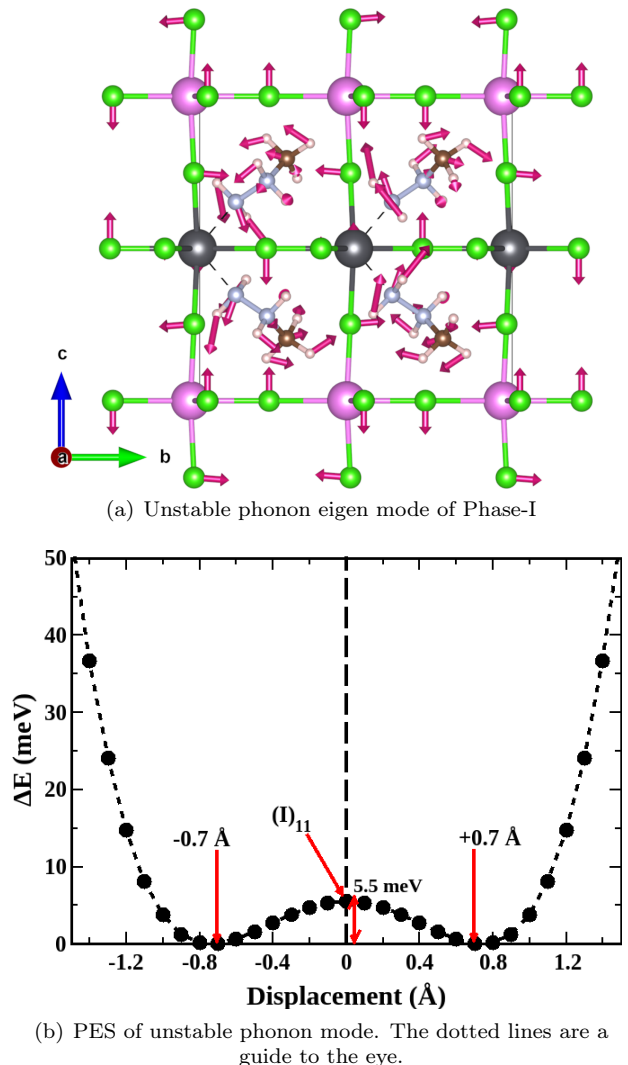


FIG. 4. Unstable phonon mode and PES of Phase-I. Magenta arrows in (a) show the magnitude of forces on each of the atoms in the unstable mode. PES of the unstable phonon mode in (b) show two new energy-minimum states. The transition of *host* of Phase-I to Phase-II occurs *via* this mode.

have been explored. The polar distortions can be induced in the *host* at finite temperatures by sufficiently large electric fields [58]. Likewise, it can be anticipated that applying an electric field in a suitable direction will induce an asymmetry in the PES of Phase-I of MHyPbCl₃, leading to the preferential stabilization of one structure over another. Consequently, the control over the stabilization of the disordered *host* within one of the ordered energy-minimum structures can be governed by the electric field. This can further lead to the development of extended hybrid networks with promising applications in ferroic-related fields.

C. Polarization

Another interesting feature in MHyPbCl_3 is the enhancement of polarization with the increase in temperature. *Guest*-driven transitions can indirectly induce polarization in the *host* through distortion. Here we probe into the origin and variation of polarization across different phases of this material to disentangle the *guest/host* contribution. Tuning these structural features may lead to enhancement of polarization in OIHPs, thus improving PCEs [53, 59, 60]. Here, we have employed Berry phase method [52, 61–63] as well as maximally localized Wannier functions (MLWF) [64–66] for the in-depth analysis of the polar order of MHyPbCl_3 . The polarization values are converged with respect to the number of k -points (Fig. S19). The values obtained from these two methods are in excellent agreement as reported in SI (see Table S12 and Table S13). The usage of the same lattice parameters (here, in Phase-I) ensures the same polarization quanta for different structural phases. Since the phase transition is *guest*-driven, we first look at the effect on total polarization solely due to *guest* re-orientation (at $m - m'$), by evaluating the net dipole moment/polarization in the absence (isolated dipoles, Fig. S20) and the presence of a fixed *host* (here, Phase-I). The isolated dipoles show a huge variation in the dipole moment (shown by diamond symbols in Fig. 5) and have the capability to induce large polarization. However, this is suppressed as soon as the *host* is introduced *via* polarization feedback to the *guest* (as discussed later). The effect of aforementioned *guest* reorientation in Phase-I *host* is captured through a pathway from $(I)_{11}$ to $(I)_{21}^c$, as shown in Fig. 5. Here, ‘c’ indicates that the *guest* at $n - n'$ and *host* are constrained in Phase-I, while the *guest* at $m - m'$ are in $(\sim II)_{21}$. This shows a net decrease in the total polarization of the combined *guest/host* system which could be due to three reasons: (1) Phase-II-like reorientation of isolated dipoles (red curve, $\Delta P = 1.55 \mu\text{C}/\text{cm}^2$), (2) Dipole-dipole interaction among the *guests* ($\Delta P = 0.12 \mu\text{C}/\text{cm}^2$) and (3) *Host* involvement, *i.e.* the electronic charge density around the *host* atoms induced by (1) ($\Delta P = 1.16 \mu\text{C}/\text{cm}^2$). These contributions are independent of whether the *guest* at $m - m'$ or $n - n'$ is rotated as seen from the symmetric dependence of ΔP in Fig. S21. Introducing *host* distortion in $(I)_{21}^c$ and optimization of the *guest* at $n - n'$ leads to the final structure, $(\sim II)_{21}$, which has an effective polarization of $-2.57 \mu\text{C}/\text{cm}^2$.

For a series of similar OIHPs, a polarization range of 1–40 $\mu\text{C}/\text{cm}^2$ has been reported and these values hugely depend on the orientation of the local dipoles [30, 53]. We find that MHyPbCl_3 lies well within this range, thus having the potential for modulating/enhancing optoelectronic properties at room-temperature, unlike other reported OIHPs.

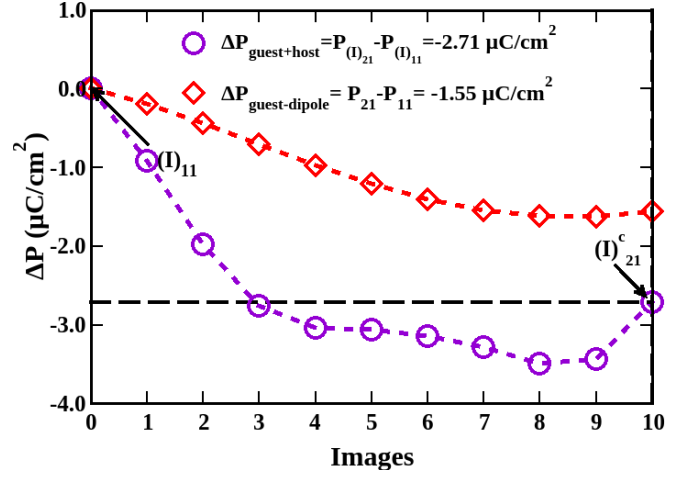


FIG. 5. Polarization difference (ΔP) for different images obtained by reorienting the *guest* at $m - m'$. This transformation takes the structure $(I)_{11} \rightarrow (I)_{21}^c$, where ‘c’ indicates that the *guest* at $n - n'$ and *host* are constrained in Phase-I, while the *guest* at $m - m'$ are in $(\sim II)_{21}$. The red curve (diamond symbols) is for isolated dipoles placed in a positive background; the violet (circular symbols) is for the *guest* in the presence of Phase-I *host*. The dotted lines are a guide to the eye.

1. Disentangling different components of polarization

Various components of OIHPs can contribute to the polarization change, including *guest*-reorientation, *host*-distortion, and *guest/host* coupling. The interplay of the *guest* and *host* of MHyPbCl_3 cannot be ignored because of their synergistic roles in phase transitions due to the strong HG coupling. Hence, we use MLWFs to probe into the detailed mechanism regarding enhancement of polarization (For details, see Sec. S-V B). Wannier centers (WCs) for the relevant structures are shown by magenta-colored spheres in Fig. S24, which are used to extract the electronic polarization along with ionic contribution due to *guest* ordering as well as *host* configurations in different phases. Here, we have considered a path $(I)_{11} \rightarrow (I)_{21}^c \rightarrow (I)_{21} \rightarrow (\sim II)_{21}$ showing polarization change (Fig. 6) along the following sequence of events: (1) reorientation of the *guest* at $m - m'$ in Phase-I, (2) *guest* relaxation at $n - n'$ in Phase-I, and finally the (3) *host* distortion involved in the phase transition. The Phase-I $(I)_{11}$ has an absolute polarization of $8.96 \mu\text{C}/\text{cm}^2$ coming from both ionic and electronic components, which are all set to zero individually for referencing. In the final Phase-II $(\sim II)_{21}$ structure, *host* plays the dominating role in changing the polarization ($> 90\%$), with only a nominal contribution from *guest*. On the other hand, the unrelaxed intermediate structure $(I)_{21}^c$ significantly reduces the polarization due to $m - m'$ -reorientation ($\Delta P_{\text{guest}} = -1.54 \mu\text{C}/\text{cm}^2$), having slightly larger contributions than the octahedral *host* ($\Delta P_{\text{host}} = -1.16 \mu\text{C}/\text{cm}^2$), as seen in Fig. 6. This might seem to agree with the experimental suggestion of *guest*

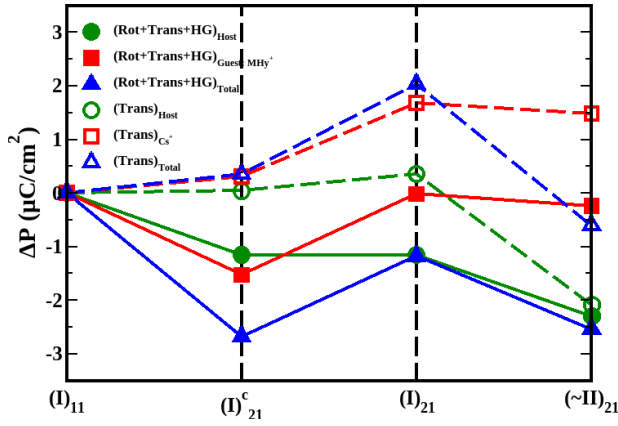


FIG. 6. Net polarization in MHyPbCl₃ across the path: $(I)_{11} \rightarrow (I)_{21}^c \rightarrow (I)_{21} \rightarrow (\sim II)_{21}$. Solid symbols represent total (blue), *host* (green), and *guest* (red) contributions to change in polarization in MHyPbCl₃. The open/hollow symbols represent the same contributions in CsPbCl₃. Organic *guest* is substituted by an isotropic, rigid inorganic entity so as to separate out the translational component from the rotational and HG-coupling term that exists for an organic *guest*. The lines are a guide to the eye.

playing the major role in polarization enhancement [36]. However, as seen in Fig. 7(b), further relaxation from the unrelaxed intermediate to relaxed-intermediate structure $((I)_{21}^c \rightarrow (I)_{21})$ slightly affects the $m - m'$ contribution ($-0.04 \mu C/cm^2$), whereas changes the atomic positions at $n - n'$ significantly. The resultant polarization due to $n - n'$ ($1.54 \mu C/cm^2$) cancels the $m - m'$ contributions, thus effectively ruling out the role of the *guest* in polarizing Phase-I. The same behavior is also seen in Phase-II (Fig. 7(b) and Fig. S27). Thus, despite *guest* being the primary order of the structural phase transition, it is the *host* that plays a dominant role in polarizing the system. Our finding contrasts the suggestions from experiments [36], where the separation of roles of *host/guest* in phase-transition and polarization was beyond the scope without the help of computational approach.

To segregate the effects of rotation and *guest/host* coupling from translational contribution to polarization, each of the MHy⁺ ions are replaced by the inorganic atom, here, Cs⁺ at its center of mass. This also helps in filtering out the effect solely due to the translation of the dipole. Fig. 6 demonstrates the exclusive role of rotation and HG coupling in drastically changing ΔP unlike translation ($1.48 \mu C/cm^2$) as in the inorganic halide perovskites. However, this translational contribution is suppressed due to its opposite nature of polarization with respect to contribution from *guest*-reorientation and HG coupling. Next we look at the atomic contributions of the *host* as it is responsible for $\sim 90\%$ total polarization change ($2.57 \mu C/cm^2$) (Table S15 and Fig. 7(a), Fig. 7(c), and Fig. S30) which is quite significant in terms of the net polarization shown by similar OIHPs [30, 53]. We find that the collective effect of Pb displacements and the po-

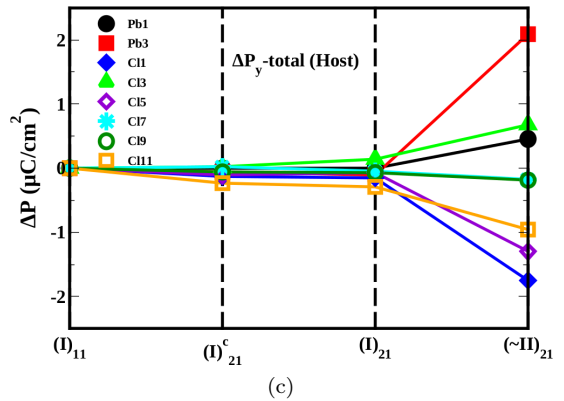
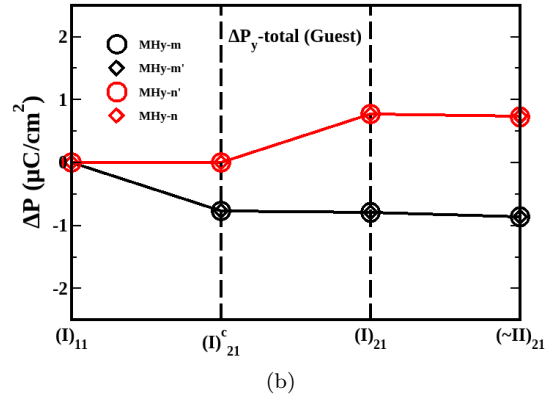
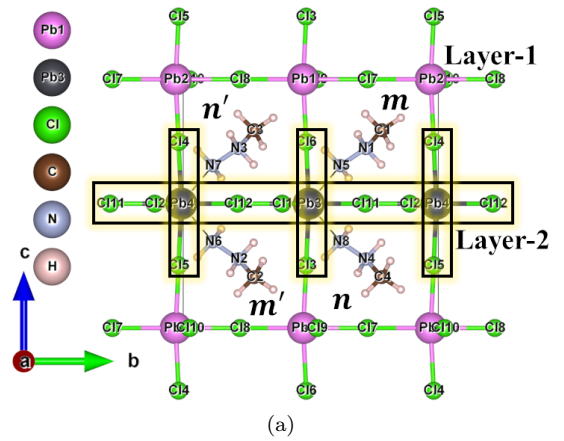


FIG. 7. (a) More distorted layer of the *host* (Layer-2 as highlighted in the figure) contributes to polarization change most significantly. Quantification of the y -component of total polarization of (b) *Guest*. (c) *Host*. Only y -component contributes to polarization in all the cases.

larization of Cl electrons in the more distorted layer of the *host* (layer-2) (Fig. 7(c)) contributes the most towards enhancement of polarization as the structure transitions from $(\sim II)_{21} \rightarrow (I)_{11}$. Furthermore, we also find that out of the s and the d non-bonding electrons of Pb, the former plays the most significant role. This dominance of s lone pair was also highlighted recently in [31, 67] by showing that the lone-pairs around Pb-atoms are highly directional in nature.

2. Polarization feedback (Effect of the host on the guest)

So far, having investigated the effect induced on the *host* due to *guest* reorientation in terms of both structural and polar properties, we next ask if the *host* could further induce polarization in the *guest* due to phase transition from $(I)_{11} \rightarrow (\sim II)_{21}$. This effect is bifurcated into two primary contributions involving (1) *host* introduction and (2) *host* distortion.

To understand the former effect, we first consider only the *guest*-reorientation ($(I)_{11} \rightarrow (I)_{21}^c$, *i.e.*, 0^{th} and 10^{th} images in Fig. 5), where total polarization of isolated *guests* (dipoles) and the combined *guest/host* system are compared. This comparison at the final structure (10^{th} image) results in a polarization difference of $1.16 \mu\text{C}/\text{cm}^2$ because of *host* introduction. This is solely due to the electronic component as the ionic contributions are canceled through the same *guest* and *host* coordinates (see SI Sec. S-V C for details). This difference consists of two factors. The first one is the pure *host* electronic polarization as a primary effect, whereas the secondary effect of the *host* on *guest* electronic polarization is termed feedback polarization. The latter is computed by comparing the *guest* electronic polarization of the 10^{th} images in Fig. 5, which amounts to only $0.02 \mu\text{C}/\text{cm}^2$ (roughly 1% of the total polarization).

The second part of the feedback effect occurs when the *host* undergoes distortion. This is computed for the identical *guest* coordinates, which would eliminate any contributions from the ionic part of the *guest* polarization. The resultant change in the *guest* polarization, therefore, will only be due to the changes in the electronic cloud on the *guest* caused by *host* distortion. We achieve this by comparing the WCs associated with the *guest* in the structures, $(I)_{21}$ and $(\sim II)_{21}$. For this, we have first assigned the WCs to each atom, depending on whether they are bond-centered (B.C.) or atom-centered (A.C.). The WC type can be decided by the ratio of the distance of the WC from the two atoms it is in the closest proximity with. We suggest that, for MHyPbCl_3 , an atom-centered WC would have a ratio < 0.25 , while higher values of this ratio would imply a bond-centered WC. The shift in the WCs (Fig. 8) in the two structures would, hence, directly contribute to feedback polarization due to *host* distortion, defined as:

$$\delta(\Delta WC) = [(\Delta WC)_{(\sim II)_{21}} - (\Delta WC)_{(I)_{21}}] \quad (4)$$

where $(\Delta WC)_{(\sim II)_{21}} = (WC)_{(\sim II)_{21}} - \text{B.C./A.C.}$ for the $(\sim II)_{21}$ -structure.

We find that this feedback amounts to $-0.22 \mu\text{C}/\text{cm}^2$ (Fig. S32 and Table S17, exists only along *y*-direction, cancels out in other directions), which demonstrates a further reduction of net polarization in $(\sim II)_{21}$ ($\sim 9\%$ with respect to the total polarization). Since *host* distortion in itself is responsible for bringing down the polarization (as shown earlier), followed by a further reduction due to feedback effect, therefore the latter acts as

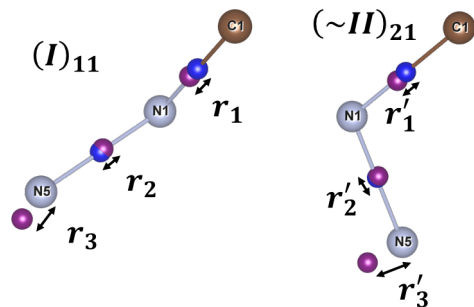


FIG. 8. Schematic representing shift in bond- and atom-centered WCs between *guest* ions of two structures. Here, we have taken one of the structures as $(I)_{11}$ for clearly demonstrating the shift in WCs between two structures. In actual, we have considered $(I)_{21}$, and $(\sim II)_{21}$ to calculate $\delta(\Delta WC)$. The violet and blue spheres represent the WCs and bond centers, respectively. r_1, r_2, r'_1, r'_2 are the distances with respect to the B.C., r_3 and r'_3 are the WC shift with respect to A.C.

positive feedback. This effect is significant given the relatively small polarization offered by OIHPs in general, which is distributed on the *guest* at $m - m'$ and $n - n'$ in a ratio of 1:0.2.

D. Coupling of polar and electronic properties

After probing the polar properties of MHyPbCl_3 and determining the elements that are critically involved in changing the polarization as the phase transition occurs, we now look at the correspondence between the polar and the electronic properties in terms of both *guest*, and *host*. (See SI Sec. S-VI for details related to band gaps).

First, we focus on the contribution from *host* atoms to electronic states. A one-to-one correspondence between polar and electronic properties is expected as the *host* dominates total polarization. Indeed, the *host* shows similar significant contributions in electronic structure. This is evident from PDOS (partial density of states), where the *p*-orbitals of Cl and Pb of the more distorted layer, *i.e.*, layer-2 (also responsible for polarization) affect the valence band significantly (Fig. S34 and Fig. S35) [49].

Secondly, we explicitly look at the effect on the *guest* density of states due to *host* distortion in the form of feedback polarization. This effect is rather unusual, as in general, the *host* atoms populate the band-edges in other OIHPs, whereas the organic cations have almost an insignificant contribution [51, 68]. However, here, we show that this large *guest*, MHy^+ (Fig. 9) directly affects the electronic properties through the polarization feedback by the *host*. Fig. 9 shows that the participation of the *guest* atoms near the band edges gets affected substantially depending on the orientation of the molecule. For *guest* orientation similar to Phase-II and Phase-I, *guest* DOS increases with the decrease in feedback polarization in both cases (Fig. 9(a) and Fig. 9(b), respectively). Although in the former, the feedback correlates positively

with *host* distortion, whereas in the latter, this correlation is negative. Thus, the effect of the *guest* on the electronic structure can be tuned by controlling feedback through *host* distortion in both phases of MHyPbCl₃. This feedback on the *guest* at the band edges has direct effects on quasiparticle band gaps and exciton binding energies of 3D hybrid perovskites. Such direct roles are recently discovered in 2D perovskites but the mechanism through feedback is not yet explored [69–72]. The orientation and packing of the *guest* also guide the *host* configuration as well as the extent of metal-halide orbital overlap, thus also affecting the electronic structure indirectly. A recent study showed the influence of the *guest* on material response, such as phase transitions, photoluminescence emission, etc. [73]. The compositions with linear spacers undergo distinct phase transitions, whereas cyclic spacers (having large steric hindrances) lack first-order transition for the investigated temperature range. Additionally, both of them show similar photo-luminescence properties. Therefore, modulation of the spacer/*guest* ion can lead to a larger structural and thermal phase space availability, thereby enhancing the functionalization and applicability of OIHPs.

E. Conclusions

This work investigates the driving force behind the structural phase transition and the origin of polarization enhancement with increase in temperature in the super-tolerant and strongly coupled member of hybrid halide perovskite, MHyPbCl₃, from the perspective of *host/guest* system. The *guest* reorientation, quantified by comparing barriers between the two phases, $(I)_{11}$ and $(\sim II)_{21}$, emerges as the primary order parameter. The substantial rotational barrier is also an indication of slow and sticky *guest* dynamics. A transition character, defined as λ , quantifies the *guest/host* contribution, highlighting the *guest* dominance. The *host* atoms are primarily responsible for polarization enhancement, with the *guest* contributing only minimally. The *host* atoms of the more distorted layer of octahedra are found to be considerably involved, thereby establishing a one-to-one correlation between structural and polar properties. An interesting positive feedback effect that the *host* induces on the *guest* polarization is observed. This would mean that as the system transitions from a more to a less distorted state ($(\sim II)_{21} \rightarrow (I)_{21}$), there is an enhancement of polarization due to *guest*-reorientation through the *host* distortion. As a consequence of this, the *host* further induces a polarization on *guest*, leading to a secondary enhancement. This feedback is also coupled with the energy levels of the *guest* at the band edges and is dependent on the starting *guest* orientation. This suggests that *guest* tunability can directly influence electronic and optical properties in over-tolerant perovskites. Hence, these systems offer viable alternatives for improved photovoltaic applications.

III. COMPUTATIONAL DETAILS

Self-consistent total-energy calculations were carried out for different structures using ultrasoft pseudopotential [74]. The lattice parameters were compared with the experimental values using two Generalized Gradient Approximation (GGA) exchange-correlation energy functionals, PBE [75] and PBE functional revised for solids (PBEsol) [44] as implemented in Quantum-ESPRESSO (QE) computational package [76, 77]. The corrections due to dispersion interactions in density functional theory (DFT) were employed through the second-generation (D2) van der Waals (vdW) corrections proposed by Grimme [40, 41].

For ultrasoft pseudopotentials, the electronic wave functions were expanded in plane waves upto a charge density cut-off of 480 *Ry* and a kinetic energy cut-off of 80 *Ry*. A cut-off of $4 \times 2 \times 2$ Monkhorst-Pack *k*-point mesh was chosen for Brillouin zone integration depending on the ordering of the lattice parameters. The structures were relaxed until the Hellmann-Feynmann forces were less than 0.026 *meV/Å*. Polarization calculations were done using the Berry phase approach with 10 *k*-points along each direction [52, 61–63]. Phase-I is taken as the reference for the polarization of all structures. Maximally localized Wannier functions were obtained to evaluate polarization using WANNIER90 code [64, 65, 78] integrated with QE. Wannier functions were generated using only valence bands, with a convergence criterion of 10^{-10}Å^2 . The starting projections included *s*, *p* and *d* orbitals for Pb, *p* for Cl, *sp*³- hybridization for C, *sp*³ for each of terminal N atoms and *s*- orbital for the two H-atoms bonded with middle nitrogen of each MHy-ion. Hybrid-PBE0 functional [79, 80] was also used to verify the lattice parameters and the difference in energies between the two phases, all implemented in VASP [81–83] using the projector augmented wave (PAW) pseudopotential [84]. For PAW-pseudopotentials, kinetic energy cut-off 750 eV ($\approx 55 \text{ Ry}$) and *k*-mesh cut-off same as that of ultrasoft pseudopotential was chosen. The phonon dispersion curves for the structures were obtained using *ab initio* lattice dynamics with the finite displacement method on a $2 \times 2 \times 2$ supercell with PHONOPY package [85]. On the optimized *guest* coordinates for different structures, we used Gaussian 16 program package [86] implementing density functional three-parameters hybrid, B3LYP methods [87, 88] with the 6-311G(2d,2p) [89–91] basis set for evaluating polarization solely due to the *guest*. Climbing Image-Nudged Elastic Band (CI-NEB) has been performed using VASP to determine the path of phase transition and the corresponding energy barrier.

ACKNOWLEDGMENTS

The authors gratefully acknowledge computational resources provided by IISER Bhopal as well as “PARAM Shivay” at Indian Institute of Technology (BHU),

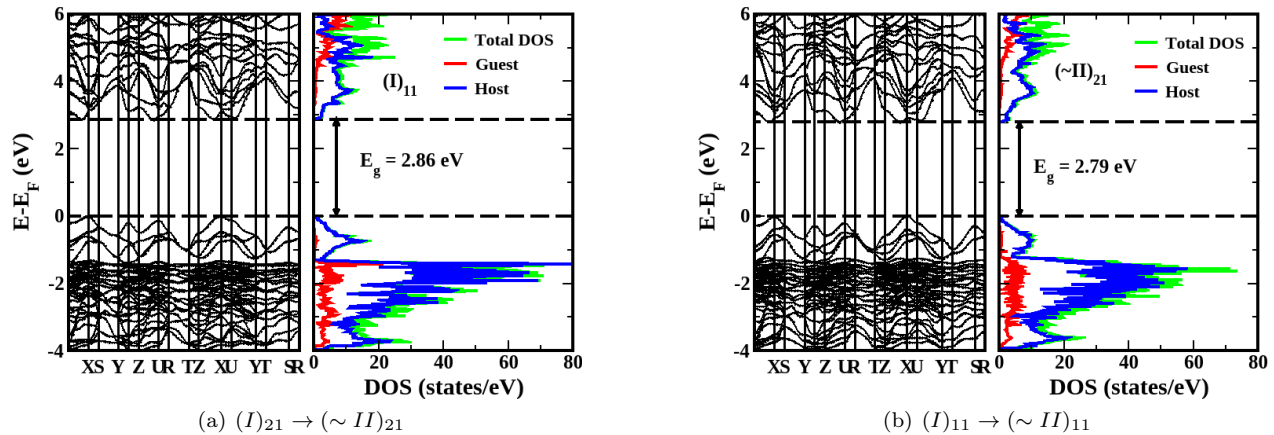


FIG. 9. Effect of polarization feedback (due to *host* distortion) on the energy levels of *guest* (MHy-ions) near the band-edges for orientation of the *guest* in both the phases, Phase-I and Phase-II.

Varanasi, which is implemented by C-DAC and supported by the Ministry of Electronics and Information Technology (MeitY) and the Department of Science and Technology (DST), Government of India, through Na-

tional Supercomputing Mission (NSM). P.S. acknowledges funding through UGC-JRF (India) for carrying out the Ph.D. program. S.M. acknowledges funding through the Integrated Ph.D. program at IISER Bhopal.

-
- [1] Michael M Lee, Joël Teuscher, Tsutomu Miyasaka, Takuro N Murakami, and Henry J Snaith. Efficient hybrid solar cells based on meso-superstructured organometal halide perovskites. *Science*, 338(6107):643–647, 2012.
- [2] Wei-Jian Xu, Svitlana Kopyl, Andrei Kholkin, and João Rocha. Hybrid organic-inorganic perovskites: Polar properties and applications. *Coord. Chem. Rev.*, 387(0):398–414, 2019.
- [3] GA Petersson, Andrew Bennett, Thomas G Tensfeldt, Mohammad A Al-Laham, William A Shirley, and John Mantzaris. A complete basis set model chemistry. i. the total energies of closed-shell atoms and hydrides of the first-row elements. *J. Chem. Phys.*, 89(4):2193–2218, 1988.
- [4] Hugh P Ryan, Zachary S Fishman, Jacob T Pawlik, Angela Grommet, Malgorzata Musial, Felix Rizzuto, James C Booth, Christian J Long, Kathleen Schwarz, Nathan D Orloff, et al. Quantifying the effect of guest binding on host environment. *Journal of the American Chemical Society*, 145(36):19533–19541, 2023.
- [5] Sadaf Bashir Khan and Shern-Long Lee. Supramolecular chemistry: Host–guest molecular complexes. *Molecules*, 26(13):3995, 2021.
- [6] Sayan Maity, Suraj Verma, Lavanya M Ramaniah, and Varadharajan Srinivasan. Cooperative octahedral tilt modes drive coexisting displacive and order–disorder pressure-induced phase transitions in mapbbr3. *The Journal of Physical Chemistry C*, 2024.
- [7] Bayrammurad Saporov and David B Mitzi. Organic–inorganic perovskites: Structural versatility for functional materials design. *Chem. Rev.*, 116(7):4558–4596, 2016.
- [8] RA Cowley. Structural phase transitions i. landau theory. *Adv. Phys.*, 29(1):1–110, 1980.
- [9] Mirosław Mączka and Maciej Ptak. Temperature-dependent raman studies of FAPbBr₃ and MAPbBr₃ perovskites: Effect of phase transitions on molecular dynamics and lattice distortion. *Solids*, 3(1):111–121, 2022.
- [10] Jiawei Wu, Jianfu Chen, and Haifeng Wang. Phase transition kinetics of mapbi3 for tetragonal-to-orthorhombic evolution. *J. Am. Chem. Soc. Au*, 3(4):1205–1212, 2023.
- [11] Wissam A Saidi and Joshua J Choi. Nature of the cubic to tetragonal phase transition in methylammonium lead iodide perovskite. *J. Chem. Phys.*, 145(14):144702, 2016.
- [12] Bernard Hehlen, Philippe Bourges, Benoît Rufflé, Sébastien Clément, Rémy Vialla, AC Ferreira, Claude Ecolivet, Serge Paofai, Stéphane Cordier, Claudine Katan, et al. Pseudospin-phonon pretransitional dynamics in lead halide hybrid perovskites. *Phys. Rev. B*, 105(2):024306, 2022.
- [13] Jia-Bin Li, Zhi-Kang Jiang, Rui Wang, Jin-Zhu Zhao, and Ruiqiang Wang. Ferroelectric order in hybrid organic-inorganic perovskite nh4pb3 with non-polar molecules and small tolerance factor. *NPJ Comput. Mater.*, 9(1):62, 2023.
- [14] K Parlinski. Secondary order parameters in the structural phase transitions. *Zeitschrift Für Physik B Condensed Matter*, 58(0):245–250, 1985.
- [15] Sayan Maity, Suraj Verma, Lavanya M Ramaniah, and Varadharajan Srinivasan. Deciphering the nature of temperature-induced phases of mapbbr3 by ab initio molecular dynamics. *Chem. Mater.*, 2022.
- [16] Mantas Simenas, Sergejus Balciunas, Sarunas Svirskas, Martynas Kinka, Maciej Ptak, Vidmantas Kalendra, Anna Gągor, Daria Szewczyk, Adam Sieradzki, and Robertas Grigalaitis. Phase diagram and cation dynamics of mixed ma(1-x)fa(x)pbbr3 hybrid perovskites.

- Chem. Mater.*, 33(15):5926–5934, 2021.
- [17] Dominik J Kubicki, Daniel Prochowicz, Albert Hofstetter, Peter Pechy, Shaik M Zakeeruddin, Michael Gratzel, and Lyndon Emsley. Cation dynamics in mixed-cation (ma) x (fa) 1-x pbi3 hybrid perovskites from solid-state nmr. *J. Am. Chem. Soc.*, 139(29):10055–10061, 2017.
- [18] VK Sharma, R Mukhopadhyay, A Mohanty, V Garcia Sakai, M Tyagi, and DD Sarma. Influence of the halide ion on the a-site dynamics in fapb x 3 (x= br and cl). *J. Phys. Chem. C*, 126(16):7158–7168, 2022.
- [19] Oleg Selig, Aditya Sadhanala, Christian Muller, Robert Lovrincic, Zhuoying Chen, Yves LA Rezus, Jarvist M Frost, Thomas LC Jansen, and Artem A Bakulin. Organic cation rotation and immobilization in pure and mixed methylammonium lead-halide perovskites. *J. Am. Chem. Soc.*, 139(11):4068–4074, 2017.
- [20] Eve M Mozur and James R Neilson. Cation dynamics in hybrid halide perovskites. *Annu. Rev. Mater. Res.*, 51(0):269–291, 2021.
- [21] Debayan Mondal and Priya Mahadevan. Structural distortions in hybrid perovskites revisited. *Chem. Mater.*, 2024.
- [22] Yongping Fu, Matthew P Hautzinger, Ziyu Luo, Feifan Wang, Dongxu Pan, Michael M Aristov, Ilia A Guzei, Anlian Pan, Xiaoyang Zhu, and Song Jin. Incorporating large a cations into lead iodide perovskite cages: Relaxed goldschmidt tolerance factor and impact on exciton-phonon interaction. *ACS Cent. Sci.*, 5(8):1377–1386, 2019.
- [23] Shi Liu, Fan Zheng, Nathan Z Koocher, Hiroyuki Takenaka, Fenggong Wang, and Andrew M Rappe. Ferroelectric domain wall induced band gap reduction and charge separation in organometal halide perovskites. *J. Phys. Chem. Lett.*, 6(4):693–699, 2015.
- [24] Tejas S Sherkar and L Jan Anton Koster. Can ferroelectric polarization explain the high performance of hybrid halide perovskite solar cells? *Phys. Chem. Chem. Phys.*, 18(1):331–338, 2016.
- [25] Bo Chen, Jian Shi, Xiaojia Zheng, Yuan Zhou, Kai Zhu, and Shashank Priya. Ferroelectric solar cells based on inorganic-organic hybrid perovskites. *J. Mater. Chem. A*, 3(15):7699–7705, 2015.
- [26] Ajay Kumar Jena, Ashish Kulkarni, and Tsutomu Miyasaka. Halide perovskite photovoltaics: Background, status, and future prospects. *Chem. Rev.*, 119(5):3036–3103, 2019.
- [27] Martin A Green, Anita Ho-Baillie, and Henry J Snaith. The emergence of perovskite solar cells. *Nat. Photonics*, 8(7):506–514, 2014.
- [28] Mingyu Jeong, In Woo Choi, Eun Min Go, Yongjoon Cho, Minjin Kim, Byongkyu Lee, Seonghun Jeong, Yimhyun Jo, Hye Won Choi, Jiyun Lee, et al. Stable perovskite solar cells with efficiency exceeding 24.8% and 0.3-v voltage loss. *Science*, 369(6511):1615–1620, 2020.
- [29] Minjin Kim, Jaeki Jeong, Haizhou Lu, Tae Kyung Lee, Felix T Eickemeyer, Yuhang Liu, In Woo Choi, Seung Ju Choi, Yimhyun Jo, Hak-Beom Kim, et al. Conformal quantum dot-sno2 layers as electron transporters for efficient perovskite solar cells. *Science*, 375(6578):302–306, 2022.
- [30] Shunbo Hu, Heng Gao, Yuting Qi, Yongxue Tao, Yongle Li, Jeffrey R Reimers, Menno Bokdam, Cesare Franchini, Domenico Di Sante, Alessandro Stroppa, et al. Dipole order in halide perovskites: Polarization and rashba band splittings. *J. Phys. Chem. C*, 121(41):23045–23054, 2017.
- [31] Xu Huang, Xiaotong Li, Yu Tao, Songhao Guo, Jiazhen Gu, Huilong Hong, Yige Yao, Yan Guan, Yunan Gao, Chen Li, et al. Understanding electron-phonon interactions in 3d lead halide perovskites from the stereochemical expression of 6s2 lone pairs. *J. Am. Chem. Soc.*, 144(27):12247–12260, 2022.
- [32] Malladi Srikanth, Mailde S Ozório, and Juarez LF Da Silva. Optical and dielectric properties of lead perovskite and iodoplumbate complexes: An ab initio study. *Phys. Chem. Chem. Phys.*, 22(33):18423–18434, 2020.
- [33] Sayan Maity, Suraj Verma, Lavanya M Ramaniah, and Varadharajan Srinivasan. Stabilizing polar domains in mapbbr3 via the hydrostatic pressure-induced liquid crystal-like transition. *J. Phys. Chem. Lett.*, 14:5497–5504, 2023.
- [34] Jarvist M Frost, Keith T Butler, Federico Brivio, Christopher H Hendon, Mark Van Schilfgaarde, and Aron Walsh. Atomistic origins of high-performance in hybrid halide perovskite solar cells. *Nano Lett.*, 14(5):2584–2590, 2014.
- [35] Mirosław Maczka, Maciej Ptak, Anna Gağor, Dagmara Stefańska, Jan K Zaręba, and Adam Sieradzki. Methylhydrazinium lead bromide: Noncentrosymmetric three-dimensional perovskite with exceptionally large framework distortion and green photoluminescence. *Chem. Mater.*, 32(4):1667–1673, 2020.
- [36] M. Maçzka, A. Gağor, J. K. Zaręba, D. Stefańska, M. Drozd, S. Balciunas, Šimėnas, J. M., Banyš, and A. Sieradzki. Three-dimensional perovskite methylhydrazinium lead chloride with two polar phases and unusual second-harmonic generation bistability above room temperature. *Chem. Mater.*, 32(9):4072–4082, 2020.
- [37] Mirosław Maçzka, Maciej Ptak, Daniel Linhares Militão Vasconcelos, Laisvydas Giriunas, Paulo Tarso Cavalcante Freire, Marko Bertmer, Juras Banyš, and Mantas Šimėnas. Nmr and raman scattering studies of temperature-and pressure-driven phase transitions in ch3nh2nh2pbcl3 perovskite. *J. Phys. Chem. C*, 124(49):26999–27008, 2020.
- [38] Mirosław Maçzka, Jan A Zienkiewicz, and Maciej Ptak. Comparative studies of phonon properties of three-dimensional hybrid organic-inorganic perovskites comprising methylhydrazinium, methylammonium, and formamidinium cations. *J. Phys. Chem. C*, 126(8):4048–4056, 2022.
- [39] Dawid Drozdowski, Anna Gağor, Dagmara Stefańska, Jan K Zaręba, Katarzyna Fedoruk, Mirosław Maçzka, and Adam Sieradzki. Three-dimensional methylhydrazinium lead halide perovskites: Structural changes and effects on dielectric, linear, and nonlinear optical properties entailed by the halide tuning. *J. Phys. Chem. C*, 126(3):1600–1610, 2022.
- [40] Stefan Grimme. Semiempirical gga-type density functional constructed with a long-range dispersion correction. *J. Comput. Chem.*, 27(15):1787–1799, 2006.
- [41] Vincenzo Barone, Maurizio Casarin, Daniel Forrer, Michele Pavone, Mauro Sambi, and Andrea Vittadini. Role and effective treatment of dispersive forces in materials: Polyethylene and graphite crystals as test cases. *J. Comput. Chem.*, 30(6):934–939, 2009.
- [42] Xudong Zhang, Wenyi Huang, Jiaying Chen, Cong Liu, Hui Yu, Lijun Zhao, and Wei Jiang. Phase stability, elastic, anisotropic and thermodynamic properties

- of gdt2al20 ($t = \text{ti, v, cr}$) compounds: A first-principles study. *Vacuum*, 157(0):312–319, 2018.
- [43] E Lora Da Silva, Jonathan M Skelton, Stephen C Parker, and Aron Walsh. Phase stability and transformations in the halide perovskite cssni_3 . *Phys. Rev. B*, 91(14):144107, 2015.
- [44] John P Perdew, Adrienn Ruzsinszky, Gábor I Csonka, Oleg A Vydrov, Gustavo E Scuseria, Lucian A Constantin, Xiaolan Zhou, and Kieron Burke. Restoring the density-gradient expansion for exchange in solids and surfaces. *Phys. Rev. Lett.*, 100(13):136406, 2008.
- [45] Noemi Hernandez-Haro, Joaquín Ortega-Castro, Yaroslav B Martynov, Rashid G Nazmitdinov, and Antonio Frontera. Dft prediction of band gap in organic-inorganic metal halide perovskites: An exchange-correlation functional benchmark study. *Chem. Phys.*, 516(0):225–231, 2019.
- [46] Un-Gi Jong, Chol-Jun Yu, Yun-Hyok Kye, Yong-Guk Choe, Wei Hao, and Shuzhou Li. First-principles study on structural, electronic, and optical properties of inorganic ge-based halide perovskites. *Inorg. Chem.*, 58(7):4134–4140, 2019.
- [47] Ivano E Castelli, Juan María García-Lastra, Kristian S Thygesen, and Karsten W Jacobsen. Bandgap calculations and trends of organometal halide perovskites. *APL Mater.*, 2(8):081514, 2014.
- [48] Ridwan O Agbaoye, Gboyega A Adebayo, and Stephane Kenmoe. Band structure and absorption spectra of nh_4xi_3 ($x = \text{pb, mg}$) based hybrid perovskite for uv ray protector and electrochromic materials applications. *J. Phys. Chem. Solids*, 151:109860, 2021.
- [49] Zhen Fan, Kuan Sun, and John Wang. Perovskites for photovoltaics: A combined review of organic-inorganic halide perovskites and ferroelectric oxide perovskites. *J. Mater. Chem. A*, 3(37):18809–18828, 2015.
- [50] Jingrui Li and Patrick Rinke. Atomic structure of metal-halide perovskites from first principles: The chicken-and-egg paradox of the organic-inorganic interaction. *Phys. Rev. B*, 94(4):045201, 2016.
- [51] Bumseop Kim, Jeongwoo Kim, and Noejung Park. First-principles identification of the charge-shifting mechanism and ferroelectricity in hybrid halide perovskites. *Sci. Rep.*, 10(1):1–7, 2020.
- [52] Nicola A Spaldin. A beginner’s guide to the modern theory of polarization. *J. Solid State Chem.*, 195(0):2–10, 2012.
- [53] Alessandro Stroppa, Claudio Quarti, Filippo De Angelis, and Silvia Picozzi. Ferroelectric polarization of $\text{ch}_3\text{nh}_3\text{pb}_3\text{i}_3$: A detailed study based on density functional theory and symmetry mode analysis. *J. Phys. Chem. Lett.*, 6(12):2223–2231, 2015.
- [54] Tran Doan Huan, Vu Ngoc Tuoc, and Nguyen Viet Minh. Layered structures of organic/inorganic hybrid halide perovskites. *Phys. Rev. B*, 93(9):094105, 2016.
- [55] Arthur Marronnier, Heejae Lee, Bernard Geffroy, Jacky Even, Yvan Bonnassieux, and Guido Roma. Structural instabilities related to highly anharmonic phonons in halide perovskites. *J. Phys. Chem. Lett.*, 8(12):2659–2665, 2017.
- [56] Omer Yaffe, Yinsheng Guo, Liang Z Tan, David A Egger, Trevor Hull, Constantinos C Stoumpos, Fan Zheng, Tony F Heinz, Leeor Kronik, Mercouri G Kanatzidis, et al. Local polar fluctuations in lead halide perovskite crystals. *Phys. Rev. Lett.*, 118(13):136001, 2017.
- [57] Chao Wang, Ming Zhang, Ruzhi Wang, Chi Zhang, Xianrui Meng, Yupeng Xi, Sainan Li, and Hui Yan. First-principles investigation into hybrid improper ferroelectricity in ruddlesden–popper perovskite chalcogenides $\text{sr}_3\text{b}_2\text{x}_7$ ($\text{b} = \text{ti, zr, hf}$; $\text{x} = \text{s, se}$). *J. Phys. Chem. C*, 125(25):13971–13983, 2021.
- [58] Linn Leppert, Sebastian E Reyes-Lillo, and Jeffrey B Neaton. Electric field-and strain-induced rashba effect in hybrid halide perovskites. *J. Phys. Chem. Lett.*, 7(18):3683–3689, 2016.
- [59] Jinsong Huang, Yongbo Yuan, Yuchuan Shao, and Yanfa Yan. Understanding the physical properties of hybrid perovskites for photovoltaic applications. *Nat. Rev. Mater.*, 2(7):1–19, 2017.
- [60] Shamim Shahrokhi, Wenxiu Gao, Yutao Wang, Pradeep Raja Anandan, Md Zahidur Rahaman, Simrjit Singh, Danyang Wang, Claudio Cazorla, Guoliang Yuan, Jun-Ming Liu, et al. Emergence of ferroelectricity in halide perovskites. *Small Methods*, 4(8):2000149, 2020.
- [61] RD King-Smith and David Vanderbilt. Theory of polarization of crystalline solids. *Phys. Rev. B*, 47(3):1651, 1993.
- [62] Raffaele Resta. Modern theory of polarization in ferroelectrics. *Ferroelectrics*, 151(1):49–58, 1994.
- [63] Raffaele Resta and David Vanderbilt. Theory of polarization: A modern approach. In *Physics of Ferroelectrics*, pages 31–68. Springer, 2007.
- [64] Nicola Marzari and David Vanderbilt. Maximally localized generalized wannier functions for composite energy bands. *Phys. Rev. B*, 56(20):12847, 1997.
- [65] Giovanni Pizzi, Valerio Vitale, Ryotaro Arita, Stefan Blügel, Frank Freimuth, Guillaume Géranton, Marco Gibertini, Dominik Gresch, Charles Johnson, Takashi Koretsune, et al. Wannier90 as a community code: New features and applications. *J. Phys.: Condens. Matter*, 32(16):165902, 2020.
- [66] Arash A Mostofi, Jonathan R Yates, Giovanni Pizzi, Young-Su Lee, Ivo Souza, David Vanderbilt, and Nicola Marzari. An updated version of wannier90: A tool for obtaining maximally-localised wannier functions. *Comput. Phys. Commun.*, 185(8):2309–2310, 2014.
- [67] Douglas H Fabini, Ram Seshadri, and Mercouri G Kanatzidis. The underappreciated lone pair in halide perovskites underpins their unusual properties. *MRS Bull.*, 45(6):467–477, 2020.
- [68] Ali Mehdizadeh, Seyed Farshad Akhtarianfar, and Saeid Shojaei. Role of methylammonium rotation in hybrid halide mapbx_3 ($x = \text{i, br, and cl}$) perovskites by a density functional theory approach: Optical and electronic properties. *J. Phys. Chem. C*, 123(11):6725–6734, 2019.
- [69] Eti Mahal, Shyama Charan Mandal, Diptendu Roy, and Biswarup Pathak. Energy level alignments between organic and inorganic layers in 2d layered perovskites: conjugation vs. substituent. *Nanoscale*, 15(17):7962–7970, 2023.
- [70] Xiaoyan Gan et al. Role of organic cations in tuning the exciton binding energy of 2d lead iodide perovskite derivatives. *J. Lumin.*, 260(0022):119878, 2023.
- [71] George C Fish, Aaron T Terpstra, Algirdas Dučinskas, Masaud Almalki, Loïc C Carbone, Lukas Pfeifer, Michael Grätzel, Jacques-E Moser, and Jovana V Milić. The impact of spacer size on charge transfer excitons in dion–jacobson and ruddlesden–popper layered hybrid perovskites. *J. Phys. Chem. Lett.*, 14(0):6248–6254, 2023.

- [72] Marina R Filip, Diana Y Qiu, Mauro Del Ben, and Jeffrey B Neaton. Screening of excitons by organic cations in quasi-two-dimensional organic–inorganic lead-halide perovskites. *Nano Lett.*, 22(12):4870–4878, 2022.
- [73] Shelby A Cuthriell, Christos D Malliakas, Mercouri G Kanatzidis, and Richard D Schaller. Cyclic versus linear alkylammonium cations: Preventing phase transitions at operational temperatures in 2d perovskites. *J. Am. Chem. Soc.*, 145(21):11710–11716, 2023.
- [74] Andrew M Rappe, Karin M Rabe, Efthimios Kaxiras, and JD Joannopoulos. Erratum: Optimized pseudopotentials [phys. rev. b 41, 1227 (1990)]. *Physical Review B*, 44(23):13175, 1991.
- [75] John P Perdew, Kieron Burke, and Matthias Ernzerhof. Generalized gradient approximation made simple. *Phys. Rev. Lett.*, 77(18):3865, 1996.
- [76] Paolo Giannozzi, Stefano Baroni, Nicola Bonini, Matteo Calandra, Roberto Car, Carlo Cavazzoni, Davide Ceresoli, Guido L Chiarotti, Matteo Cococcioni, Ismaila Dabo, et al. Quantum espresso: A modular and open-source software project for quantum simulations of materials. *J. Phys.: Condens. Matter*, 21(39):395502, 2009.
- [77] Paolo Giannozzi, Oliviero Andreussi, Thomas Brumme, Oana Bunau, M Buongiorno Nardelli, Matteo Calandra, Roberto Car, Carlo Cavazzoni, Davide Ceresoli, Matteo Cococcioni, et al. Advanced capabilities for materials modelling with quantum espresso. *J. Phys.: Condens. Matter*, 29(46):465901, 2017.
- [78] Ivo Souza, Nicola Marzari, and David Vanderbilt. Maximally localized wannier functions for entangled energy bands. *Phys. Rev. B*, 65(3):035109, 2001.
- [79] John P Perdew, Matthias Ernzerhof, and Kieron Burke. Rationale for mixing exact exchange with density functional approximations. *J. Chem. Phys.*, 105(22):9982–9985, 1996.
- [80] Jing Yang, Liang Z Tan, and Andrew M Rappe. Hybrid functional pseudopotentials. *Phys. Rev. B*, 97(8):085130, 2018.
- [81] Georg Kresse and Jürgen Hafner. Ab initio molecular dynamics for liquid metals. *Phys. Rev. B*, 47(1):558, 1993.
- [82] Georg Kresse and Jürgen Furthmüller. Efficiency of ab-initio total energy calculations for metals and semiconductors using a plane-wave basis set. *Comput. Mater. Sci.*, 6(1):15–50, 1996.
- [83] Georg Kresse and Jürgen Furthmüller. Efficient iterative schemes for ab initio total-energy calculations using a plane-wave basis set. *Phys. Rev. B*, 54(16):11169, 1996.
- [84] G Kresse and J Hafner. Norm-conserving and ultrasoft pseudopotentials for first-row and transition elements. *J. Phys.: Condens. Matter*, 6(40):8245, 1994.
- [85] A Togo and I Tanaka. First principles phonon calculations in materials science. *Scr. Mater.*, 108(0):1–5, Nov 2015.
- [86] M. J. Frisch, G. W. Trucks, H. B. Schlegel, G. E. Scuseria, M. A. Robb, J. R. Cheeseman, G. Scalmani, V. Barone, G. A. Petersson, H. Nakatsuji, X. Li, M. Caricato, A. V. Marenich, J. Bloino, B. G. Janesko, R. Gomperts, B. Mennucci, H. P. Hratchian, J. V. Ortiz, A. F. Izmaylov, J. L. Sonnenberg, D. Williams-Young, F. Ding, F. Lipparini, F. Egidi, J. Goings, B. Peng, A. Petrone, T. Henderson, D. Ranasinghe, V. G. Zakrzewski, J. Gao, N. Rega, G. Zheng, W. Liang, M. Hada, M. Ehara, K. Toyota, R. Fukuda, J. Hasegawa, M. Ishida, T. Nakajima, Y. Honda, O. Kitao, H. Nakai, T. Vreven, K. Throssell, J. A. Montgomery, Jr., J. E. Peralta, F. Ogliaro, M. J. Bearpark, J. J. Heyd, E. N. Brothers, K. N. Kudin, V. N. Staroverov, T. A. Keith, R. Kobayashi, J. Normand, K. Raghavachari, A. P. Rendell, J. C. Burant, S. S. Iyengar, J. Tomasi, M. Cossi, J. M. Millam, M. Klene, C. Adamo, R. Cammi, J. W. Ochterski, R. L. Martin, K. Morokuma, O. Farkas, J. B. Foresman, and D. J. Fox. Gaussian 16 Revision C.01, 2016. Gaussian Inc. Wallingford CT.
- [87] Axel D Becke. Density-functional thermochemistry. iv. a new dynamical correlation functional and implications for exact-exchange mixing. *J. Chem. Phys.*, 104(3):1040–1046, 1996.
- [88] Chengteh Lee, Weitao Yang, and Robert G Parr. Development of the colle-salvetti correlation-energy formula into a functional of the electron density. *Phys. Rev. B*, 37(2):785, 1988.
- [89] AD McLean and GS Chandler. Contracted gaussian basis sets for molecular calculations. i. second row atoms, $z=11-18$. *J. Chem. Phys.*, 72(10):5639–5648, 1980.
- [90] RBJS Krishnan, J Stephen Binkley, Rolf Seeger, and John A Pople. Self-consistent molecular orbital methods. xx. a basis set for correlated wave functions. *J. Chem. Phys.*, 72(1):650–654, 1980.
- [91] Aneta Ciupa-Litwa, Maciej Ptak, Edyta Kucharska, Jerzy Hanuza, and Mirosław Mączka. Vibrational properties and dft calculations of perovskite-type methylhydrazinium manganese hypophosphate. *Molecules*, 25(21):5215, 2020.

Supplemental Material: Guest-induced phase transition leads to polarization enhancement in MHyPbCl₃

Pradhi Srivastava¹, Sayan Maity², Varadharajan Srinivasan²

¹Department of Physics, Indian Institute of Science Education and Research Bhopal, Bhopal 462 066, India and

²Department of Chemistry, Indian Institute of Science Education and Research Bhopal, Bhopal 462 066, India

S-I. INTRODUCTION

TABLE S1. Cubic (disordered) phase transition temperatures with respect to 0 K ordered phase, for chloride perovskites with different tolerance factors.

| Parameters | MAPbCl ₃ | FAPbCl ₃ | MHyPbCl ₃ |
|--------------------------|---------------------|---------------------|---|
| τ [1–3] | 0.94 | 1.02 | 1.14 |
| Temperature (K) | 178 [4–8] | 200 [9, 10] | 342 [11] |
| Host barrier (meV/f.u.) | 302 ^a | 492 ^a | 44 ^{a,b} 604 ^{a,c} |
| Guest barrier (meV/f.u.) | 135 [12] | 104 [13] | 75 ^b 237 ^c |

^a Calculated in our work.

^b Comparison between the two ordered phases, cubic phase does not exist.

^c Theoretically constructed cubic phase.

TABLE S2. Cubic (disordered) phase transition temperatures with respect to 0 K ordered phase, for bromide perovskites with different tolerance factors.

| Parameters | MAPbBr ₃ | FAPbBr ₃ | MHyPbBr ₃ |
|--------------------------|---------------------|-----------------------|----------------------|
| τ [1–3] | 0.92 | 1.00 | 1.10 |
| Temperature (K) | 236 [14] | 260 [14–16] | 420 |
| Host barrier (meV/f.u.) | 215 [17] | 448 ^a [18] | 542 ^a |
| Guest barrier (meV/f.u.) | 25 [17] | 95 [18] | 159 ^a |

^a Calculated in our work

TABLE S3. Cubic (disordered) phase transition temperatures with respect to 0 K ordered phase, for iodide perovskites with different tolerance factors.

| Parameters | NH ₄ PbI ₃ [19] | MAPbI ₃ | FAPbI ₃ |
|--------------------------|---------------------------------------|--------------------|--------------------|
| τ [1–3] | 0.76 | 0.91 | 0.98 |
| Temperature (K) | – | 327 [5, 20] | 400 |
| Host barrier (meV/f.u.) | 500 | 160 [21, 22] | 260 [23] |
| Guest barrier (meV/f.u.) | 25 | 32 [12, 24] | 83 [25] |

Tables S1–S3 compare the *host* and the *guest* barrier for differently sized *guests*/A-site cations. The *host* barrier is the difference in the single point energies of the 0 K optimized phase (distorted *host*) and the disordered cubic phase (undistorted *host*) unless specified otherwise. The *guest* barrier is the reorientational energy barrier of the organic cation in the disordered phase between energy-equivalent configurations. The analysis suggests that as the tolerance factor increases (due to an increase in the size of the *guest*), the phase transition temperature rises, along with a relative increase in the *guest* barrier over the *host*.

S-II. STRUCTURAL DETAILS

To compare the alignment of MHy⁺-ions in MHyPbCl₃ of Phases-I and II according to the experimentally suggested polarization direction [11], the structure of Phase-II is transformed as shown in (Fig. S1). This transformation (S.1) corresponds to the screw symmetry (2₁) about *c*-axis.

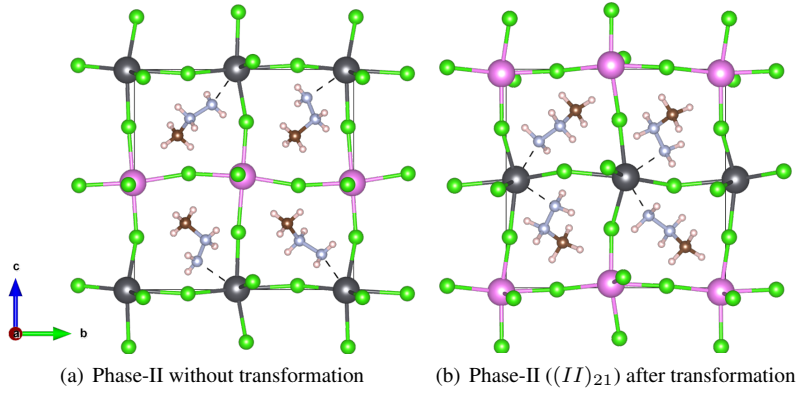


FIG. S1. Phase-II being transformed as per the transformation mentioned in the matrix. This is done to bring one-to-one correspondence between the *guest* ions of Phase-I and Phase-II.

TABLE S4. Comparison of the experimentally and theoretically calculated lattice parameters for PBE and PBEsol functionals (+vdW-corr.) as implemented in QE. Self-consistent energy difference, ΔE , with respect to Phase-I is also reported.

| Lattice-parameters | Expt. ^a | | PBE | | PBEsol | |
|------------------------------------|--------------------|---------|-------------------------------|--------------------|-------------------|-------------------|
| | LT | HT | LT | HT | LT | HT |
| a (Å) | 5.7266 | 5.7416 | 5.7034 (0.40) ^b | 5.6520 (1.56) | 5.5204 (3.60) | 5.5182 (3.89) |
| b (Å) | 11.3396 | 11.4227 | 11.2966 (0.38) | 11.4523 (-0.26) | 10.9719 (3.24) | 11.1290 (2.57) |
| c (Å) | 11.3926 | 11.4054 | 11.2680 (1.09) | 11.1585 (2.16) | 10.9787 (3.63) | 10.8333 (5.02) |
| β (°) | 87.6680 | 90 | 87.7091 (-0.05) | 90 | 83.3983 (4.87) | 90 |
| ΔE (meV/f.u.) ^c | | | -39.55 | 0 | -44.22 | 0 |

^a The parameters are taken from [11].

^b The numbers in braces are the tolerance values, τ which is defined in Sec.S-II.

^c Phase I has been taken as the reference while evaluating ΔE .

$$\begin{bmatrix} a_{tr} \\ b_{tr} \\ c_{tr} \end{bmatrix} = \begin{bmatrix} -1 & 0 & 0 \\ 0 & -1 & 0 \\ 0 & 0 & 1 \end{bmatrix} \begin{bmatrix} a \\ b \\ c \end{bmatrix} + \begin{bmatrix} 0 \\ 0 \\ 0.5 \end{bmatrix} \quad (\text{S.1})$$

The lattice parameters of Phase-I ((I)₁₁) and Phase-II ((II)₂₁) as obtained from Quantum ESPRESSO (Table S4), and VASP (Table S5) have been compared with respect to the experimental values [11] for different functionals [26–28] (PBE [29], PBEsol [30] and hybrid-PBE0 functionals [31, 32]).

$$\tau(\%) = (a_{exp} - a_{opt})/a_{exp} \times 100 \quad (\text{S.2})$$

Energetically, ((II)₂₁) is the ground state for all the cases considered.

The *host* distortion is measured as the root mean square (RMS) of the deviation of the bond from the average over bond lengths. It is defined as follows:

$$\delta d_{\text{Pb-Cl}} = \sqrt{\frac{1}{6} \sum_{j=1}^6 (d_{\text{Pb-Cl},j} - d_{\text{Pb-Cl}})^2} \quad (\text{S.3})$$

Here, $\delta d_{\text{Pb-Cl}}$ is the RMS of the deviation of the bond length, and is a measure of *host* distortion.

$$d_{\text{Pb-Cl}} = \frac{1}{6} \sum_{j=1}^6 d_{\text{Pb-Cl},j} \quad (\text{S.4})$$

TABLE S5. Comparison of the experimental and theoretically obtained lattice parameters for different functionals as implemented in VASP. Self-consistent total energy difference, ΔE , is measured for optimized structures with respect to Phase-I. The maximum component of force is less than the convergence threshold criterion of $5E-3 \text{ eV/\AA}$

| Lattice-parameters | Expt. | | PBE | | PBEsol | | Hybrid-PBE0 | |
|-----------------------|----------|----------|----------|----------|----------|----------|-------------|----------|
| | LT | HT | LT | HT | LT | HT | LT | HT |
| a (Å) | 5.7266 | 5.7416 | 5.7031 | 5.6555 | 5.5197 | 5.5201 | 5.6498 | 5.6118 |
| b (Å) | 11.3396 | 11.4227 | 11.2835 | 11.4296 | 10.9682 | 11.1254 | 11.2022 | 11.3466 |
| c (Å) | 11.3926 | 11.4054 | 11.2667 | 11.1828 | 10.9801 | 10.8587 | 11.1932 | 11.1035 |
| α (°) | 90 | 90 | 90 | 90 | 90 | 90 | 90 | 90 |
| β (°) | 87.67 | 90 | 87.77 | 90 | 83.49 | 90 | 87.13 | 90 |
| γ (°) | 90 | 90 | 90 | 90 | 90 | 90 | 90 | 90 |
| V (Å ³) | 739.1926 | 748.0183 | 724.4635 | 722.8475 | 660.4912 | 666.8702 | 707.5309 | 707.0062 |
| ΔE (meV) | | | -151 | 0 | -164 | 0 | -106 | 0 |
| F_{max} (eV/(Å)) | | | 7.50E-04 | 1.50E-03 | 2.50E-03 | 3.20E-03 | 7.6E-04 | 7.5E-04 |

where j runs over the six chlorine atoms of the lead octahedra. $d_{\text{Pb}-\text{Cl}}$ is the average bond length. The *host* distortion as per this definition is plotted in Fig. 2(a).

The *host* tilting, defined by $\delta\theta_{\text{tilt}}$, is a measure of its deviation from 90° (for an ideal cubic phase). $\delta\theta_{gl}$ gives the deviation of the octahedral tilt from 0° of the cubic phase (in which case there is a zero-tilt). The definitions of these two parameters with respect to *host* are as follows:

$$|\delta\theta_{\text{tilt}}| = (|\delta\theta_{\text{tilt}1}| + |\delta\theta_{\text{tilt}2}|)/2 \quad (\text{S.5a})$$

$$\delta\theta_{\text{tilt}1} = 90 - \theta_{\text{avg}1} \quad (\text{S.5b})$$

$$\theta_{\text{avg}1} = (\theta_{m1} + \theta_{n1})/2 \quad (\text{S.5c})$$

where θ_{m1} and θ_{n1} has been shown in (iii) of Fig. 2 of main text. Here, the tilt angle is calculated with respect to the ideal cubic phase tilting. These values in the plane perpendicular to all the axes have been reported in Table S7. The other set of tilt angle is given by $\theta_{\text{avg}2} = (\theta_{m2} + \theta_{n2})/2$, hence $\delta\theta_{\text{tilt}2} = 90 - \theta_{\text{avg}2}$. Similar deviations in the tilt angles can be shown along b and c -axes as well. A complete plot corresponding to $\delta\theta_{\text{tilt}}$ is shown in Fig. 2(b) The deviations indicate how close the *host* tilting is to a particular phase, Phase-I or II. An alternate way to quantify the tilts is by estimating the Glazer notation along a , b , and c -axes, respectively. The deviation in the octahedral tilts from the perfect cubic octahedron perpendicular to a -axis, $\delta\theta_{gl}$, is given by

$$\delta\theta_{gl} = (|b_1| + |b_2| + |c_1| + |c_2|)/4 \quad (\text{S.6})$$

Refer to (iv) of Fig. 2 in the main text for the angles b_1 , b_2 , c_1 , and c_2 . The shifts in Glazer angles (with respect to cubic phase) along a , b , and c -axis for differently distorted octahedral layers, layer-I (less distorted) and layer-II (more distorted), have been plotted in Fig. 2(c). The angle, $\delta\theta_{gl}$, is averaged over the plane perpendicular to a -axis. The tilts about b and c -axes can be obtained similarly. Fig. 2(d) shows the variation in $\delta\theta_{gl}$ averaged over layers as well as over the plane.

Similarly, we define a set of parameters to define the *guest* configuration. The *guest* reorientation pattern of the i^{th} structure is described by the orientation of the normal to the molecular plane, (θ_n, ϕ_n) and a set of internal angles, ω_{int} . The internal angles are obtained by aligning the normal along the crystal c -axis, such that the molecule lies in the ab plane. $\omega_{1_{\text{int}}/2_{\text{int}}}$ is the angle made by CN1/N2N1 bond measured to the crystal a -axis. The schematic of the angles to define the molecular orientation has been shown in (i) and (ii) of Fig. 2 of the main text. The values of *host* tilting and *guest* orientation for Phase-I, ($\sim II$)₂₁ and (II)₂₁ and several other structures have been tabulated in Tables S7 and S10.

S-III. HOST-GUEST (HG) COUPLING

A. HG coupling strength

The strength depends on the *guest* type/orientation for a given *host* [33]. Herein, we propose a measure for the *host/guest* coupling strength in a given phase or, equivalently, a given *guest* orientation. For this, we first define the elastic energy cost that

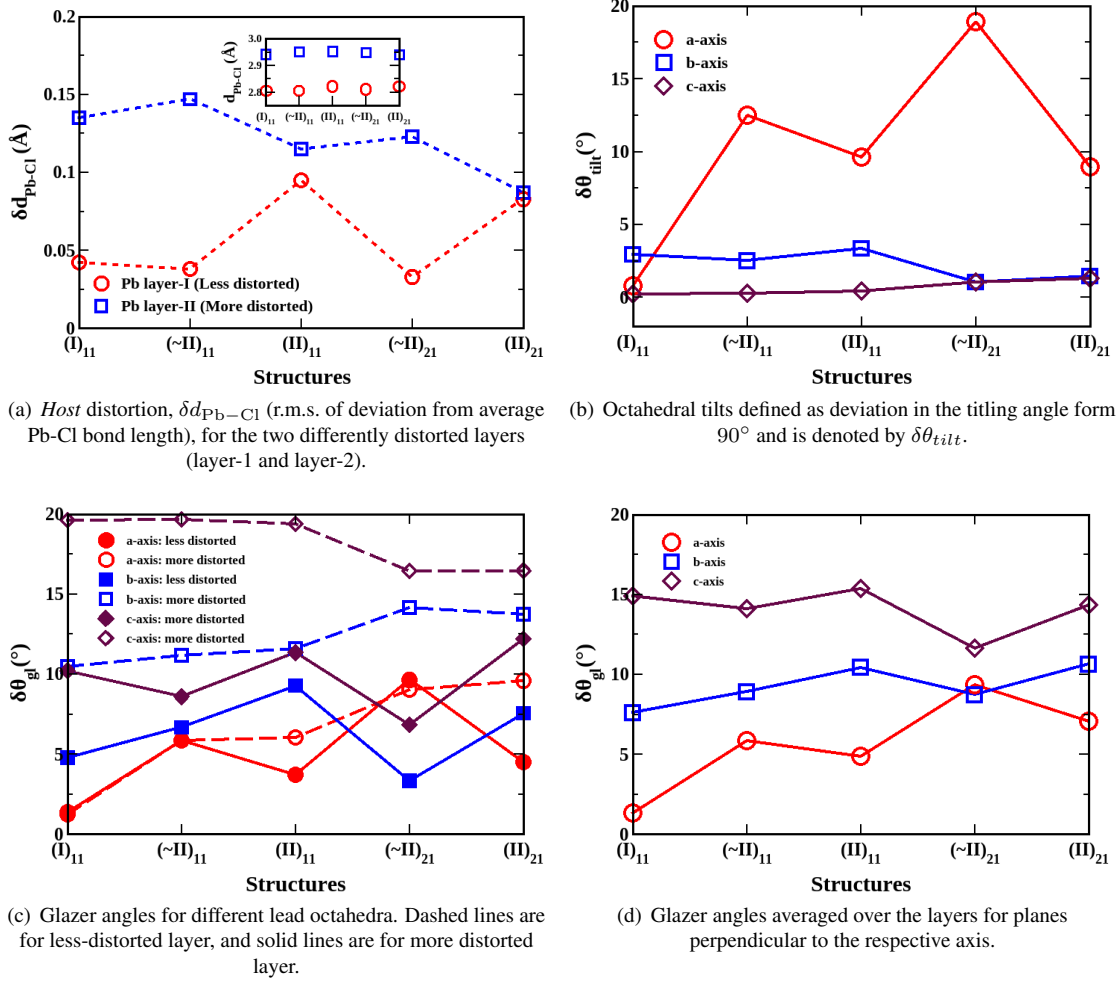


FIG. S2. Parameters to define the (a) *host* distortion (given by δd_{Pb-Cl}), and (b) deviation in octahedral titling from the ideal 90° of ideal cubic phase (given by $\delta\theta_{tit}$), (c) Glazer angles for differently distorted layers (given by $\delta\theta_{gl}$) and (d) Averaged Glazer angles over all the layers. These analyses are carried over different structures, including $(I)_{11}$, $(\sim II)_{11}$, $(II)_{11}$, $(\sim II)_{21}$, and $(II)_{21}$.

TABLE S6. Comparison of experimentally and theoretically obtained lattice parameters (in terms of percentage difference, τ) for PBE, PBEsol and PBE0 functionals as implemented in VASP. Self-consistent energy difference for the optimized phases, ΔE , with respect to Phase-I is also reported.

| Lattice-parameters | PBE | | PBEsol | | Hybrid (PBE0) | |
|-------------------------------|-------|------|--------|------|---------------|------|
| | LT | HT | LT | HT | LT | HT |
| a | 0.40 | 1.50 | 3.60 | 3.90 | 1.40 | 2.40 |
| b | 0.50 | 0.00 | 3.30 | 2.60 | 1.30 | 1.00 |
| c | 1.10 | 2.00 | 3.60 | 4.80 | 1.10 | 2.00 |
| β^a | -0.10 | | 4.80 | | 0.67 | |
| ΔE (meV) ^b | -151 | 0 | -164 | 0 | -106 | 0 |

^a β is measured only for LT (Phase-II) since it is monoclinic with b as its unique axis.

^b Phase-I has been taken as the reference while evaluating ΔE .

the *host* incurs in transitioning to undistorted from a distorted phase at a given configuration of the *guest* (here, g_0 , which is the lowest symmetry or ground state configuration), which is given by the following equation.

$$E_{elas}^A = E_{undist}^A - E_{dist}^A \quad (S.7)$$

where E^A is the electronic energy for the 0K ground state for ion in ABX_3 in the a given phase. This elastic energy cost can also be interpreted from the Taylor series expansion of the energy of the undistorted phase (cubic or the completely disordered

TABLE S7. Parameters for *host* tilting (averaged Glazer notation over layers, $\delta\theta - \text{tilt}$, perpendicular to all the axes) and *guest* orientation at all the four sites for different structures as optimized from QE.

| Structures | Octahedral rotation | | | Guest-site | Normal to molecular plane | | Internal coordinates | |
|---------------------------|---------------------|-----------|-----------|------------|---------------------------|----------|----------------------|-----------------|
| | a -axis | b -axis | c -axis | | θ_n | ϕ_n | ω_{1int} | ω_{2int} |
| $(I)_{11}$ (Phase-I) | 0.81 | 2.95 | 0.22 | m | 140.82 | 81.50 | -41.87 | 37.65 |
| | | | | m' | 39.18 | 98.50 | 155.13 | -125.34 |
| | | | | n' | 39.18 | -81.50 | 155.13 | -125.34 |
| | | | | n | 140.82 | -98.50 | -41.87 | 37.65 |
| $(\sim II)_{11}$ | 12.49 | 2.51 | 0.28 | m | 130.15 | 82.68 | -41.58 | 36.57 |
| | | | | m' | 49.85 | 97.32 | 153.06 | -128.80 |
| | | | | n' | 31.63 | -76.36 | 155.49 | -123.15 |
| | | | | n | 148.37 | -103.64 | -51.78 | 29.58 |
| $(II)_{11}$ | 9.63 | 3.34 | 0.41 | m | 135.46 | 81.71 | -39.06 | 39.92 |
| | | | | m' | 44.54 | 98.29 | 157.51 | -123.51 |
| | | | | n' | 34.64 | -86.61 | 151.82 | -129.14 |
| | | | | n | 145.36 | -93.39 | -34.97 | 44.07 |
| $(\sim II)_{21}$ | 18.92 | 1.04 | 1.03 | m | 45.30 | 164.61 | 31.45 | 159.25 |
| | | | | m' | 134.70 | 15.39 | 62.22 | -169.98 |
| | | | | n' | 32.74 | -68.37 | 156.31 | -119.40 |
| | | | | n | 147.26 | -111.63 | -66.94 | 17.35 |
| $(II)_{21}$ (Phase-II) | 8.96 | 1.45 | 1.29 | m | 42.96 | 142.84 | 22.47 | 150.81 |
| | | | | m' | 137.04 | 37.16 | 96.78 | -134.88 |
| | | | | n' | 39.09 | -84.68 | 153.46 | -126.37 |
| | | | | n | 140.91 | -95.32 | -37.19 | 42.98 |

phase) about that of the equilibrium (at x_0) phase as follows:

$$E_{undist}(x, g_0) = E_{dist}(x_0, g_0) + \frac{1}{2} \frac{\partial^2 E}{\partial x^2} \Big|_{(x_0, g_0)} (x - x_0)^2 + \dots \quad (\text{S.8})$$

where x represents the *host* coordinates and g represents the *guest* coordinates, which includes orientation, composition, etc. (x_0, g_0) correspond to the *host* and the *guest* coordinates in the ground state energy-minimum structure. The first order derivative vanishes at equilibrium (that is $(\partial E/\partial x)|_{(x_0, g_0)} = 0$) in Eq. S.8, whereas the second-order derivative, $(\partial^2 E/\partial x^2)|_{(x_0, g_0)} = k$, k being the elastic constant; is representative of the elastic energy cost associated with *host* distortion.

As can be seen from Figure S3(a) and (b), this elastic energy cost for the case of hybrid perovskites involves not only the energy change due to framework distortion but also due to the change in the *host/guest* coupling induced due to the change in the *host* environment. It should be noted that this also involves any electronic feedback from the *guest* polarizing the *host* and *vice-versa*. Next, in order to estimate the *host/guest* coupling strength, we consider a case where the A-site guest interacts isotropically with the *host* and is taken as the reference. This is done so as to quantify and compare the HG interactions for a range of organic *guests*. Hence, for the reference system, we replace the organic molecule with a spherically symmetric and rigid inorganic atom, cesium (Cs), which is a well-studied A-site ion for the inorganic halide perovskites (Figure S3(c) and (d)). This choice is also motivated by the fact that this methodology can thus be extended to the entire family of halide perovskites, of which cesium forms a very important part. The total elastic energy cost for OIHPs can thus be decomposed as $E_{elas}^A = E_{elas}^{Cs} + E_{ind}^{H/G}$, where $E_{ind}^{H/G}$ is the *host/guest* coupling strength induced due to the presence of an anisotropic *guest*. In other words, the strength of the HG interaction induced due to the presence of an organic entity (G , the *guest*), $(E_{ind}^{H/G})$, can thus be defined as the difference in the elastic energies of the *host* in the presence of organic ion G and an inorganic ion (here, Cs):

$$E_{ind}^{H/G} = E_{elas}^G - E_{elas}^{Cs} \quad (\text{S.9})$$

The greater the magnitude of $E_{ind}^{H/G}$; the stronger the effect of HG coupling, which can be compared for a series of *guests*, and the results are tabulated in Table S8. The table demonstrates a strong HG-interaction for *MHy*-containing halide perovskite.

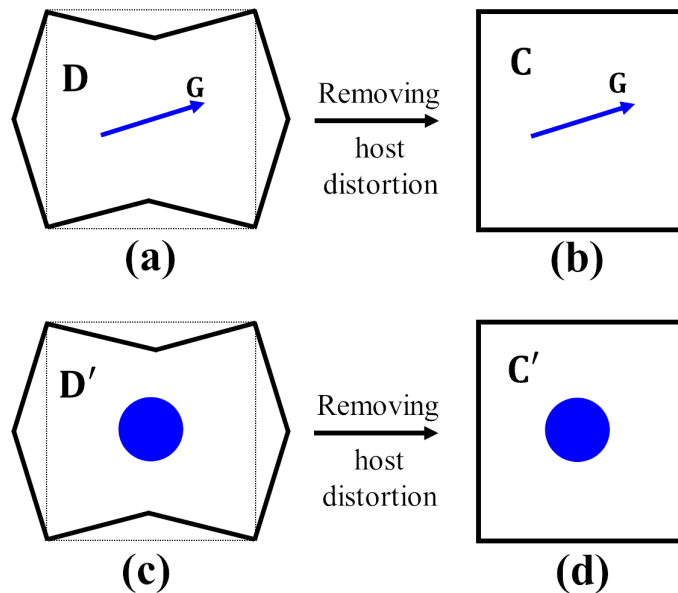


FIG. S3. Schematic of OIHPs from the perspective of *host-guest* system. The blue color indicates the positioning of the A-site ion (*guest*) facilitated by the *host* shown in black. (a) Structure D: Equilibrium/Fully optimized configuration containing the molecular dipole or the organic *guest* (*G*) in the distorted host. (b) Structure C: *Guest* of D in undistorted/cubic phase. (c) Structure D': Same as D with *G* replaced by the inorganic cation Cs^+ at the center of mass of *G*. (d) Structure C': Same as D' but with undistorted *host*. The blue isotropic spheres in structures D' and C' can also be assumed as disordered *G* which can pick up all the possible directions (*G* generally behaves as a free rotor at high temperatures).

TABLE S8. $E_{ind}^{H/G}$ for determining the *HG* coupling.

| Total energy (Ry) | Parameters of MAPbCl ₃ | | Parameters of FAPbCl ₃ | | Parameters of MHyPbCl ₃ | |
|----------------------|-----------------------------------|-----------------|-----------------------------------|-----------------|------------------------------------|-----------------|
| | MA ⁺ | Cs ⁺ | FA ⁺ | Cs ⁺ | MHy ⁺ | Cs ⁺ |
| E_{0K} | -289.747 | -304.888 | -308.708 | -304.877 | -311.009 | -304.830 |
| E_{cubic} | -289.732 | -304.895 | -308.687 | -304.880 | -310.908 | -304.874 |
| $E_{elas}^{G/Cs}$ | 0.015 | -0.006 | 0.021 | -0.003 | 0.101 | -0.044 |
| $E_{ind}^{H/G}$ | 0.021 | | 0.024 | | 0.145 | |
| $E_{ind}^{H/G}$ (eV) | 0.286 | | 0.326 | | 1.976 | |

B. Correlation between *host* distortion and *guest* orientation

Octahedral tilting and the Glazer notations for $(II)_{21}$ (which is fully optimized $(I)_{21}^c$) and $(II)_{11}$ (fully optimized $(II)_{11}$, no change in notations before and after relaxation implies that the *guest* and *host* configurations do not change significantly with respect to their starting configurations) are shown in Fig. S4 and Fig. S5. The figures show that *guest* cannot undergo reorientation even after full optimization and remains close to its starting configuration. Instead, the *host* gets distorted so as to accommodate the *guest*. Therefore, a strong correlation exists between the *guest*-reorientation and *host* distortion. Recently, a correlated effect of the *host* distortion, *guest* reorientation, and strength of H-bonding has been observed on halide ion migration [34] in $(\text{Cs}/\text{MA})\text{PbCl}_3$. This helps in estimating the halide migration barrier and reducing I-V hysteresis in solar cells [35].

We analyzed the correlation between *host* distortion and *guest* orientation by optimizing different starting configurations. The list of some of the studied structures, optimized lattice parameters, and energy differences are reported in Table S9. For greater accuracy, the rotational energy barrier is estimated by carrying out a transformation of the *guest* from Phase-I to Phase-II orientation under the constraint of Phase-I lattice parameters (Refer to Sec. S-IV). The barriers are simulated under the conditions of fixed lattice parameters of Phase-I unless specified otherwise.

The coupling between the *host* and the *guest* ordering is also verified by interchanging the $m - m'$ and $n - n'$ -positioned cations, to see the effect on *host* distortion. We observe that the distortion pattern strongly follows the cation ordering, as has been shown in Fig. S6 and Fig. S7. The figures show both the structural changes and the changes in the octahedral pattern with the interchange of the symmetry-equivalent *guest* ions.

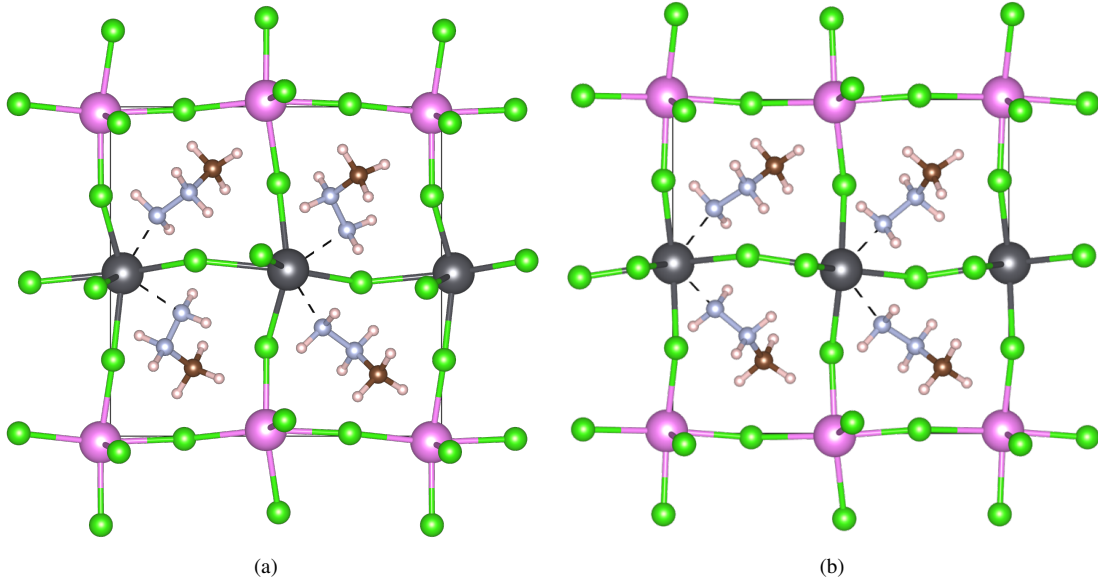


FIG. S4. Correlation of the *host* distortion and *guest* reorientation. The *guest* and the *host* of Phase-I and Phase-II are interchanged and then optimized: (a) $(II)_{21}$, obtained by optimizing $(I)_{21}$, and (b) $(II)_{11}$ (lesser distortion to accommodate Phase-I *guest*), obtained by optimizing $(II)_{11}$.

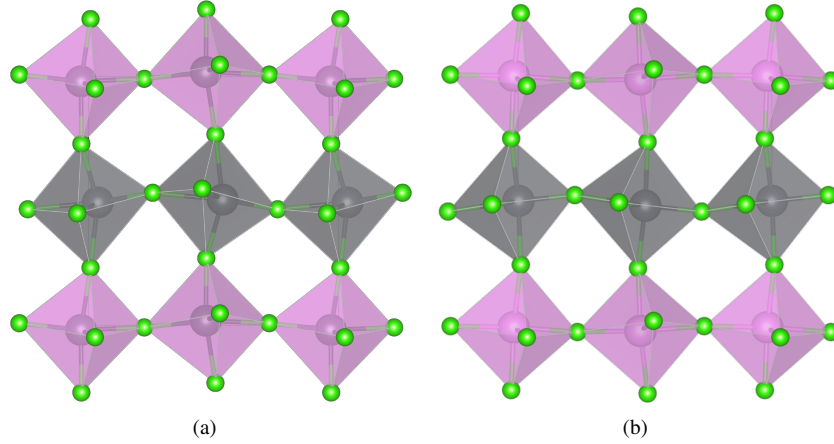


FIG. S5. Correlation of octahedral distortion and MHy^+ reorientation. (a) Octahedral distortion of $(II)_{21}$, (b) Octahedral distortion of $(II)_{11}$, respectively. Glazer notation for both the structures is $(a^+b^-c^-)$.

TABLE S9. Lattice parameters and energy differences for different structures keeping Phase-I as the reference.

| Lattice-parameters | $(I)_{21}-cc^a$ | $(II)_{11}-cc$ | $(I)_{21}-vcr^b$ | $(II)_{11}-vcr$ | $-(\sim II)_{11}-vcr^c$ | $+(\sim II)_{11}-vcr$ |
|-----------------------|-----------------|----------------|------------------|-----------------|-------------------------|-----------------------|
| a (Å) | 5.5182 | 5.5203 | 5.5207 | 5.5683 | 5.5684 | 5.5685 |
| b (Å) | 11.1290 | 10.9719 | 10.9720 | 11.1319 | 11.1236 | 11.1324 |
| c (Å) | 10.8333 | 10.9787 | 10.9779 | 10.9825 | 10.9818 | 10.9819 |
| α (°) | 90 | 90 | 90 | 90 | 90 | 90 |
| β (°) | 90 | 83.40 | 90 | 91.35 | 91.42 | 88.59 |
| γ (°) | 90 | 90 | 90 | 90 | 90 | 90 |
| V (Å ³) | 665.2951 | 660.5595 | 660.5694 | 680.5747 | 680.5760 | 680.5781 |
| ΔE (meV) | 420.69 | 317.23 | -175.79 | -53.58 | -58.40 | -58.38 |

^a cc-Host atoms are fixed in Phase-I position while *guest* atoms in Phase-II positions are allowed to relax.

^b cell optimization of Phase-I *host* with Phase-II positioned *guest*

^c cell optimization of Phase-I after following the unstable mode along both the directions

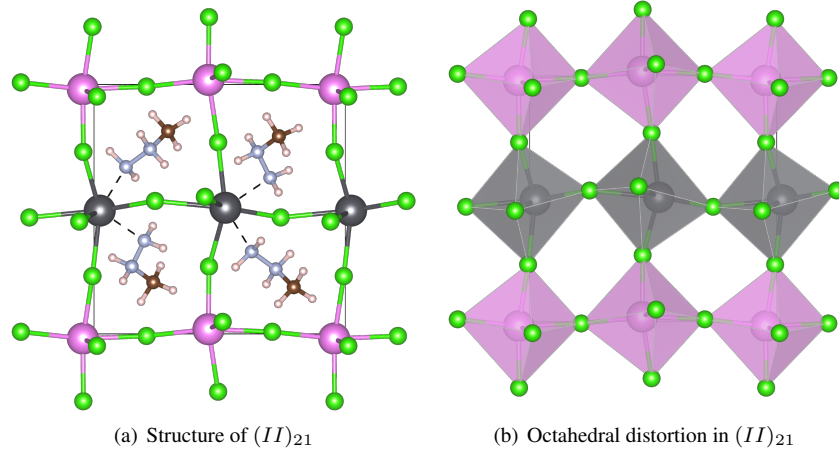


FIG. S6. *Host* distortion following the *guest* orientation in $(II)_{21}$, where the *guest* is significantly reoriented at $m - m'$ with respect to Phase-I.

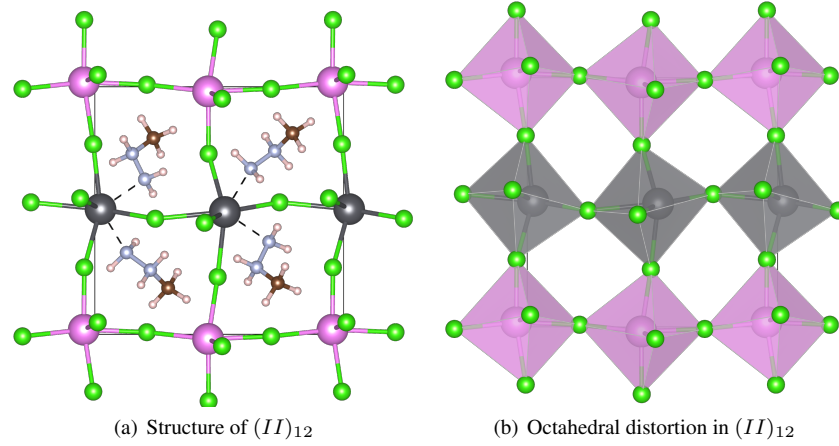


FIG. S7. Shift in the *host* distortion (with respect to Fig. S6) following the *guest* orientation in $(II)_{12}$, where the *guest* is significantly reoriented at $n - n'$ with respect to Phase-I.

S-IV. STRUCTURAL TRANSFORMATION FROM $(I)_{11}$ TO $(\sim II)_{21}$

A. Guest reorientation

We propose that the *guest* ions at $m - m'$ can be reoriented from Phase-I to Phase-II-like orientation through a rigid rotation accompanied by a translation of the form $M_{Final} = MR + T$ (Eq. S.11 and Eq. S.12), which would avoid any changes due to internal angles. Here the superscript c stands for the constraint under which this structure is created. $(I)_{21}^c$ has the constraint that the *host* and the *guest* at $n - n'$ are exactly of Phase-I, whereas the *guest* at $m - m'$ resembles $(\sim II)_{21}$ orientation. The *guest* at $n - n'$ is relaxed in $(I)_{21}$. This, further followed by the *host* relaxation, would lead to the final Phase-II-like structure, $(\sim II)_{21}$ (since it is constrained under lattice parameters of Phase-I). This transition is similar to the roto-displacive type distortion connecting the AFE and FE structures of $APbI_3$ ($A=MA, FA$) [36, 37]. M in the above equation represents the coordinates of the atoms of MHy^+ of $(I)_{11}$ and M_{Final} for $(I)_{21}^c$.

The transformation matrix is evaluated as follows:

$$R = R_z(\phi)R_x(\theta)R_z''(\psi) \quad (S.10)$$

$$T' = \begin{bmatrix} (N1_x)_{(I)_{11}} + \sin(j) \left((N1_x)_{(\sim II)_{21}} - (N1_x)_{(I)_{11}} \right) \\ (N1_y)_{(I)_{11}} + \sin(j) \left((N1_y)_{(\sim II)_{21}} - (N1_y)_{(I)_{11}} \right) \\ (N1_z)_{(I)_{11}} + \sin(j) \left((N1_z)_{(\sim II)_{21}} - (N1_z)_{(I)_{11}} \right) \end{bmatrix} \quad (S.11)$$

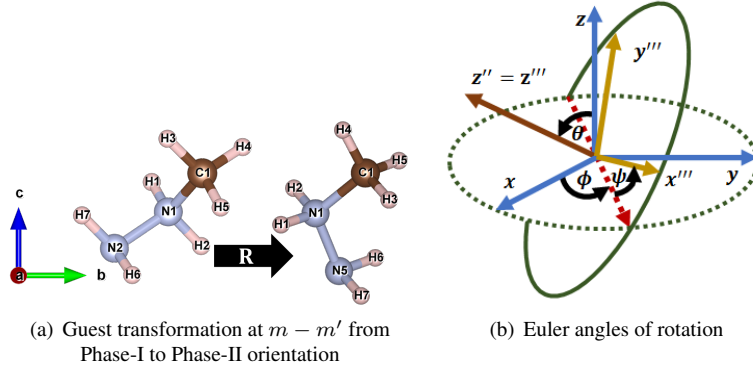


FIG. S8. Transformation of the *guest* from Phase-I orientation to Phase-II-orientation using a matrix of transformation shown by \mathbf{R} , which includes both the Euler angles of rotation and translation vector.

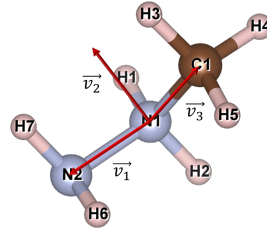


FIG. S9. Vectors used while transformation are denoted by \vec{v}_1 , \vec{v}_2 , and \vec{v}_3 . \vec{v}_1 denotes the $N1N2$ unit vector, \vec{v}_3 denotes the unit vector corresponding to $C1N1$. These two are defined in the molecular plane. The third vector, \vec{v}_2 , defines the unit vector normal to the molecular plane and is obtained by the cross product of \vec{v}_1 and \vec{v}_3 .

Here the angles, ϕ , θ and ψ are the Euler angles of rotation about z , x and z'' -axes respectively. $j = 0^\circ$ and 90° for $(I)_{11}$ and $(I)_{21}^c$, respectively.

$$0 \leq \theta \leq 180^\circ : \begin{cases} \text{anti-c.w. for MHy}^+ \text{ at } m - m' \\ \text{c.w. for MHy}^+ \text{ at } n - n' \end{cases}$$

$$\phi = 0.015 \theta, \quad \psi = 1.17 \theta, \quad j = 1.13 \theta$$

The rotation is done from the *guest* orientation at $m - m'$ in Phase-I to Phase-II-like $(\sim II)_{21}$, as in Fig. S8(a). $(\sim II)_{21}$ is also referred to as the new LT-phase. We have estimated the Euler angles of rotation (ϕ , θ , ψ about z , x and z' -axes, respectively) involved in this transformation (from $(I)_{11}$ to $(\sim II)_{21}$ (new LT-phase)). The Euler angles of rotation are shown in Fig. S8(b). The total rotation matrix is given by Eq. S.12. A similar methodology was adopted in studying ferroelectric polarization of MAPbI_3 [36].

$$R = R_z(\phi)R_x(\theta)R_{z''}(\psi) = \begin{bmatrix} \cos(\phi)\cos(\psi) - \cos(\theta)\sin(\phi)\sin(\psi) & \cos(\phi)\sin(\psi) + \cos(\psi)\cos(\theta)\sin(\phi) & \sin(\phi)\sin(\theta) \\ -\cos(\psi)\sin(\phi) - \cos(\phi)\cos(\theta)\sin(\psi) & \cos(\phi)\cos(\psi)\cos(\theta) - \sin(\phi)\sin(\psi) & \cos(\phi)\sin(\theta) \\ \sin(\psi)\sin(\theta) & -\cos(\psi)\sin(\theta) & \cos(\theta) \end{bmatrix} \quad (\text{S.12})$$

The transformation of the following three vectors in $(I)_{11}$ is observed to find the matrix \mathbf{R} : $\vec{v}_1 = \overrightarrow{N_2N_1} = \vec{N}_2 - \vec{N}_1$, $\vec{v}_3 = \overrightarrow{C_1N_1} = \vec{C}_1 - \vec{N}_1$ and $\vec{v}_2 = \hat{v}_1 \times \hat{v}_3$. The vectors are represented in Fig. S9.

Using $M_{Final} = MR$, with the middle nitrogen atoms of both the $(I)_{11}$ and $(\sim II)_{21}$ structures at the origin, we find the ' R' '-matrix which nearly follows the properties of a proper rotation ($\det(\mathbf{R})=1$ and $R^T R = \mathbb{1}$). Here $\det(\mathbf{R}) \approx 0.9954$, and $R' R$ is close to identity matrix.

$$R' R = \begin{bmatrix} 0.9990 & -0.0016 & -0.0016 \\ -0.0016 & 0.9945 & -0.0016 \\ -0.0016 & -0.0016 & 0.9974 \end{bmatrix} \quad (\text{S.13})$$

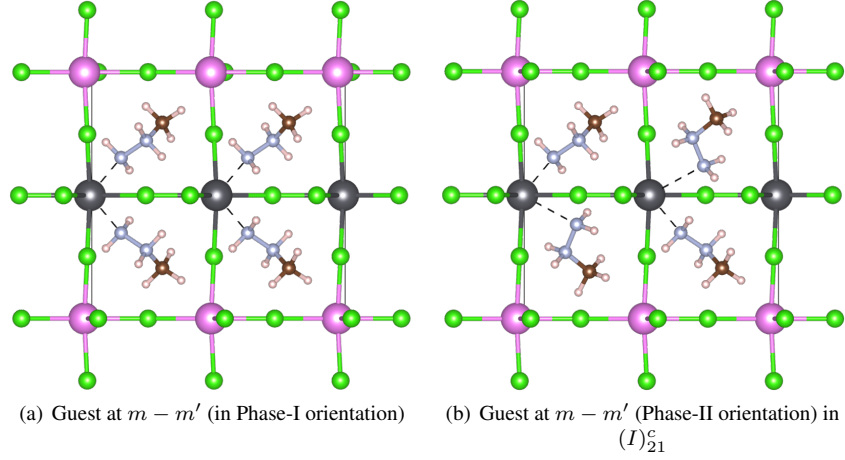


FIG. S10. Transformed *guest* from Phase-I to Phase-II orientation in the presence of *host* distortion of Phase-I for Berry phase calculations. Since the *host* is kept frozen during this transformation for polarization calculation variation along this path, hence the first structure is $(I)_{11}$, and the second structure is $(I)_{21}^c$.

On comparing the matrix R with Eq. S.12, we get $\phi = 1.15^\circ$, $\theta = 79.60^\circ$, $\psi = 93.22^\circ$. A proper rotation matrix, R , is thus expressed by substituting these values in Eq. S.12.

$$R = \begin{bmatrix} -0.0598 & 0.9980 & 0.0199 \\ -0.1790 & -0.0303 & 0.9834 \\ 0.9820 & 0.0552 & 0.1805 \end{bmatrix} \quad (\text{S.14})$$

The transformation involves both the rotation and the translation of the A-site ions, where the translation vector, T , is given by Eq. S.15.

$$T = [0.7338 \quad -0.5978 \quad 0.0982] \quad (\text{S.15})$$

These R - and T - matrices define the net transformation across the two phases. The transformed *guest* ions are represented in Fig.S10(a) and Fig. S10(b) in the presence of Phase-I *host* atoms.

The values for rotation parameter to obtain the new transformed structure, $(I)_{21}^c$ are: $\phi = 1.15^\circ$, $\theta = 79.60^\circ$, $\psi = 93.22^\circ$. The intermediate structures between $(I)_{11}$ and $(I)_{21}^c$ are obtained by discrete rotation as suggested by Eq. S.12. There is an energy difference of about 13 meV/f.u. in the final structure with respect to $(\sim II)_{21}$, as is seen in the inset of Fig. S11(a). This difference arises due to the rigid rotation of the molecule at $m - m'$, where we do not allow any relaxation of the internal angles due to rigid rotation being carried out. This includes the very slight differences in the internal coordinates of the molecule, such as the C1-N1-N2 bond angle, positions of hydrogen atoms associated with the molecule, etc., which would not significantly change any characteristics of the system. However, since both of them are structurally very similar, and hence are labeled as $(\sim II)_{21}$.

Fig. S11(a) shows the energy barrier between the optimized Phase-I and the final $(\sim II)_{21}$ structures, which is obtained by geometry optimization of each of the intermediates, except that of reoriented-*guest* at $m - m'$. A huge energy barrier of around ~ 0.3 eV/unit is evident of rotational immobility of the *guest*, indicative of a *guest* driven phase transition. The 1st image is equivalent to $(\sim II)_{11}$, which is obtained from optimizing the minima obtained by following the unstable phonon mode of Phase-I. Hence, its energy is lower than that of Phase I. However, its symmetry is lowered and no longer belongs to the Phase-I space group, $Pb2_1m$, but rather has a space group similar to Phase-II ($P2_1$). All the structures starting from the 1st image have the space group that of Phase-II ($P2_1$), but *guest* orientation still remains close to Phase-I until the transition state is achieved. In the meantime, the *host* has already transitioned to Phase-II, as can be seen from Fig. S11(b). The results are further verified by carrying out a minimum energy path (MEP) simulation through NEB, starting from the above-obtained set of intermediates. The parameters describing the *guest* orientation and *host* distortion of the path determined by fixed-cell NEB (fc-NEB) are tabulated in Table S10, where the cell has been kept fixed during simulation. We have also carried out variable-cell NEB (vc-NEB) where the transition happens between Phase-I and Phase-II. The corresponding energy barrier and the transition character (TC) have been represented in Fig. S12 and Fig. S13(c), respectively. The color coding and values around the transition point show the dominating nature of the *guest* in causing the phase-transition, along with the contribution from *host*.

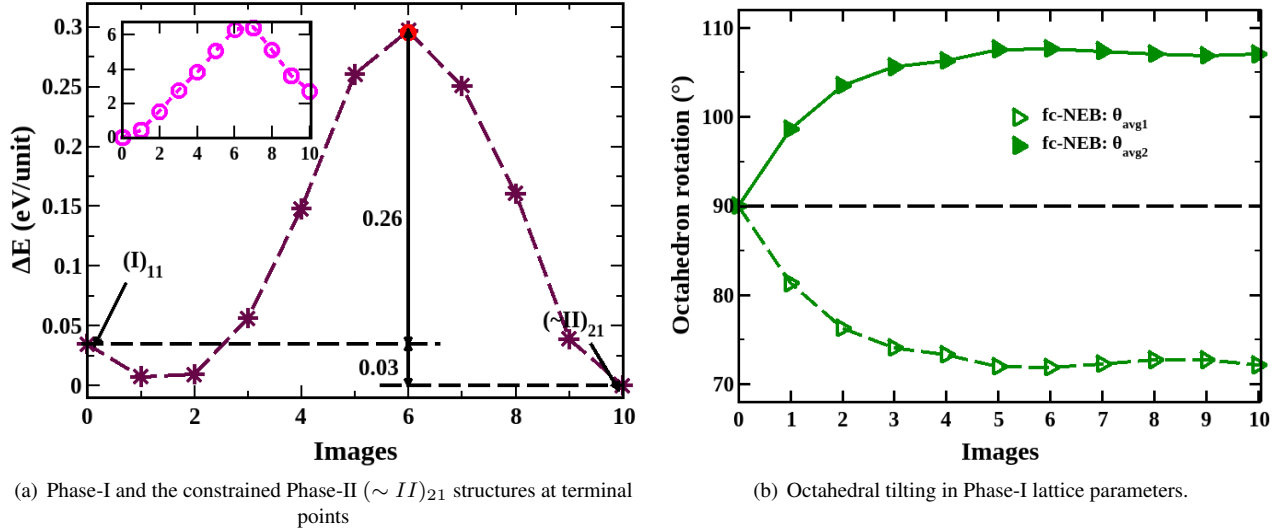


FIG. S11. (a) Rotational energy barrier as a function of images. Maroon curve denotes fixed cell NEB (fc-NEB) to estimate the rotational barrier between $(I)_{11}$ and $(\sim II)_{21}$ of MHyPbCl_3 in Phase-I lattice parameters. The red spot is the transition state. The pink curve in the inset is for the barrier encountered in the Phase-I lattice parameters with fixed *host*. (b) Octahedral tilting for the images across the transition paths. $\theta_{avg1} = (\theta_{m1} + \theta_{n1})/2$ and $\theta_{avg2} = (\theta_{m2} + \theta_{n2})/2$. The green triangles are for the intermediate structures obtained from CI-NEB with Phase-I and $(\sim II)_{21}$ as the end structures. The lines are a guide to the eye.

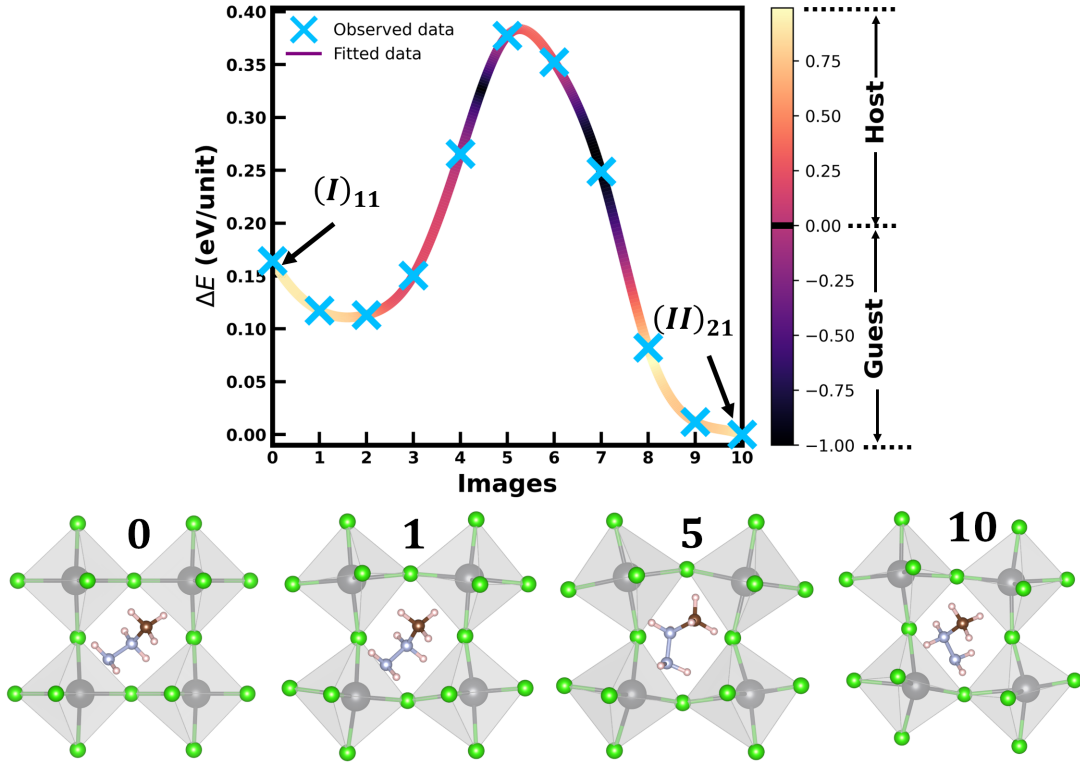


FIG. S12. Energy barrier and the relative contribution of *guest/host* towards phase transition as is shown by the color code for a variable cell NEB (vc-NEB) carried out from Phase-I to Phase-II (both completely optimized). The curves are fitted by spline interpolation. The structures shown below are the initial (Phase-I), 1st (where *host* distortion is prominent), 5th (the transition point) and the final images $(II)_{21}$. Here, in addition to *guest*-reorientation, *host* distortion is also involved significantly in transition.

The *guest* orientation at $m - m'$ and $n - n'$ and the average *host* distortion in terms of its tilting ($\delta\theta_{ilt}$) for different structures

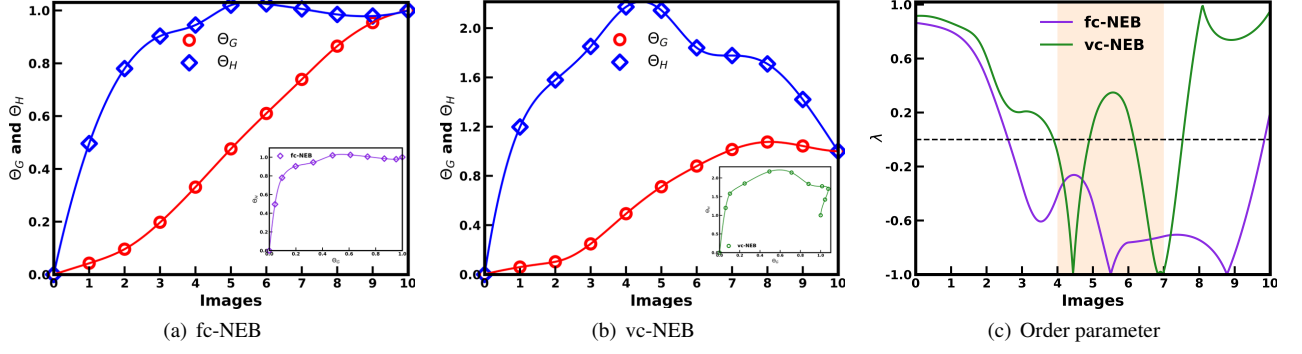


FIG. S13. Relative changes in *guest/host* configuration. The inset shows variation in the *host*-tilting (Θ_H) versus *guest*-orientation (Θ_G) as the transition progresses, as defined in Eqs. S.16 and S.17. The curves are fitted by spline interpolation. fc-NEB is for NEB done in Phase-I lattice parameters. The cell parameters are fixed during the optimization. vc-NEB stands for variable cell NEB where the NEB is carried out between fully optimized (including cell) Phase-I and Phase-II structures which have different cell parameters. (c) Order parameter as a function of reaction coordinates. The shaded region is the region around transition which is initiated predominantly by *guest*-reorientation in both fc- and vc-NEB.

TABLE S10. Parameters for *Guest* orientation and *host* distortion along fc-NEB as calculated from VASP.

| Images | <i>Guest</i> orientation | | | | Octahedral rotation | |
|-----------------------------|---------------------------|----------|----------------------|-----------------|---------------------|-----------------|
| | Normal to molecular plane | | Internal coordinates | | | |
| | θ_n | ϕ_n | ω_{1int} | ω_{2int} | θ_{avg1} | θ_{avg2} |
| Phase-I | 140.55 | 81.26 | -42.48 | 36.94 | 89.97 | 89.97 |
| 1 | 133.32 | 82.07 | -42.06 | 36.41 | 81.30 | 98.62 |
| 2 | 126.35 | 84.96 | -37.70 | 40.34 | 76.28 | 103.48 |
| 3 | 119.62 | 90.89 | -26.78 | 52.33 | 74.03 | 105.55 |
| 4 | 115.00 | 99.10 | -12.51 | 71.09 | 73.27 | 106.25 |
| 5 | 109.97 | 109.59 | 1.91 | 93.17 | 71.96 | 107.54 |
| 6 | 101.67 | 121.60 | 13.59 | 114.11 | 71.88 | 107.62 |
| 7 | 87.77 | 134.29 | 22.51 | 132.91 | 72.27 | 107.36 |
| 8 | 69.40 | 146.69 | 29.00 | 147.97 | 72.68 | 107.04 |
| 9 | 54.18 | 158.15 | 31.71 | 156.02 | 72.68 | 106.82 |
| ($\sim II$) ₂₁ | 45.58 | 166.47 | 32.10 | 159.50 | 72.11 | 106.99 |

have been tabulated below for comparison. The averaged $\delta\theta_{tilt}$ perpendicular to *a*-axis for Phase-I is 0° , i.e., $(\theta_{m1} + \theta_{m2} + \theta_{n1} + \theta_{n2}) = 90^\circ$ (Refer to Fig. 2(iii) in the main text for these angles).

The primary effect leading to the phase transition is decided by the relative slopes of variation of the *guest* and the *host* parameters. Keeping track of this factor, as defined by TC, during the transition helps us decide which of the two would contribute most towards the transition. Transition character (TC) denoted by λ and defined by Eq. S.18 has been plotted in Fig. S13.

The plots shown by Fig. S12 and Fig. S13 show the dominating role of the *guest* reorientation across the transition path irrespective of the lattice parameters (fixed-cell or variable-cell).

B. Transition character (TC)

We evaluate the transition character (TC) using the *host*-tilting and *guest*-orientation parameters. The definitions are given as follows:

- *Host*-tilting: Defined for i^{th} -structure by $\Theta_{H,i}$ as follows:

$$\Theta_{H,i} = \sum_{j \leq i} \Delta\theta_{H,j} \quad (\text{S.16a})$$

TABLE S11. *Host* distortion and *Guest* orientation for different structures in terms of % deviation from Phase-I.

| Structures | Host-tilting $\Delta\theta_H$ | Guest-orientation $\Delta\theta_G$ |
|------------------------------|----------------------------------|---------------------------------------|
| $(I)_{11}$ | 0 | 0 |
| $(\sim II)_{11}$ | 63.6 | 38.8 |
| $(II)_{11}$ (before relax) | 55.2 | 0 |
| $(II)_{11}$ (after relax) | 57.1 | 33.6 |
| $(II)_{11}$ (after vc-relax) | 100 | 100 |
| $(\sim II)_{21}$ | 97.6 | 833.35 |
| $(II)_{21}$ | 55.2 | 743.5 |

$$\Delta\theta_{H,i} = (\delta\theta_{H,i} - \delta\theta_{H,i-1})/\delta\theta_{H,fin} \quad (\text{S.16b})$$

$$\delta\theta_{H,i} = \theta_{H,i} - \theta_{H,ref} \quad (\text{S.16c})$$

- *Guest*-reorientation: Defined for i^{th} -structure by $\Theta_{G,i}$ as follows:

$$\Theta_{G,i} = \sum_{j \leq i} \Delta\theta_{G,j} \quad (\text{S.17a})$$

$$\Delta\theta_{G,i} = \sqrt{(\Delta\omega_{norm,i}^2 + \Delta\omega_{int,i}^2)} \quad (\text{S.17b})$$

$$\omega_{norm,i} = \cos^{-1}(\mathbf{v} \cdot \mathbf{v}_0) \quad (\text{S.17c})$$

$$\Delta\omega_{norm,i} = \frac{(\delta\omega_{norm,i} - \delta\omega_{norm,i-1})}{\delta\omega_{norm,fin}} \quad (\text{S.17d})$$

$$\delta\omega_{norm,i} = \omega_{norm,i} - \omega_{norm,ref} \quad (\text{S.17e})$$

$$\Delta\omega_{int,i} = (\delta\omega_{int,i} - \delta\omega_{int,i-1})/\delta\omega_{int,ref} \quad (\text{S.17f})$$

$$\delta\omega_{int,i} = \omega_{int,i} - \omega_{int,ref} \quad (\text{S.17g})$$

- TC: Defined for i^{th} -structure by λ_i which is the ratio of the difference of the slopes of relative changes of *host/guest* configurations to the sum of their slopes, as follows:

$$\lambda = \frac{|\Delta\theta_{H,i}| - |\Delta\theta_{G,i}|}{|\Delta\theta_{H,i}| + |\Delta\theta_{G,i}|}, \quad -1 \leq \lambda \leq 1 \quad (\text{S.18})$$

The subscript (*ref, fin*) is for initial (0^{th} , Phase-I) and the final (Phase-II/Phase-II-like) structures, respectively. H stands for *host* and G stands for *guest*. \mathbf{v} is the unit vector of the normal to the molecular of a particular structure (defined by θ_n, ϕ_n), with \mathbf{v}_0 being the same for the Phase-I or the 0^{th} structure. $\omega_{int,i}$ is the angle that one of the molecular vectors ($CN1$ or $N2N1$) makes with the crystal a -axis. $\delta\theta_i$ is equal to $\delta\theta_{tilt}$, since the reference phase, Phase-I has the $\theta_{tilt} = \theta_{ref} = 90^\circ$, same as that of cubic phase. Refer to Eq. S.5 for the definition of $\delta\theta_{tilt}$. $\Theta_{H,i}$ and $\Theta_{G,i}$ are the measures of the deviation of the *host*-tilting and *guest*-ordering of the i^{th} -structure with respect to the Phase-I (reference) structure. For the reference phase, $\Theta_H = 0$ as well as $\Theta_G = 0$. $\Delta\theta_{H,i}$ and $\Delta\theta_{G,i}$ are the slopes calculated by backward difference of $\Theta_{H,i}$ and $\Theta_{G,i}$, respectively.

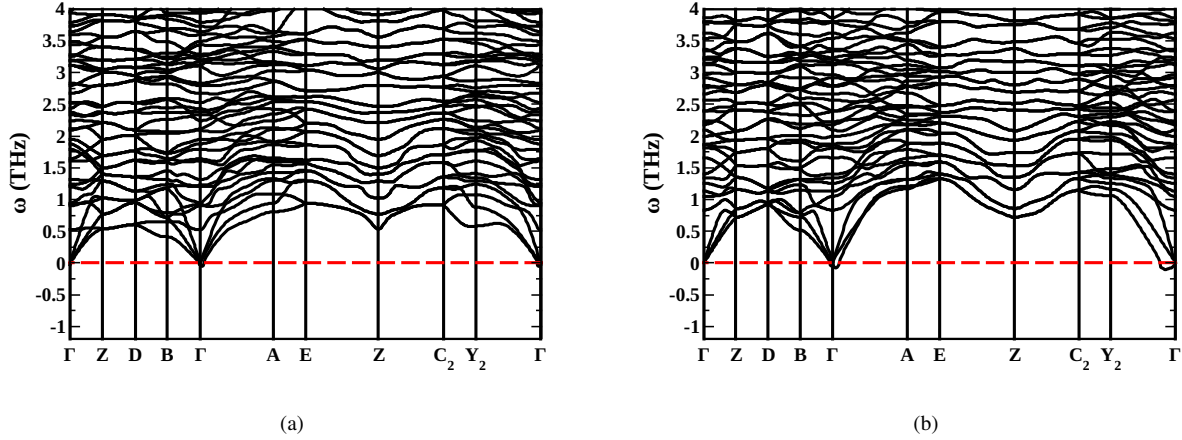


FIG. S14. Phonon dispersion curves for (a) $(\sim II)_{21}$. (b) $(II)_{21}$. Absence of any imaginary frequency implies that both these structures are dynamically stable.

TABLE S12. Polarization as evaluated from Berry phase for different structures^a (in $\mu\text{C}/\text{cm}^2$).

| Structures | P | $P - P_{\text{quanta}}^b$ | ΔP ($\mu\text{C}/\text{cm}^2$) |
|------------------|--------|---------------------------|--|
| $(I)_{11}$ | -17.78 | 8.99 | 0 |
| $(\sim II)_{11}$ | -17.58 | 9.19 | 0.20 |
| $(I)_{21}^c$ | 6.28 | 6.28 | -2.71 |
| $(I)_{21}$ | 7.79 | 7.79 | -1.20 |
| $(\sim II)_{21}$ | 6.42 | 6.42 | -2.57 |
| $(II)_{21}$ | 4.71 | 4.71 | -4.28 ^c |

^a non-zero ΔP only along y -direction.

^b For $(I)_{11}$, $P_{\text{quanta}} = 26.78 \mu\text{C}/\text{cm}^2$

^c For $(II)_{21}$, $P_{\text{quanta}} = 26.59 \mu\text{C}/\text{cm}^2$, hence ΔP may not be exact.

C. Host-distortion

The phonon dispersion curves of $(II)_{21}$ (LT-phase) in Fig. S14(b) and $(\sim II)_{21}$ in Fig. S14(a) depict the stability of these structures at 0 K. The structures are dynamically stable within the known numerical error of phonon calculations (~ 0.3 THz). However, Phase-I is dynamically unstable at 0 K as is shown by unstable optical mode (negative frequency) in Fig. S15(a). Displacing the ions along the unstable mode (as explained in the main text), we arrive at a new energy-minimum structure, which when optimized completely (vc-relax) (shown in Fig. S17), tends towards the lattice parameters of Phase-II (Table S9). This structure is labeled as $(II)_{11}$ since the *guest* do not vary significantly in their orientations with respect to Phase-I (according to the cut-offs of 10° defined for respective phase orientations in the main text). The geometry-optimized equivalent of the PES minima is denoted by $(\sim II)_{11}$ and is shown in Fig. S16. But due to the high energy barrier, the *guest* at $m - m'$ do not undergo significant reorientation. The presence of an energy barrier for the dynamically unstable Phase-I is also confirmed by using hybrid functional (PBE0), as is shown in Fig. S15(b). These new energy-minima structures ($(\sim II)_{11}$ and $(II)_{11}$) are dynamically stable as can be seen from their phonon dispersion curves in Fig. S15(c) and Fig. S15(d), respectively.

All the structures investigated in this study are plotted on an energy scale with respect to Phase-I in Fig. S18.

S-V. POLARIZATION

Table S12 contains the polarization values of several constructed structures of MHyPbCl_3 as calculated from Berry phase approach [38–41]. It must be noticed that since the organic entities (*guest*) carry a positive charge independently (*i. e.* A^+), hence the calculation of dipole moment depends on the choice of origin. Eq. S.19 gives the dipole moment for a charged system.

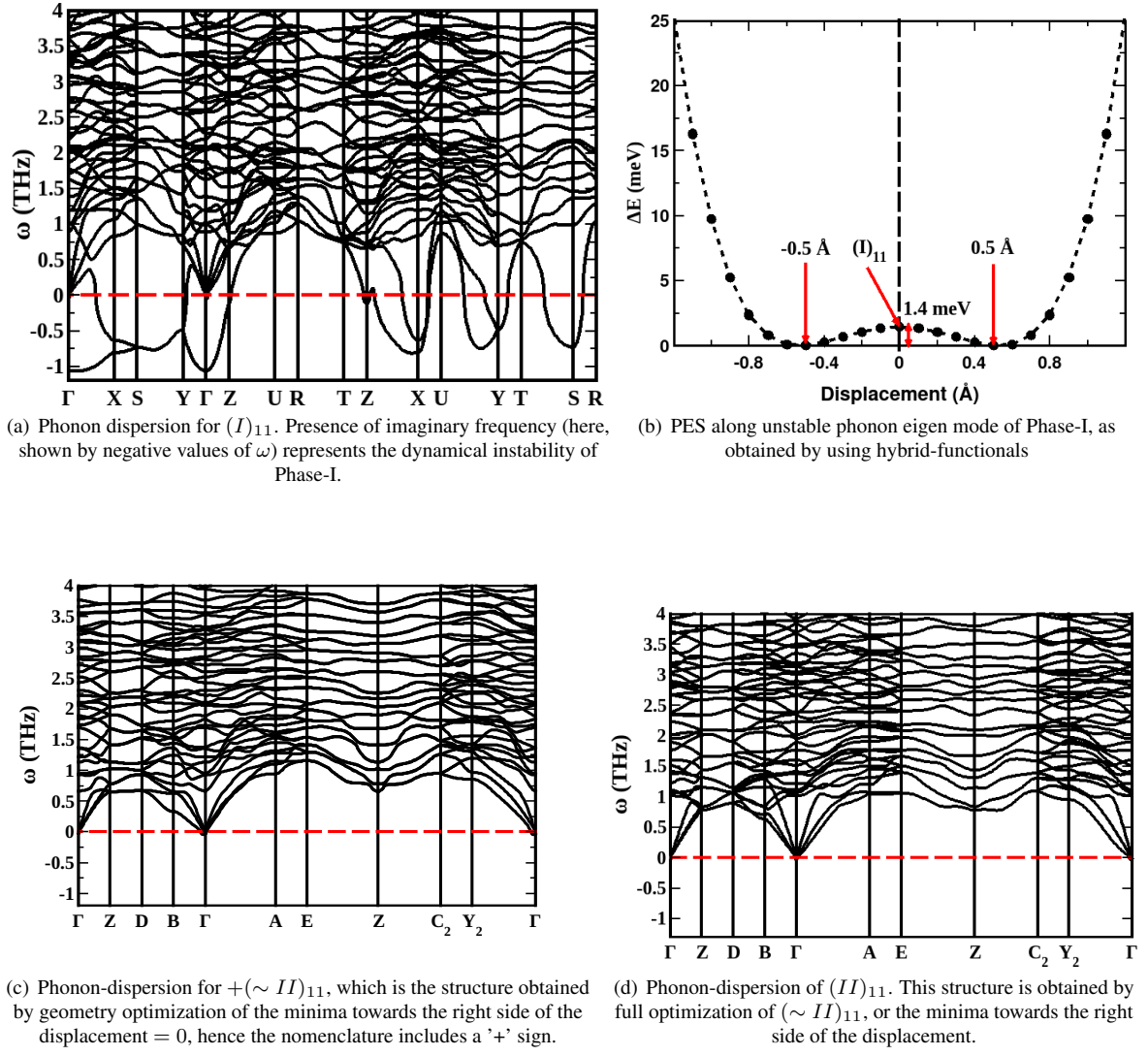


FIG. S15. (a), (c) and (d) Phonon dispersion curves of different phases of MHyPbCl₃. Phase-I is dynamically unstable, as is evident from the presence of imaginary phonon frequencies. The PES generated in Fig.4b (GGA-XC) in the main text and (b) (hybrid functional) by following this mode shows two dynamically stable energy-equivalent states. The absence of any imaginary mode in (c), and (d) tells that these two structures, which are obtained from geometry ($(\sim II)_{11}$), and full ($(II)_{11}$) relaxation of energy-minimum states of (b) are dynamically stable. The plots are shown for structures corresponding to the right-minima, the left-minima also shows similar dispersion cures and dynamical stability.

$$\mathbf{p}' = \int \mathbf{r}' \rho(\mathbf{r}) d\mathbf{r} = \mathbf{d} - \mathbf{r}_0 Q \quad (\text{S.19})$$

where $\mathbf{d} = \int \mathbf{r} \rho(\mathbf{r}) d\mathbf{r}$, is the dipole moment for a neutral system, \mathbf{r}_0 is the position vector of the origin and center of charge, Q is the net charge on the *guest* [36]. The middle nitrogen atom in the *guest* molecule is taken as the reference during transformation.

The convergence of polarization values has been checked with the k -mesh grid points along y -direction since there is no net polarization along both the x and z -axes. The convergence of polarization with the number of k -points is shown in Fig. S19. We have chosen $k = 10$ for further calculations on polarization.

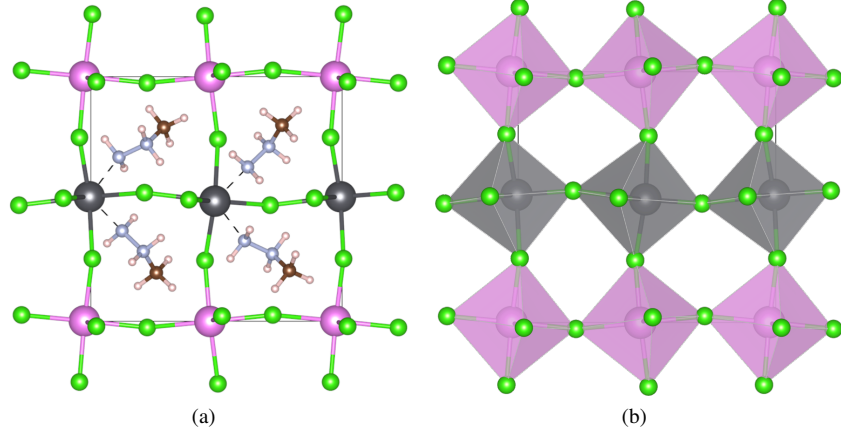


FIG. S16. The structures obtained after geometry optimization of the structure at one of the minima of the PES (Fig. 4b of main text) which is calculated along the unstable eigen-mode of Phase-I, labelled as (a)($\sim II$)₁₁. (b) Octahedral distortion of (a).

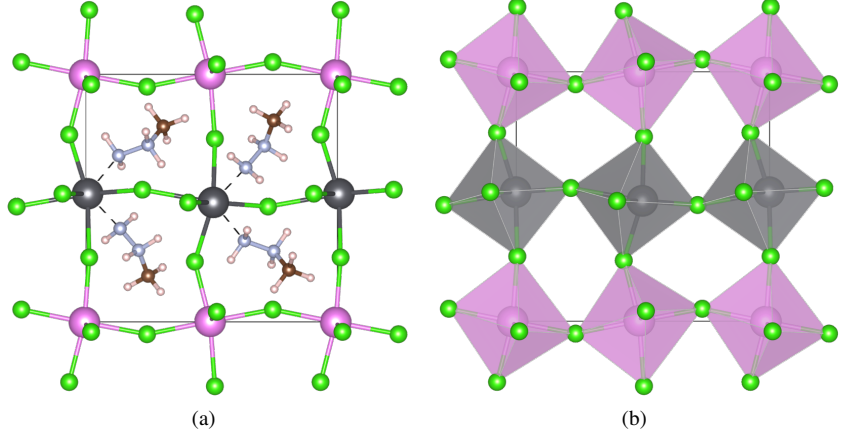


FIG. S17. The structures obtained after cell/full optimization of the structure at one of the minima of the PES (Fig. 4b of main text) which is calculated along the unstable eigen-mode of Phase-I, labelled as (a)(II)₁₁ (full optimized structure of ($\sim II$)₁₁). (b) Octahedral distortion of (a).

A. Role of *guest* reorientation

Polarization differences with respect to (I)₁₁ with and without the *host* has been shown in Fig. 5 in main text for b3lyp/6-311g(2d,2p) functional [42–46]. A minimum of polarization at the 9th image in Fig. 5 in the main text, which also corresponds to $\theta = 64^\circ$ (transformation coordinate) in Fig. S21 tells that there is a possibility of yet another configuration of the *guest* which can further bring down the polarization of the system, but is not a ground state orientation.

Polarization differences with respect to (I)₁₁ during the transformation of *guest* independently is plotted in Fig. S21 for b3lyp/6-311g(2d,2p) functional and in Fig. S22(a) for pbepbe/6-31+g(d,p) functional [29, 47, 48]. The positions $m - m'$ and $n - n'$ are marked in Fig. S10(a). pbepbe/6-31+g(d,p) functional is used to match the level of theory with which the calculations

TABLE S13. Comparison of ΔP ($\mu C/cm^2$) with respect to (I)₁₁ as evaluated from MLWFs with those obtained from Berry phase approach.^a

| | $(I)_{21}^c - (I)_{11}$ | $(I)_{21} - (I)_{11}$ | $(\sim II)_{21} - (I)_{11}$ | $(II)_{21} - (I)_{11}$ |
|-------------------------|-------------------------|-----------------------|-----------------------------|------------------------|
| Lattice (MLWF) | -1.16 | -1.16 | -2.30 | -3.63 |
| MHy ⁺ (MLWF) | -1.54 | -0.03 | -0.24 | -0.64 |
| Total (MLWF) | -2.68 | -1.18 | -2.54 | -4.27 |
| Total (Berry) | -2.71 | -1.20 | -2.57 | -4.28 |

^a Net polarization exists only along y -direction.

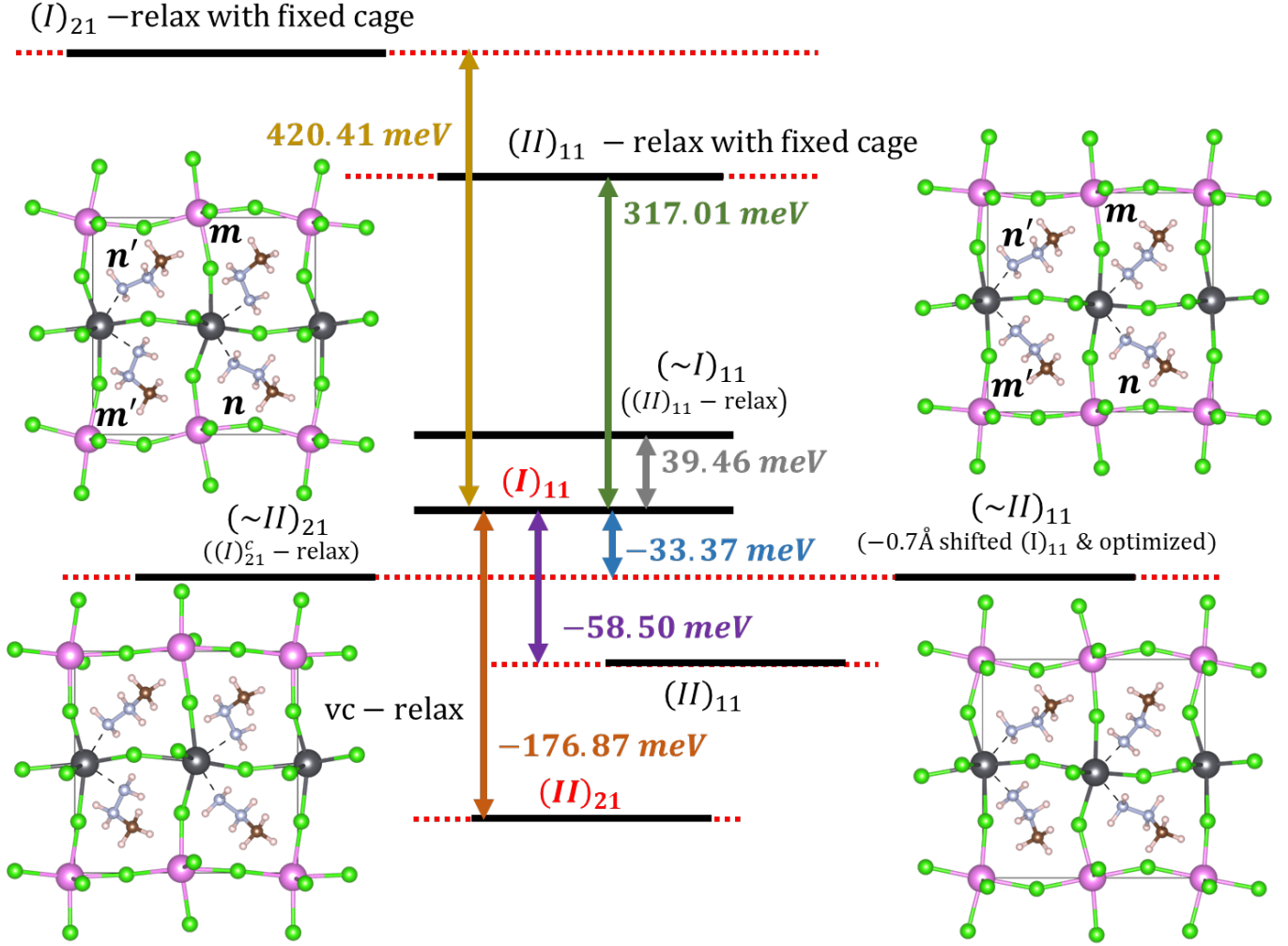


FIG. S18. Energy scaling of the several structures with respect to $(I)_{11}$ of MHyPbCl₃ investigated in this work. ‘vc-relax’ implies variable-cell optimization, which is done for the two energy equivalent geometries, $(\sim II)_{11}$, and $(\sim II)_{21}$. $(\sim II)_{11}$ -vcr is, in fact $(II)_{11}$, and $(\sim II)_{21}$ -vcr is $(II)_{21}$. Their energy levels show that these structures on cell optimization acquire Phase-II symmetry and lattice parameters. The ‘ $(II)_{11}$ ’ structures are higher in energy because of the inability of the *guest* ions to rotate to Phase-II orientation.

are done in the presence of lattice-ions. However, the net values do not vary significantly with the functionals. Fig. S22(b) shows the variation in the polarization with and without the *host* for rigid rotation of the molecular dipoles for pbepe/6-31+g(d,p) functional. There is no significant difference in ΔP with the change in functionals (Fig. S22).

B. Disentangling different components of polarization

MLWFs have been employed to separate out the contribution of each element to the net polarization in MHyPbCl₃. The polarization per unit cell can be defined as the dipole moment of the Wannier charge density (Eq. S.20) [50–54].

$$\mathbf{p}_e = -e \sum_n \int d^3r \mathbf{r} |W_n(\mathbf{r})|^2 \quad (\text{S.20})$$

Each WC corresponds to a charge of $-2e^-$ for a spin-unpolarized system. Hence the WCs are associated with the electronic polarization of the system, whereas the ionic polarization is obtained from the atomic coordinates of the ions. The decomposition would show the extent to which each of the *host* and the *guest* sublattices would contribute to ionic and electronic polarization

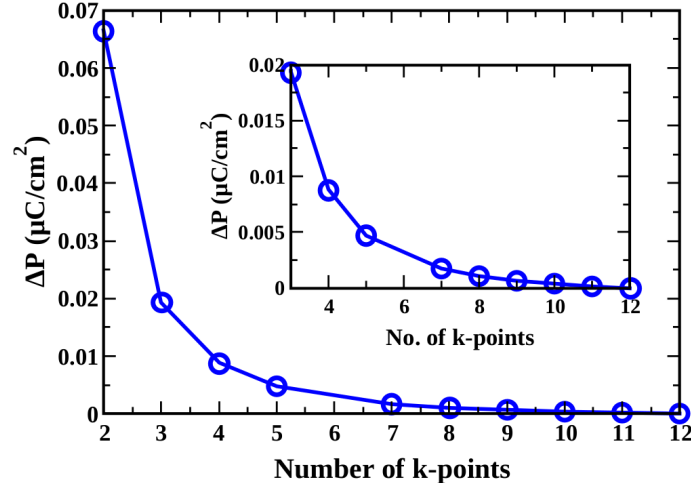


FIG. S19. Convergence of polarization as a function of number of k -points along y -direction.

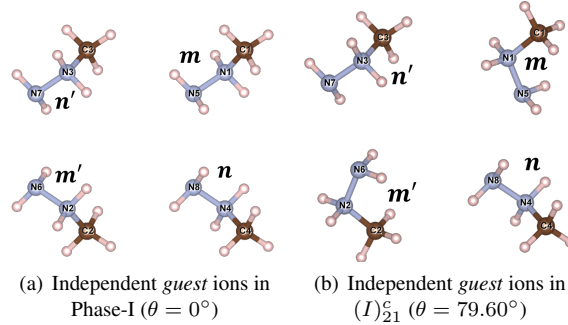


FIG. S20. ((a), (b)) *Guest* treated independently for dipole moment calculation through Gaussian [49] for Phase-I and Phase-II orientations. These are the *guest* ions of Fig. S10, except that the *host* is replaced by a net positive charge on each *guest* for free *guest* calculation since the dipole-dipole interaction does not vary much with reorientation (in terms of its effect on polarization).

individually [50]. The total polarization in terms of electronic and ionic components can, thus be written as in Eq. S.21.

$$\mathbf{P} = \sum_n q_n \mathbf{r}_n + \sum_i q_i \mathbf{r}_i \quad (\text{S.21})$$

Here \mathbf{r}_n is the position of n^{th} nuclei and \mathbf{r}_i is the position vector of i^{th} WC. Wannier centers (WCs) for $(I)_{21}^c$, $(I)_{21}$ and $(II)_{21}$ are shown by magenta colored spheres in Fig. S24. The *guest* atoms are labelled in Fig. S23 for $(I)_{11}$ and $(\sim II)_{21}$.

The ionic and electronic contribution to polarization are compared for the hybrid (MHyPbCl₃) as well as inorganic (CsPbCl₃) perovskites [38, 40, 51, 55–58] and the results are plotted in Fig. S25. The polarization values of MHyPbCl₃ with respect to Phase-I, as evaluated from the ionic positions and WCs, is reported in Tables S14–S16. All the polarization values are reported with respect to Phase-I.

There is a net cancellation of polarization along x and z -axes individually for ionic and electronic polarization. Ionic, electronic, and total contribution to polarization for all the atoms of MHyPbCl₃ along these directions are shown in Figs. S28–S29.

TABLE S14. ΔP_x (with respect to Phase-I) as evaluated from WCs along the suggested phase transformation path (in $\mu\text{C}/\text{cm}^2$).

| Structures | Host | | | Guest | | | Total polarization |
|------------------|-------|------------|-------|-------|------------|-------|--------------------|
| | Ionic | Electronic | Total | Ionic | Electronic | Total | |
| $(I)_{11}$ | 0.00 | 0.00 | 0.00 | 0.00 | 0.00 | 0.00 | 0.00 |
| $(I)_{21}^c$ | 0.00 | 0.00 | 0.00 | 0.00 | 0.00 | 0.00 | 0.00 |
| $(I)_{21}$ | 0.00 | 0.00 | 0.00 | 0.00 | 0.00 | 0.00 | 0.00 |
| $(\sim II)_{21}$ | 0.00 | 0.00 | 0.00 | 0.00 | 0.00 | 0.00 | 0.00 |
| $(II)_{21}$ | 86.11 | -90.24 | -4.13 | 86.34 | -82.24 | 4.10 | -0.03 |

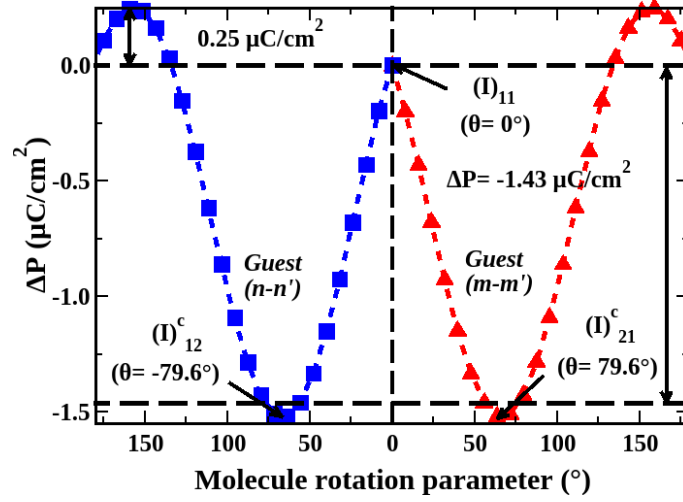


FIG. S21. ΔP as a function of the transformation parameter, θ for isolated *guest* molecules with b3lyp/6-31g(2d,2p) functional. The red curve is taken for the transformation done for the *guest* ions at $m - m'$, whereas the blue curve is for the ions transformed at $n - n'$. The differences are taken with respect to Phase-I. The dotted lines are a guide to the eye.

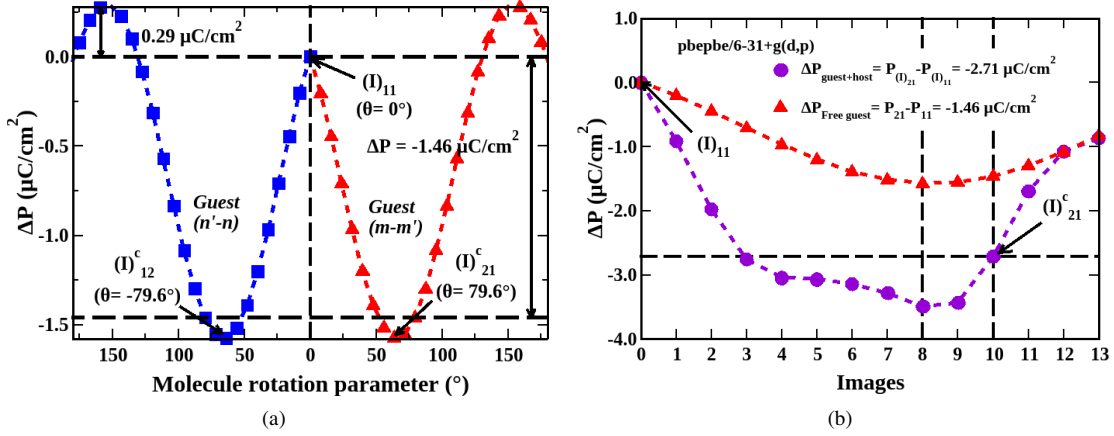


FIG. S22. Polarization as evaluated from (a) GAUSSIAN-16 using pbe/bpe/6-31+g(d,p) for isolated *guest*. (b) Berry phase approach for the periodic system of *guest* in the presence of the *host*. The dotted lines are a guide to the eye.

TABLE S15. ΔP_y (with respect to Phase-I) as evaluated from WCs for different structures (in $\mu\text{C}/\text{cm}^2$).

| Structures | Host | | | Guest | | | Total polarization |
|------------------|-------|------------|-------|-------|------------|-------|--------------------|
| | Ionic | Electronic | Total | Ionic | Electronic | Total | |
| $(I)_{11}$ | 0.00 | 0.00 | 0.00 | 0.00 | 0.00 | 0.00 | 0.00 |
| $(I)_{21}^c$ | 0.00 | -1.16 | -1.16 | 6.84 | -8.38 | -1.54 | -2.70 |
| $(I)_{21}$ | 0.00 | -1.16 | -1.16 | 34.62 | -34.65 | -0.03 | -1.19 |
| $(\sim II)_{21}$ | 82.60 | -84.92 | -2.32 | 34.62 | -34.88 | -0.26 | -2.58 |
| $(II)_{21}$ | 95.69 | -99.34 | -3.65 | 40.19 | -40.82 | -0.64 | -4.27 |

TABLE S16. ΔP_z (with respect to Phase-I) as evaluated from WCs for different structures (in $\mu\text{C}/\text{cm}^2$).

| Structures | Host | | | Guest | | | Total polarization |
|------------------|-------|------------|-------|-------|------------|-------|--------------------|
| | Ionic | Electronic | Total | Ionic | Electronic | Total | |
| $(I)_{11}$ | 0.00 | 0.00 | 0.00 | 0.00 | 0.00 | 0.00 | 0.00 |
| $(I)_{21}^c$ | 0.00 | 0.00 | 0.00 | 0.00 | 0.00 | 0.00 | 0.00 |
| $(I)_{21}$ | 0.00 | 0.00 | 0.00 | 0.00 | 0.00 | 0.00 | 0.00 |
| $(\sim II)_{21}$ | 0.00 | 0.00 | 0.00 | 0.00 | 0.00 | 0.00 | 0.00 |
| $(II)_{21}$ | 38.83 | -39.36 | -0.53 | 11.30 | -10.75 | 0.55 | 0.02 |

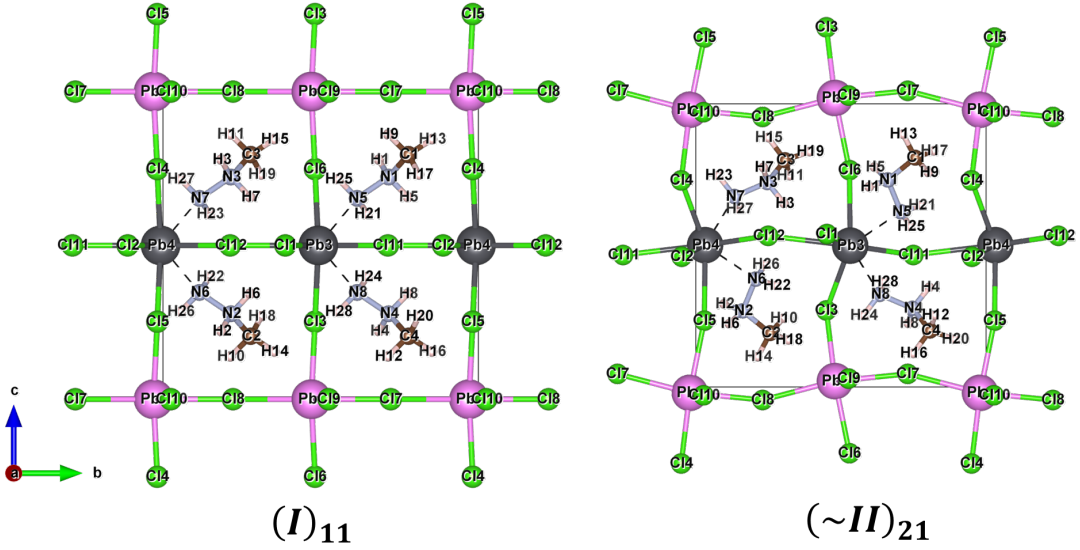


FIG. S23. Labeling of *guest* and *host* atoms in Phase-I and ($\sim II$)₂₁.

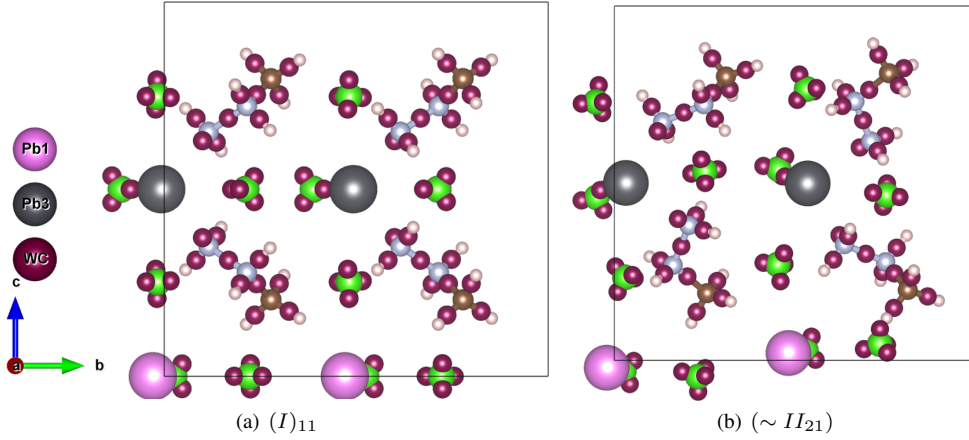


FIG. S24. Wannier centers associated with the *guest* and the *host* for Phase-I, (I)₁₁ and Phase-II under the constraints of Phase-I lattice parameters, ($\sim II$)₂₁.

The values are plotted separately for the *guest* and the *host* sublattices.

C. Polarization feedback (Effect of the *host* on the *guest*)

The first contribution to polarization feedback is computed as the change in the electronic polarization of the *guest* due to the introduction of the *host*, as given by Eq. S.22.

$$\Delta P_{G^e} = (P_{G_{10}^e}^H - P_{G_0^e}^H) - (P_{G_{10}^e}^{free} - P_{G_0^e}^{free}) \quad (\text{S.22})$$

For this, we consider only the 0th (Phase-I) and the 10th (Phase-II-like) images of Fig. 5 of the main text. Taking Phase-I as the reference, the first difference quantifies the *guest* electronic polarization (indicated by G^e) for the 10th (hence, denoted by $P_{G_{10}^e}$) with respect to Phase-I in the presence of *host* (indicated by superscript ' H '). The second difference in the equation quantifies the same contribution, but for isolated *guests*, hence indicated by superscript ' $free$ '. The net difference, thus is given by ΔP_{G^e} , which is the electronic polarization induced on the *guest* and is computed by the shift in the *guest* Wannier centers (WCs) in the presence and absence (free/isolated *guest*) of *host*.

The second part of the polarization feedback induced on the *guest* due to *host* distortion is obtained by comparing the distance of the *guests* WCs in the two cases from bond/atom centers in (I)₂₁ and ($\sim II$)₂₁ since they have the same *guest* orientation, but

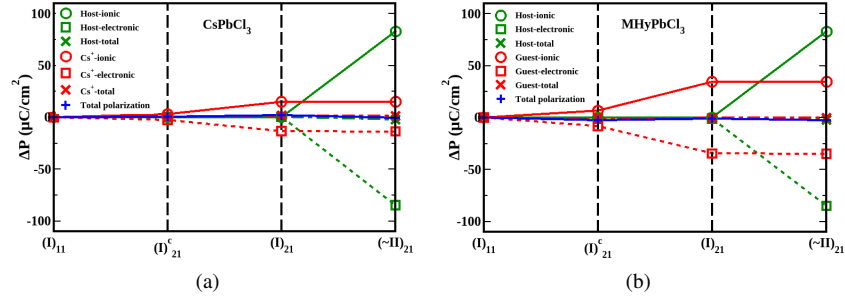


FIG. S25. Ionic and electronic contribution to y -component of polarization due to (a) CsPbCl_3 and (b) MHyPbCl_3 . The respective components along x and z -directions cancel and, therefore, have zero net polarization along these directions.

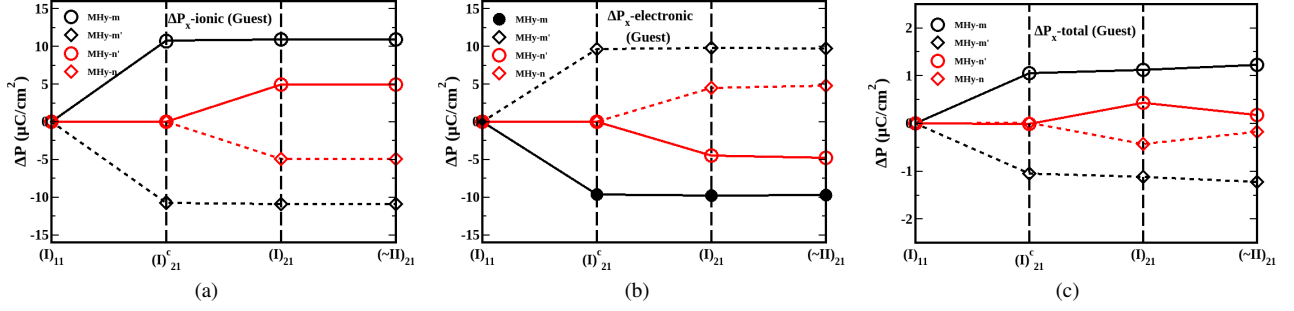


FIG. S26. x -component of polarization of the *guest* (a) Ionic (b) Electronic (c) Total.

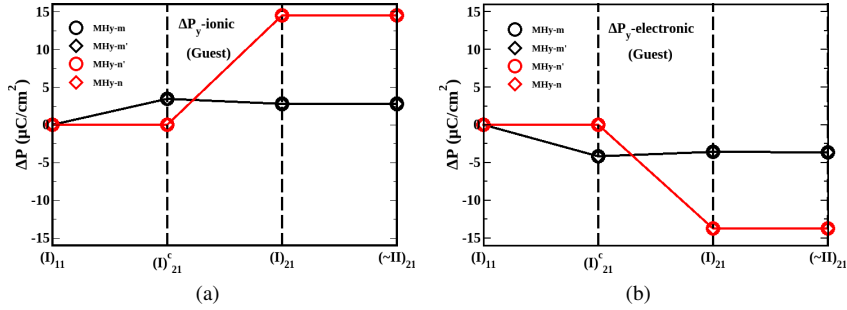


FIG. S27. y -component of polarization of the *guest* (a) Ionic (b) Electronic. The total polarization along y -axis due to *guest* orientation is shown in the main text (Fig. 7(b)).

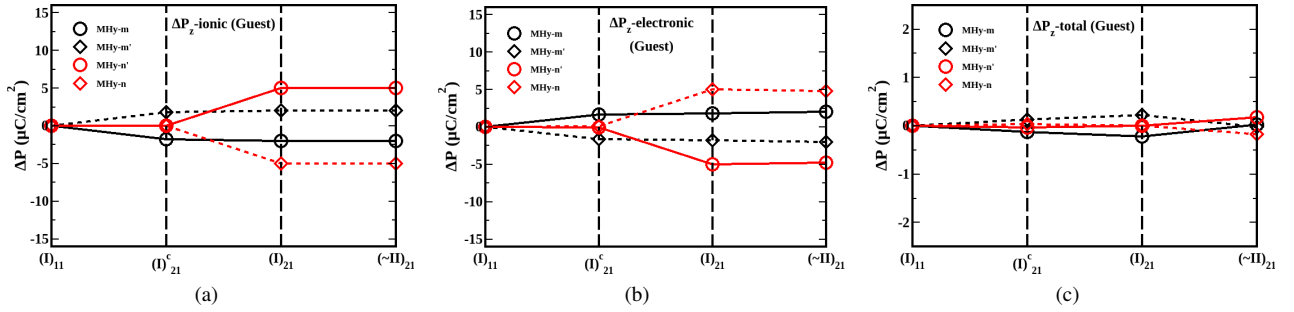


FIG. S28. z -component of polarization of the *guest* (a) Ionic (b) Electronic (c) Total.

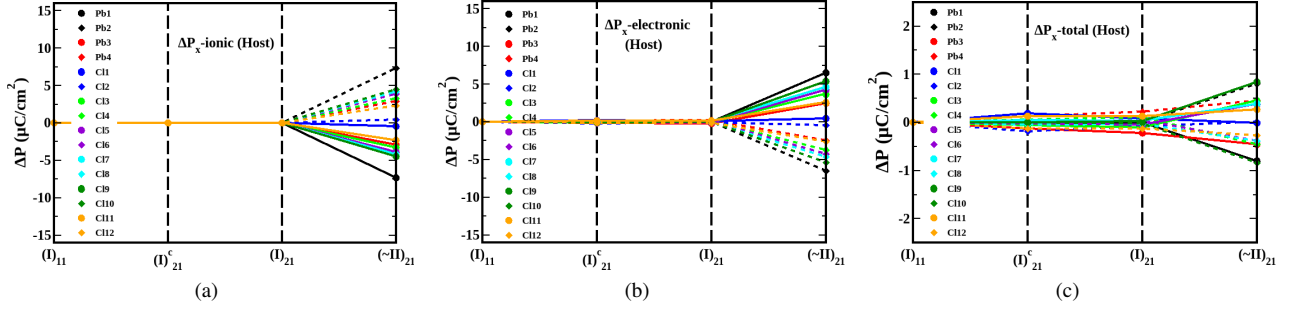


FIG. S29. x -component of polarization of the *host* (a) Ionic (b) Electronic (c) Total.

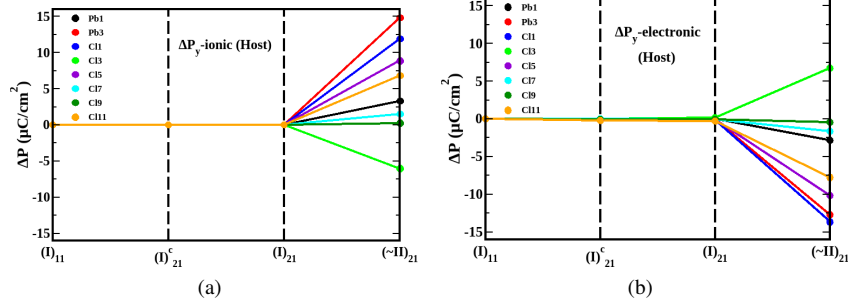


FIG. S30. y -component of polarization of the *host* (a) Ionic (b) Electronic. The total polarization along y -axis due to *host* atoms is shown in the main text (Fig. 7(c)).

different *host* distortions. Hence, any relative shift of the *guest* WCs in the two cases will be evidence of polarization induced on the *guest* by the *host*, hence constitutes another part of the polarization feedback. Table S17 shows the relative shift of WCs, defined as $\delta(\Delta WC) = (\Delta WC)_{(\sim II)_{21}} - (\Delta WC)_{(I)_{21}}$, in all the directions. A non-zero shift indicates an effective electronic polarization contribution (no change in ionic polarization) to the feedback.

S-VI. COUPLING OF POLAR AND ELECTRONIC PROPERTIES

We have employed GGA-functional, which is shown to predict fairly accurate band gaps due to the cancellation of errors because of the non-inclusion of spin-orbit coupling [59, 60]. We obtain the band gap for Phase-II of MHyPbCl₃ as ~ 3 eV (experimental value is 3.4 eV). Band structure and DOS for different structures under consideration (including experimental phases, Phase-I and Phase-II) are plotted in Fig. S33. The band gap values and major contribution of the *host* atoms near the Fermi-level of each of the structures of MHyPbCl₃ (Fig. S33) indicate that these values depend remarkably on *host* distortion. The structure $(\sim II)_{21}$, which is obtained by geometry optimization of $(I)_{21}^c$, has a net stress of around 0.4 GPa and demonstrates a reduction in the band gap. This can be considered one of the alternate approaches to make this compound and other crystal

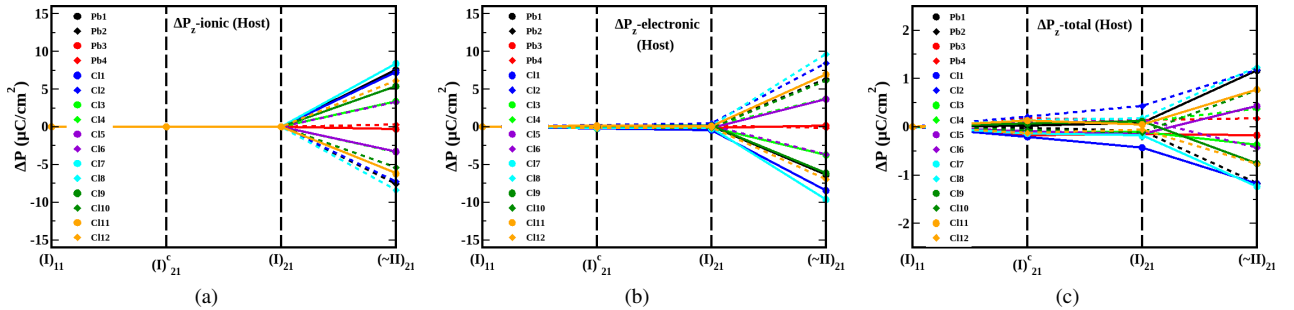


FIG. S31. z -component of polarization of the *host* (a) Ionic (b) Electronic (c) Total.

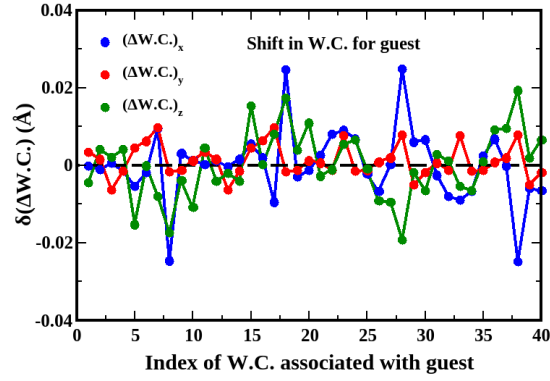


FIG. S32. Change in (ΔWC) of $(\sim II)_{21}$ with respect to $(I)_{21}$ along all the three directions. The values have been tabulated in Table S17.

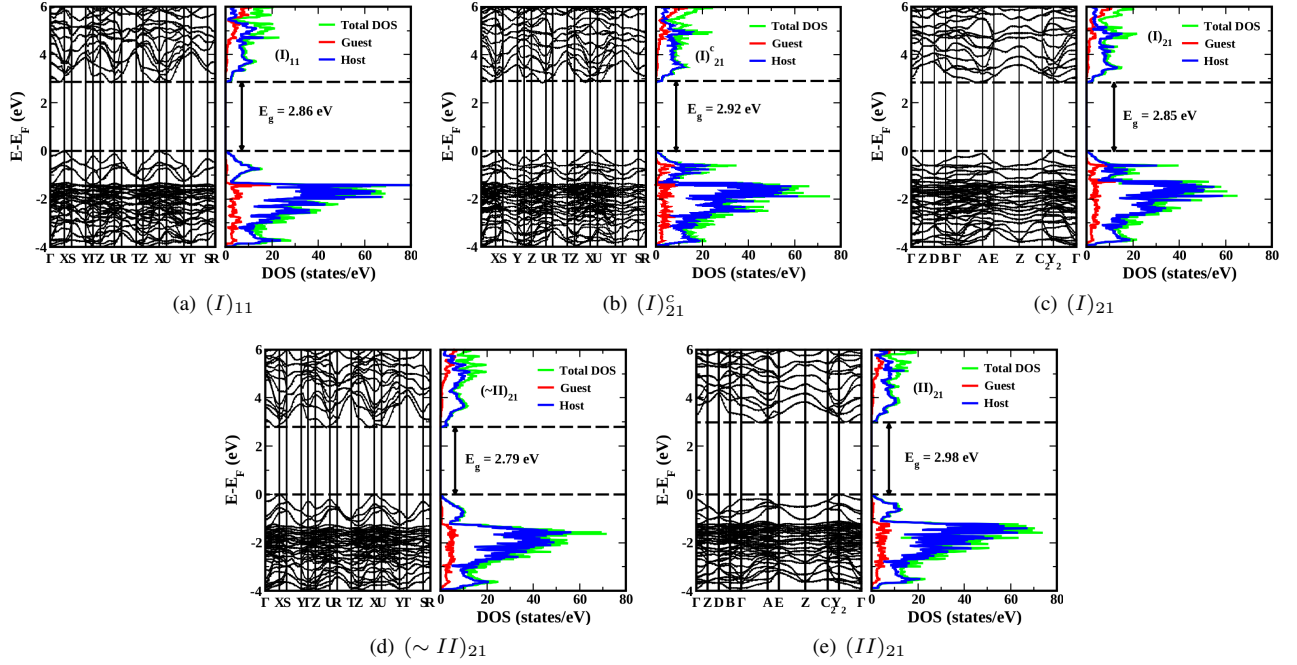


FIG. S33. Band structure and DOS for $(I)_{11}$, $(I)_{21}^c$, $(I)_{21}$, $(\sim II)_{21}$ and $(II)_{21}$, demonstrating the dominance of *host* atoms near Fermi level and the indirect effect of *guest*-orientation on the band-gap.

structures employing MHy^+ at A-site efficient for photovoltaic applications.

PDOS of all the structures as shown in Fig. S34 demonstrate that the contribution due to lead atoms of the more distorted layer (Layer-2) (grey layer in Fig. S1 and S5) change significantly over the evolution of the phases. A similar observation holds for chloride ions of the same layer. Orbital-wise projected density of states in Fig. S35 further shows that the p -orbitals of Cl atoms dominate the valence band and that of lead atoms dominate the conduction bands. sp -hybridized states of Cl and Pb, respectively, can also occupy the conduction bands, as is observed for other similar hybrid perovskites [61–63]. The labeling of the atoms is done in Fig. S23.

TABLE S17. Values of the change in the shift in Wannier-centers, denoted by $\delta(\Delta WC)$ in Å, along all the three directions.

| Bond/atom centers for associating WCs | | $\delta(\Delta WC)_x$ | $\delta(\Delta WC)_y$ | $\delta(\Delta WC)_z$ |
|---|-----|-----------------------|-----------------------|-----------------------|
| C1 | N1 | -0.0002 | 0.0033 | -0.0045 |
| C1 | H9 | -0.0011 | 0.0016 | 0.0041 |
| C1 | H13 | 0.0005 | -0.0064 | 0.0020 |
| C1 | H17 | -0.0016 | -0.0016 | 0.0041 |
| N1 | N5 | -0.0055 | 0.0044 | -0.0153 |
| N1 | H1 | -0.0019 | 0.0062 | -0.0001 |
| N1 | H5 | 0.0095 | 0.0096 | -0.0081 |
| N5 | N5 | -0.0246 | -0.0018 | -0.0174 |
| N5 | H21 | 0.0030 | -0.0014 | -0.0039 |
| N5 | H25 | 0.0013 | 0.0012 | -0.0109 |
| C2 | N2 | 0.0002 | 0.0033 | 0.0045 |
| C2 | H10 | 0.0012 | 0.0016 | -0.0041 |
| C2 | H14 | -0.0005 | -0.0064 | -0.0020 |
| C2 | H18 | 0.0016 | -0.0016 | -0.0041 |
| N2 | N6 | 0.0055 | 0.0045 | 0.0152 |
| N2 | H2 | 0.0019 | 0.0062 | 0.0001 |
| N2 | H6 | -0.0095 | 0.0096 | 0.0081 |
| N6 | N6 | 0.0246 | -0.0017 | 0.0174 |
| N6 | H22 | -0.0030 | -0.0014 | 0.0039 |
| N6 | H26 | -0.0013 | 0.0012 | 0.0109 |
| C3 | N3 | 0.0026 | 0.0006 | -0.0028 |
| C3 | H11 | 0.0080 | -0.0013 | -0.0011 |
| C3 | H15 | 0.0090 | 0.0077 | 0.0054 |
| C3 | H19 | 0.0068 | -0.0016 | 0.0065 |
| N3 | N7 | -0.0023 | -0.0013 | -0.0009 |
| N3 | H3 | -0.0068 | 0.0008 | -0.0092 |
| N3 | H7 | 0.0001 | 0.0019 | -0.0095 |
| N7 | N7 | 0.0249 | 0.0078 | -0.0193 |
| N7 | H23 | 0.0060 | -0.0051 | -0.0019 |
| N7 | H27 | 0.0066 | -0.0019 | -0.0066 |
| C4 | N4 | -0.0026 | 0.0006 | 0.0028 |
| C4 | H12 | -0.0080 | -0.0013 | 0.0011 |
| C4 | H16 | -0.0090 | 0.0077 | -0.0054 |
| C4 | H20 | -0.0068 | -0.0016 | -0.0065 |
| N4 | N8 | 0.0023 | -0.0013 | 0.0009 |
| N4 | H4 | 0.0068 | 0.0008 | 0.0092 |
| N4 | H8 | -0.0001 | 0.0019 | 0.0095 |
| N8 | N8 | -0.0249 | 0.0078 | 0.0193 |
| N8 | H24 | -0.0060 | -0.0051 | 0.0019 |
| N8 | H28 | -0.0066 | -0.0019 | 0.0066 |
| Sum | | 0.0000 | 0.0460 | 0.0000 |
| Total electronic polarization ($\mu C/cm^2$) | | 0.00 | -0.22 | 0.00 |

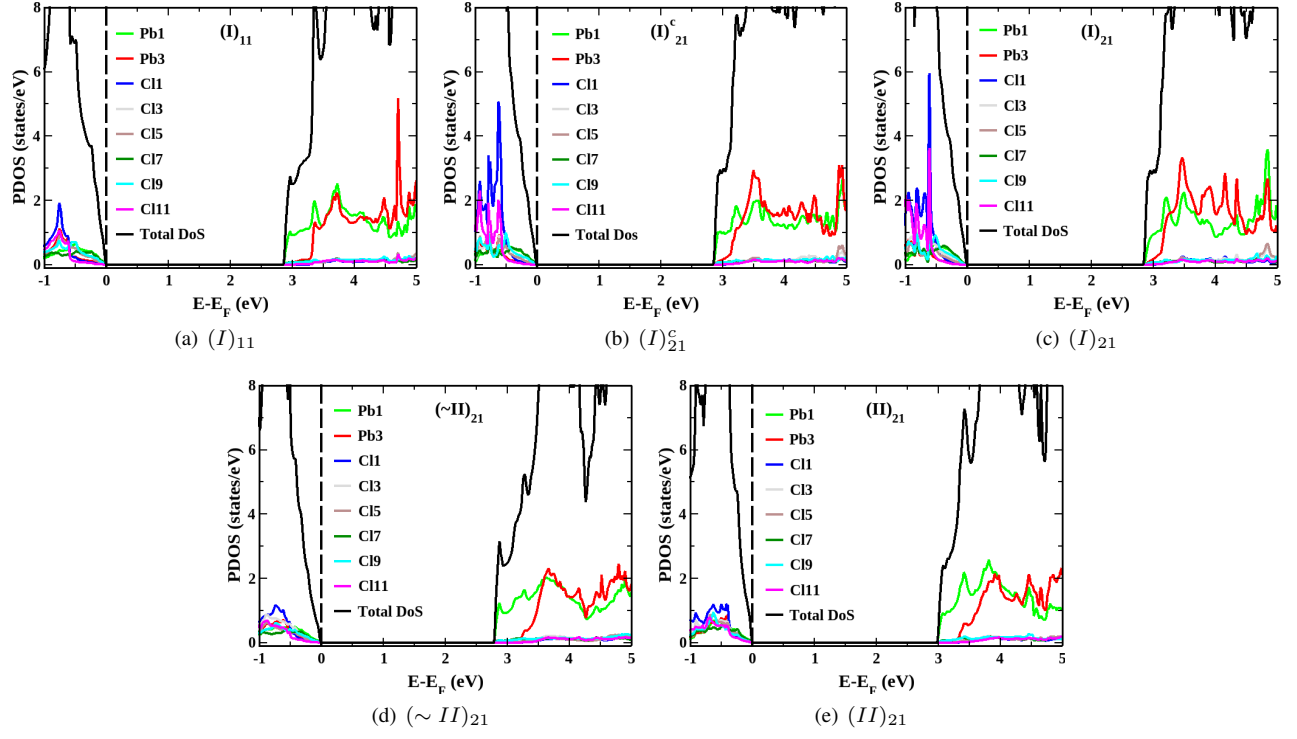


FIG. S34. Atom Projected Density of States (PDOS) of different structures studied to demonstrate the dominating effect of *host* atoms near band-edges. This is done to bring out the one-to-one correlation between the electronic and polar properties of MHyPbCl_3 . The atoms dominating the valence band near Fermi-levels are the ones that contribute maximum to polarization enhancement and are part of the more-distorted layer of *host*, *i.e.*, layer-2.

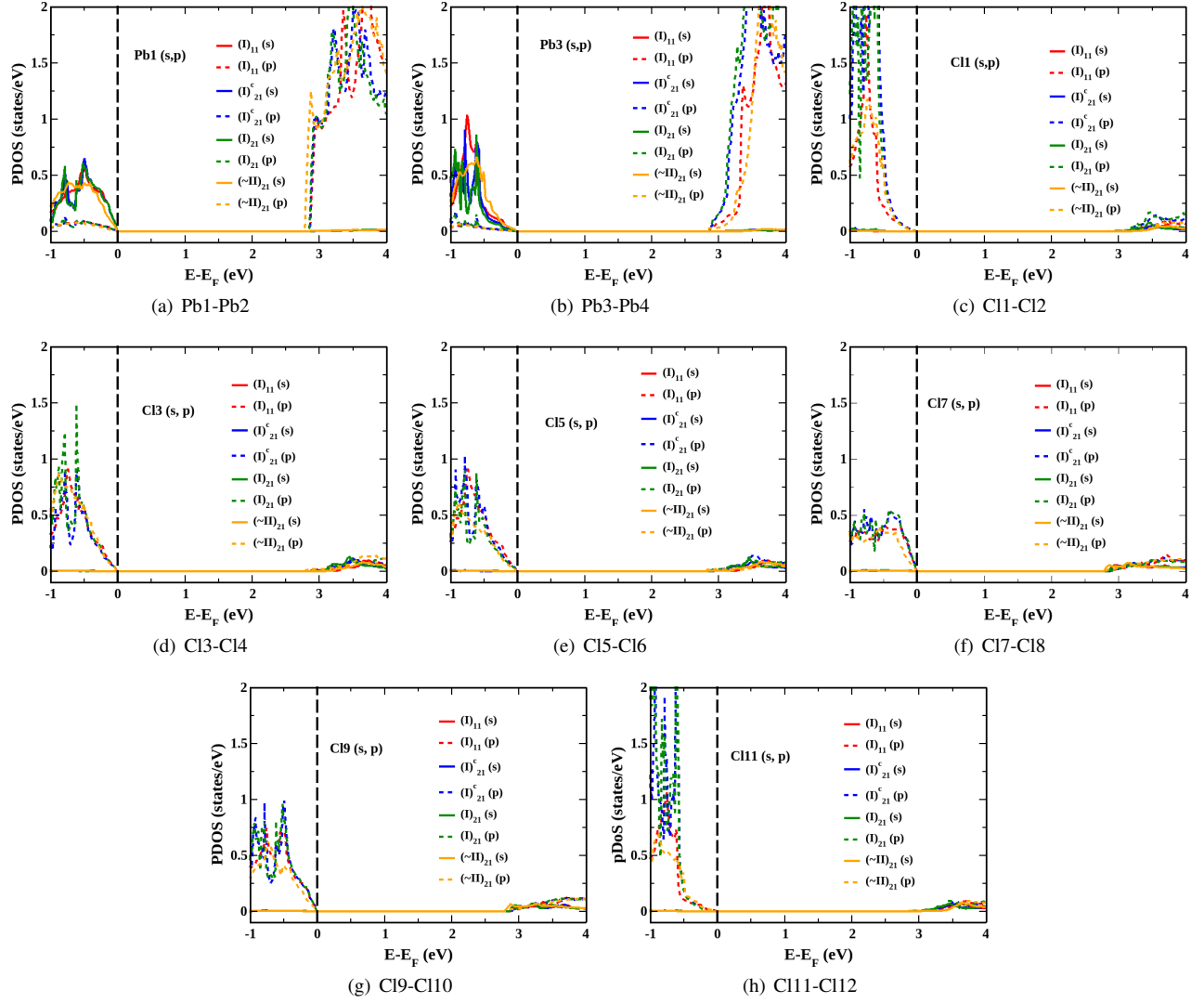


FIG. S35. Orbital PDOS of different structures studied to demonstrate the orbitals of *host* atoms involved in the dominating contribution of the *host* near the Fermi-level. This is done to bring out the correlation between electronic and polar properties. The latter is predominantly due to the more distorted layer of *host*, *i.e.*, layer-2, which is the same for the valence band near the Fermi-level of PDOS plots. For the numbering of the atoms, refer to Fig. S23 for both Phase-I and $(\sim II)_{21}$.

-
- [1] G. Nagabhushana, R. Shivaramaiah, and A. Navrotsky, *Proc. Natl. Acad. Sci. U.S.A.* **113**, 7717 (2016).
- [2] W. Travis, E. Glover, H. Bronstein, D. Scanlon, and R. Palgrave, *Chem. Sci.* **7**, 4548 (2016).
- [3] G. Kieslich, S. Sun, and A. K. Cheetham, *Chem. Sci.* **6**, 3430 (2015).
- [4] N. Onoda-Yamamuro, T. Matsuo, and H. Suga, *J. Phys. Chem. Solids* **53**, 935 (1992).
- [5] M. Faghifnasiri, M. Izadifard, and M. E. Ghazi, *J. Phys. Chem. C* **121**, 27059 (2017).
- [6] T. T. Thu Nguyen, Y. Kim, S. Bae, M. Bari, H. R. Jung, W. Jo, Y.-H. Kim, Z.-G. Ye, and S. Yoon, *J. Phys. Chem. Lett.* **11**, 3773 (2020).
- [7] F. H. Naqvi and J.-H. Ko, *Materials* **15**, 8151 (2022).
- [8] C. Roiland, G. Trippé-Allard, K. Jemli, B. Alonso, J.-C. Ameline, R. Gautier, T. Bataille, L. Le Polles, E. Deleporte, J. Even, *et al.*, *Phys. Chem. Chem. Phys.* **18**, 27133 (2016).
- [9] A. G. Kontos, G. K. Manolis, A. Kaltzoglou, D. Palles, E. I. Kamitsos, M. G. Kanatzidis, and P. Falaras, *J. Phys. Chem. C* **124**, 8479 (2020).
- [10] S. Govinda, B. P. Kore, D. Swain, A. Hossain, C. De, T. N. Guru Row, and D. Sarma, *J. Phys. Chem. C* **122**, 13758 (2018).
- [11] M. Mączka, A. Gağor, J. K. Zaręba, D. Stefańska, M. Drozd, S. Balciunas, Šimėnas, J. M., Banyš, and A. Sieradzki, *Chem. Mater.* **32**, 4072 (2020).
- [12] S. Kanno, Y. Imamura, A. Saeki, and M. Hada, *J. Phys. Chem. C* **121**, 14051 (2017).
- [13] S. Kanno, Y. Imamura, and M. Hada, *J. Phys. Chem. C* **121**, 26188 (2017).
- [14] M. Mączka and M. Ptak, *Solids* **3**, 111 (2022).
- [15] E. C. Schueller, G. Laurita, D. H. Fabini, C. C. Stoumpos, M. G. Kanatzidis, and R. Seshadri, *Inorg. Chem.* **57**, 695 (2018).
- [16] E. M. Mozur, J. C. Trowbridge, A. E. Maughan, M. J. Gorman, C. M. Brown, T. R. Prisk, and J. R. Neilson, *ACS Mater. Lett.* **1**, 260 (2019).
- [17] S. Maity, S. Verma, L. M. Ramaniah, and V. Srinivasan, *Chem. Mater.* (2022).
- [18] A. Oranskaia, J. Yin, O. M. Bakr, J.-L. Bredas, and O. F. Mohammed, *J. Phys. Chem. Lett.* **9**, 5474 (2018).
- [19] J.-B. Li, Z.-K. Jiang, R. Wang, J.-Z. Zhao, and R. Wang, *NPJ Comput. Mater.* **9**, 62 (2023).
- [20] P. Whitfield, N. Herron, W. Guise, K. Page, Y. Cheng, I. Milas, and M. Crawford, *Sci. Rep.* **6**, 35685 (2016).
- [21] J. Wu, J. Chen, and H. Wang, *J. Am. Chem. Soc. Au* **3**, 1205 (2023).
- [22] W. A. Saidi and J. J. Choi, *J. Chem. Phys.* **145**, 144702 (2016).
- [23] J. Yin, G. Teobaldi, and L.-M. Liu, *J. Phys. Chem. Lett.* **13**, 3089 (2022).
- [24] F. Brivio, J. M. Frost, J. M. Skelton, A. J. Jackson, O. J. Weber, M. T. Weller, A. R. Goni, A. M. Leguy, P. R. Barnes, and A. Walsh, *Phys. Rev. B* **92**, 144308 (2015).
- [25] Z. Xu, M. Chen, and S. F. Liu, *Sci. China Chem.* **62**, 866 (2019).
- [26] G. Kresse and J. Hafner, *Phys. Rev. B* **47**, 558 (1993).
- [27] G. Kresse and J. Furthmüller, *Comput. Mater. Sci.* **6**, 15 (1996).
- [28] G. Kresse and J. Furthmüller, *Phys. Rev. B* **54**, 11169 (1996).
- [29] J. P. Perdew, K. Burke, and M. Ernzerhof, *Phys. Rev. Lett.* **77**, 3865 (1996).
- [30] J. P. Perdew, A. Ruzsinszky, G. I. Csonka, O. A. Vydrov, G. E. Scuseria, L. A. Constantin, X. Zhou, and K. Burke, *Phys. Rev. Lett.* **100**, 136406 (2008).
- [31] J. P. Perdew, M. Ernzerhof, and K. Burke, *J. Chem. Phys.* **105**, 9982 (1996).
- [32] J. Yang, L. Z. Tan, and A. M. Rappe, *Phys. Rev. B* **97**, 085130 (2018).
- [33] M.-H. Tremblay, J. Bacsá, S. Barlow, and S. R. Marder, *Mater. Chem. Front.* **4**, 2023 (2020).
- [34] M. L. Holekevi Chandrappa, Z. Zhu, D. P. Fenning, and S. P. Ong, *Chem. Mater.* **33**, 4672 (2021).
- [35] C. Li, S. Tscheuschner, F. Paulus, P. E. Hopkinson, J. Kießling, A. Köhler, Y. Vaynzof, and S. Huettner, *Adv. Mater.* **28**, 2446 (2016).
- [36] A. Stroppa, C. Quarti, F. De Angelis, and S. Picozzi, *J. Phys. Chem. Lett.* **6**, 2223 (2015).
- [37] S. Hu, H. Gao, Y. Qi, Y. Tao, Y. Li, J. R. Reimers, M. Bokdam, C. Franchini, D. Di Sante, A. Stroppa, *et al.*, *J. Phys. Chem. C* **121**, 23045 (2017).
- [38] R. King-Smith and D. Vanderbilt, *Phys. Rev. B* **47**, 1651 (1993).
- [39] R. Resta, *Ferroelectrics* **151**, 49 (1994).
- [40] R. Resta and D. Vanderbilt, in *Physics of Ferroelectrics* (Springer, 2007) pp. 31–68.
- [41] N. A. Spaldin, *J. Solid State Chem.* **195**, 2 (2012).
- [42] A. D. Becke, *J. Chem. Phys.* **104**, 1040 (1996).
- [43] C. Lee, W. Yang, and R. G. Parr, *Phys. Rev. B* **37**, 785 (1988).
- [44] A. McLean and G. Chandler, *J. Chem. Phys.* **72**, 5639 (1980).
- [45] R. Krishnan, J. S. Binkley, R. Seeger, and J. A. Pople, *J. Chem. Phys.* **72**, 650 (1980).
- [46] A. Ciupa-Litwa, M. Ptak, E. Kucharska, J. Hanuza, and M. Mączka, *Molecules* **25**, 5215 (2020).
- [47] G. Petersson, A. Bennett, T. G. Tensfeldt, M. A. Al-Laham, W. A. Shirley, and J. Mantzaris, *J. Chem. Phys.* **89**, 2193 (1988).
- [48] G. Petersson and M. A. Al-Laham, *J. Chem. Phys.* **94**, 6081 (1991).
- [49] M. J. Frisch, G. W. Trucks, H. B. Schlegel, G. E. Scuseria, M. A. Robb, J. R. Cheeseman, G. Scalmani, V. Barone, G. A. Petersson, H. Nakatsuji, X. Li, M. Caricato, A. V. Marenich, J. Bloino, B. G. Janesko, R. Gomperts, B. Mennucci, H. P. Hratchian, J. V. Ortiz, A. F. Izmaylov, J. L. Sonnenberg, D. Williams-Young, F. Ding, F. Lipparini, F. Egidi, J. Goings, B. Peng, A. Petrone, T. Henderson, D. Ranasinghe, V. G. Zakrzewski, J. Gao, N. Rega, G. Zheng, W. Liang, M. Hada, M. Ehara, K. Toyota, R. Fukuda, J. Hasegawa, M. Ishida, T. Nakajima, Y. Honda, O. Kitao, H. Nakai, T. Vreven, K. Throssell, J. A. Montgomery, Jr., J. E. Peralta, F. Ogliaro, M. J. Bearpark, J. J. Heyd, E. N. Brothers, K. N. Kudin, V. N. Staroverov, T. A. Keith, R. Kobayashi, J. Normand, K. Raghavachari, A. P.

- Rendell, J. C. Burant, S. S. Iyengar, J. Tomasi, M. Cossi, J. M. Millam, M. Klene, C. Adamo, R. Cammi, J. W. Ochterski, R. L. Martin, K. Morokuma, O. Farkas, J. B. Foresman, and D. J. Fox, Gaussian 16 Revision C.01 (2016), gaussian Inc. Wallingford CT.
- [50] E. Berger, J. Wiktor, and A. Pasquarello, *J. Phys. Chem. Lett.* **11**, 6279 (2020).
- [51] X. Wu, O. Diéguez, K. M. Rabe, and D. Vanderbilt, *Phys. Rev. Lett.* **97**, 107602 (2006).
- [52] N. Marzari and D. Vanderbilt, in *AIP Conference Proceedings*, Vol. 436 (American Institute of Physics, 1998) pp. 146–155.
- [53] M. Stengel and N. A. Spaldin, *Phys. Rev. B* **73**, 075121 (2006).
- [54] A. A. Soluyanov and D. Vanderbilt, *Phys. Rev. B* **83**, 035108 (2011).
- [55] N. Marzari and D. Vanderbilt, *Phys. Rev. B* **56**, 12847 (1997).
- [56] A. A. Mostofi, J. R. Yates, G. Pizzi, Y.-S. Lee, I. Souza, D. Vanderbilt, and N. Marzari, *Comput. Phys. Commun.* **185**, 2309 (2014).
- [57] I. Souza, N. Marzari, and D. Vanderbilt, *Phys. Rev. B* **65**, 035109 (2001).
- [58] G. Pizzi, V. Vitale, R. Arita, S. Blügel, F. Freimuth, G. Géranton, M. Gibertini, D. Gresch, C. Johnson, T. Koretsune, *et al.*, *J. Phys.: Condens. Matter* **32**, 165902 (2020).
- [59] E. Mosconi, A. Amat, M. K. Nazeeruddin, M. Gratzel, and F. De Angelis, *J. Phys. Chem. C* **117**, 13902 (2013).
- [60] N. Pandey, T. Kongnok, N. Palakawong, S. Limpijumnong, W. R. Lambrecht, and S. Junghwan, *ACS omega* **5**, 25723 (2020).
- [61] A. Mehdizadeh, S. F. Akhtarianfar, and S. Shojaei, *J. Phys. Chem. C* **123**, 6725 (2019).
- [62] B. Kim, J. Kim, and N. Park, *Sci. Rep.* **10**, 1 (2020).
- [63] D. Liu, Q. Li, J. Hu, H. Jing, and K. Wu, *J. Mater. Chem. C* **7**, 371 (2019).